CHALMERS
UNIVERSITY OF TECHNOLOGY

Wind Tunnel Test of a Double Blade Swept Propeller and Analysis of Real Geometry Effects

Master's Thesis in Applied Mechanics

Sandra Busch Isak Jonsson

Department of Applied Mechanics
Chalmers University of Technology
Gothenburg, Sweden 2015-06-15
Master's Thesis 2015:13

Master's thesis 2015:13

Wind Tunnel Test of a Double Blade Swept Propeller and Analysis of Real Geometry Effects

SANDRA BUSCH and ISAK JONSSON

Department of Applied Mechanics
Division of Fluid Dynamics
Chalmers University of Technology
Gothenburg, Sweden 2015

Wind Tunnel Test of a Double Blade Swept Propeller and Analysis of Real Geometry Effects
SANDRA BUSCH and ISAK JONSSON

Supervisors: Alexandre Capitao Patrao, Applied Mechanics and Anders Lundbladh, GKN Aerospace and Richard Avellán, GKN Aerospace
Examiner: Tomas Grönstedt, Applied Mechanics

Master's Thesis 2015:13
Department of Applied Mechanics
Division of Fluid Dynamics
Chalmers University of Technology
SE-412 96 Gothenburg
Telephone +46 31 772 1000

Cover: Static rig logo, designed by Véronique Thill

Gothenburg, Sweden 2015

Wind Tunnel Test of a Double Blade Swept Propeller and Analysis of Real Geometry Effects

SANDRA BUSCH and ISAK JONSSON
Department of Applied Mechanics
Chalmers University of Technology

Abstract

This Master Thesis has been carried out at Chalmers University of Technology in Göteborg and GKN Aerospace in Trollhättan during the spring of 2015. The aim was to identify the effects of as-manufactured geometry and mechanical deformation on the aerodynamic performance of a double blade swept propeller, also called "Boxprop".

The Boxprop is a new high speed propeller concept that was developed by Richard Avellán and Anders Lundbladh at Volvo Aero Corporation in Trollhättan, now GKN Aerospace Sweden. In the past, research has been focused mainly on jet engines, since propeller driven aircraft only form a small part of the commercial air traffic. Nevertheless, propellers have high propulsive efficiencies due to low operating pressure ratios, which is of interest in terms of a reduction of emissions and noise.

The blades of conventional high speed propellers are swept rearwards whereas the Boxprop comprises forward swept blades that are joined at the tip. The forward sweep is supposed to have a positive influence at the tip flow but the drawbacks are usually aerodynamic instabilities and flutter. These disadvantages may be eliminated by the joined blade tips which make the Boxblade geometry stiffer and improves the stability.

Chalmers University of Technology in Göteborg and GKN Aerospace collaborate in the NFFP iFram project to develop the Boxprop concept further. Previous master theses' showed discrepancies between CFD simulation results and experimental testing. By realising further CFD simulations and static as well as dynamic experimental tests, these differences could be identified and thus be considered in further research.

The CFD simulations yielded that roughness of the propeller blades may reduce the turbo efficiency up to 15%, and causes an increase in propeller torque as well as a decrease in propeller thrust. Those values change in function of the employed advance ratio of the propeller. Another contributing factor that could be identified was the geometry of the nacelle, which causes a light increase in performance due to lower local wind speed in front of the propeller. Last but not least, also the deformation of the blade causes an increase in performance, due to a larger diameter when deformed. The performance is also influenced by the change of the angle of the leading edge, resulting in slightly twisted blade. The effect on the flow field of the deformed GPX-313 can only be estimated, since it would involve an extended analysis of various blade sections in CFD that could not be realised in the time available.

Experiments with Boxprops made out of rigid opaque material with a diameter of $0.15\,m$ and $0.3\,m$ have been realised statically and in the Chalmers L2 wind tunnel at speeds up to $40\,m/s$ and a rotational tip speed up to $210\,m/s$, corresponding to up to $26000\,rpm$ rotational speed, to further study the performance of the Boxprop. An analysis of the flow field in the propeller swirl of the propeller was carried out with a

stereo PIV, studying a plane along the wind tunnel flow field.

Surface roughness measurements and 3D scans have been conducted on Boxprop blades to identify manufactured defects that can have impact on aerodynamic performance. FE simulations were done to calculate deformation of a Boxprop due to rotational load during testing. Polished and non-polished blades have been compared experimentally to test the impact of decreased roughness.

The ability to conduct experiments in the Chalmers wind tunnel gave comparable experimental results for various advance ratios to verify the performance of the propeller. Considering roughness effects and disturbances in material deformation and flow field, the experimental results are on the same level as the results from the CFD simulations.

Contents

Preface

The work presented in this thesis was carried out at Chalmers University of Technology in Göteborg in close collaboration with GKN Aerospace in Trollhättan. We would like to thank our supervisors at GKN, Anders Lundbladh and Richard Avallán which always provided valuable input to the problems encountered and great support and guidance during our thesis work. In addition, we would like to express our gratitude towards our examiner Tomas Grönstedt for the support and the ability to realise this thesis work at Chalmers University. We would also like to thank Alexandre Capitao Patrao at the Department of Applied Mechanics for the valuable support and sharing his knowledge especially for the CFD part of this thesis but also for his interest and suggestions towards the experimental testing. For the support regarding the test rig and the wind tunnel experiments, we like to thank Valery Chernoray at the Department of Applied Mechanics. For the realisation of the PIV session in the wind tunnel we would like to thank Mikhail Tokarev at the Department of Applied Mechanics. We appreciate the possibility to use the resources of Chalmers Centre for Computational Science and Engineering (C3SE) for the calculations realised in this project. For the usage of material and machines in the prototype workshop in mechanical building we would like to thank the Mechanical Engineering Department at Chalmers. This work has been financed by the Swedish National Aeronautical Research Program (NFFP), which is jointly run by the Swedish Armed Forces, Swedish Defence Materiel Administration and the Swedish Governmental Agency for Innovation Systems.

Sandra Busch and Isak Jonsson, Göteborg September 7, 2015

Nomenclature

Abbreviations

$BLDC$ Brushless Direct Current

CCL CFX command language

CFD Computational Fluid Dynamics

EMF Electro Magnetic Field

GPS GKN Propeller Single Blade

GPX GKN Propeller Boxblade

$NACA$ National Advisory Committee for Aeronautics

$NFFP$ Swedish National Aeronautical Research Program

PIV Particle Image Velocimetry

PWM Pulse Wave Modulated

RMS Root Mean Square

ADT Acturator Disk Theory

NTIS National Technical Information Service

PLA Polylactic acid

Greek Symbols

β_{cp}	Confidence Level	
δ_v	Viscous layer thickness	$[m]$
$\dot{\omega}$	Angular Acceleration	

η_p	Propeller efficiency	
η_t	Turbo efficiency	
γ	Ratio of specific heats	
μ	Dynamic viscosity	$[Pas]$
ν	Kinematic viscosity	$[m^2/s]$
ω	Turbulent frequency	
ϕ	Advance angle	$[^\circ]$
ρ	Density of the fluid	$[kg/m^3]$
σ_{uts}	Ultimate Tensile Strength	
τ_w	Shear stress	$[N/m^2]$
ε	Turbulent dissipation	

Lower Case Roman

$\overline{x}$	Sample Mean	
a	Speed of sound	$[m/s]$
c	Chord length	$[m]$
c_d	Drag coefficient	
c_l	Lift coefficient	
k	Turbulent kinetic energy	
k_s	Roughness height	$[m]$
k_s^+	Dimensionless roughness height	
$k_{s,eq}$	Equivalent roughness height	$[m]$
l	Characteristic length	$[m]$
p_∞	Ambient pressure	$[Pa]$
Re_{crit}	Critical Reynolds number	
s	Standard Deviation	
u^+	Dimensionless velocity	
u_τ	Wall friction velocity	$[m/s]$

v	Absolute velocity	$[m/s]$
v_p	Velocity in the propeller plane	$[m/s]$
v_s	Slipstream velocity	$[m/s]$
y^+	Dimensionless wall distance	

Upper Case Roman

A_p	Propeller disk area	$[m^2]$
C_P	Coefficient of power	
C_T	Coefficient of thrust	
D	Diameter of the propeller	$[m]$
dD	Sectional drag force	$[N/m]$
dL	Sectional lift force	$[N/m]$
dQ	Sectional Torque	$[N/m]$
dT	Sectional Thrust	$[N/m]$
F	Force	$[N]$
I	Body Inertia	
M	Mach number	
M	Torque	
P	Power	$[N]$
R	Specific gas constant	$[J/kgK]$
R_a	Arithmetic roughness	$[m]$
Re	Reynolds number	
T	Temperature	$[K]$
T	Thrust	$[N]$
U	Mean velocity	$[m/s]$
V	Relative velocity	$[m/s]$
V	Velocity	$[m/s]$
V'	Ambient Wind speed	$[m/s]$
V_∞	Free stream velocity	$[m/s]$

1

Introduction

This chapter gives a short overview of the Boxprop concept as well as previous and ongoing projects. The aims, scope and limitations for this thesis work are also presented.

1.1 Background

The Boxprop is a new high speed propeller concept that was developed by Richard Avellán and Anders Lundbladh at Volvo Aero Corporation in Trollhättan, Sweden, now GKN Aerospace. In the past, research has been focused mainly on jet engines since propeller driven aircrafts only form a small part of the commercial air traffic, either in smaller commuter airplanes or freighters. Nevertheless, propellers have high propulsive efficiencies due to low operating pressure ratios which is of interest in terms of a reduction of emissions and noise.

These properties led, for instance, NASA and General Electrics to develop the GE36, an unducted fan (UDF) or propfan during the oil crisis of the late 1970's and early 1980's. First prototypes and test flights have been realised, but although the open rotor arrangement had a low specific fuel consumption the development was discontinued. The noise levels caused by the open rotor design remain a significant issue as they can not be damped out by a surrounding nacelle.

The blades of conventional high speed propellers are swept rearwards, whereas the Boxprop comprises forward swept blades which are joined at the tip. The forward sweep is thought to have a positive influence at the tip flow but the drawbacks are usually aerodynamic instabilities and flutter. These disadvantages may be eliminated by the joined blade tips which possibly make the Boxblade geometry stiffer and improve the stability. The current Boxprop is shown in Figure 1.1.

Over the past few years, Chalmers University of Technology in Göteborg and GKN Aerospace have cooperated in the development of this type of propeller which resulted in the iFram project. In this project, several Master Theses and project works have been

carried out as well as ongoing or future doctorates. During these works, two types of test rig, a single static rig (SSR) and a dual dynamic rig (DDR), have been realised as well as CFD simulations to determine the aerodynamic performance of the Boxprop.

The first CFD simulations were carried out mainly at cruise speed, whereas the experimental tests of the manufactured propellers were realised at static conditions. This complicated the comparison of experimental and simulation results. Another cause for the significant discrepancies between those results are additional effects due to deformation, roughness, and disturbances in the flow field such as recirculation of the flow in the static test rig.

1.2 Aims

The core aim of the thesis is to obtain a greater understanding of the discrepancies that occur between experimental tests and CFD simulations that have already been carried out in previous Master Theses [1], [2], [3] and [4]. Achieving this aim requires various CFD simulations, as well as the reconditioning of the existing test rig at Chalmers University. Factors that are thought to contribute to the discrepancies between simulation and testing such as roughness effects and deformation also need to be studied further. As the test rig has until now only been run in static conditions, testing was also conducted in the Chalmers wind tunnel.

1.3 Scope and limitations

Although the DDR is intended for testing counter rotating propellers, the experimental tests conducted in this thesis are only single rotating. Counter rotating tests would probably be performed with one front Boxprop and one conventional blade as aft propeller. Since the work focuses on the development of the Boxprop and not conventional blade design, counter rotating tests were not considered in this thesis work. This also applies to the CFD simulations as they only consider single rotating propellers. The CFD simulations use a simplified computational domain compared to the test set up with only one blade out of five being represented in this domain. Testing in the wind tunnel is limited to low rotational speeds since the material of the propellers is brittle and the risk of breaking them is too high. The same applies for the wind speed in the wind tunnel. The manufactured Boxprop are made out of plastic material, a change in propeller material (except different plastics) was not considered. This also limits the variety of cases that can be tested in either the static or wind tunnel tests as the blade pitch is fixed and one propeller can not be used for testing of different flight conditions (take-off, cruise, approach). In order to establish the deformation of the propellers under centrifugal load, only basic finite element methods (FEM) are used, since the specialisation of both thesis workers is in the field of fluid dynamics.

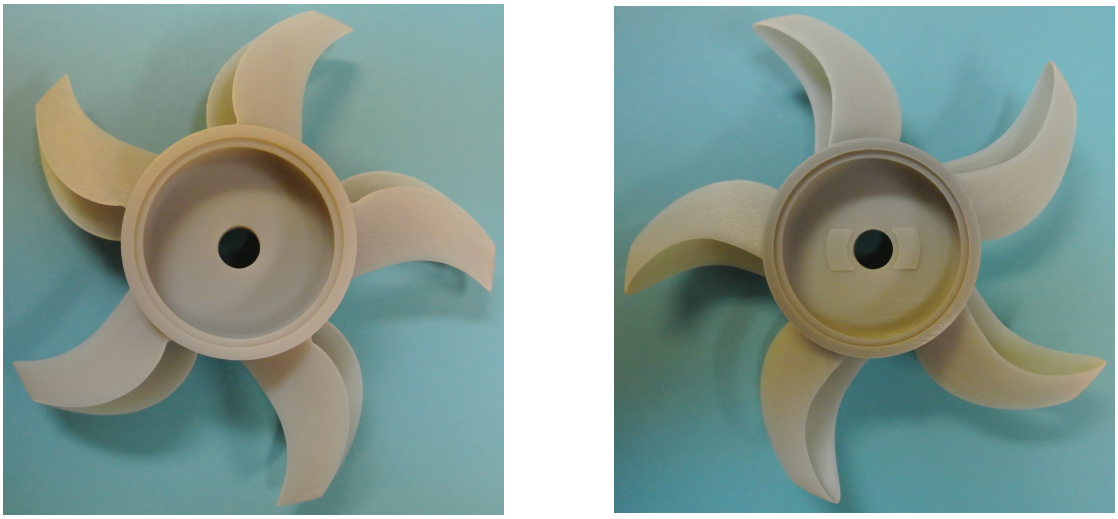

Figure 1.1: Manufactured Boxprop (GP-X-313) with a diameter of 150 mm shown from front (picture to the right) and back side (picture to the left).

2

Theory

In this chapter the main theory concerning aerodynamics, Computational Fluid Dynamics (CFD) and the testing facilities is presented. Since this work succeeds previous thesis works, some of the most used expressions are repeated whereas others that have been mentioned before are not cited in full detail, focusing instead on new aspects that have been introduced in this thesis work to obtain a better agreement between simulation and testing.

2.1 Aerodynamics

In this section the underlying aerodynamics of common propellers and also of the Boxprop will be presented. In section 2.2 the governing equations of importance to this case will be presented as well as their implementation in the CFD software that was used in this work.

2.1.1 Airfoil design

Propeller blades have varying twist, chord and thickness from hub to tip. Thus, with a certain blade sweep, thickness and chord distribution, the airfoil profile will change primarily as a function of the radial distance from the hub. For propeller blade design, the main parameters are usually taken from established blade profile families for certain applications. The Boxprop uses *e.g.* the NACA 16-series which is characterized by low drag at high speeds, and avoidance of low pressure peaks; although it only has a relatively low lift, which makes it suitable mainly for aircraft and ship propellers [5].

The current Boxprop, GPX313, has been developed by S. Adriansson [1] and Olofsson and Pettersson [2] during their thesis work. This resulted in a Matlab code, called BBCode, which creates the geometry of the Boxblade. The geometry of the Boxblade is based on the NACA 16-series profiles, stacked upon a continuously curved stacking line, similar to a catenary, which can be defined by modifying different parameters in

the BBCode. The data sheets generated by the Matlab code can be read into either Autodesk Inventor or Catia to build a 3D geometry.

2.1.2 Actuator disk and blade element method

Actuator disk theory can be used to calculate the thrust generated by a propeller. Assumptions are incompressible flow, and an increase in velocity and pressure induced by the disk. This theory is modeled by a control volume surrounding a stream tube with surrounded fluid, as shown in Figure 2.1. The inlet conditions are ambient pressure p_∞, a fluid velocity V_∞ and constant density ρ. Assumptions for the propeller disk are amongst others that it is infinitely thin, has an infinite amount of blades, a given diameter D and the flow can be considered as incompressible, isentropic and inviscid. The velocity through the propeller plane is assumed to be uniform of magnitude v_p. The flow inside the stream tube behind the propeller is accelerated to the uniform slipstream velocity v_s.

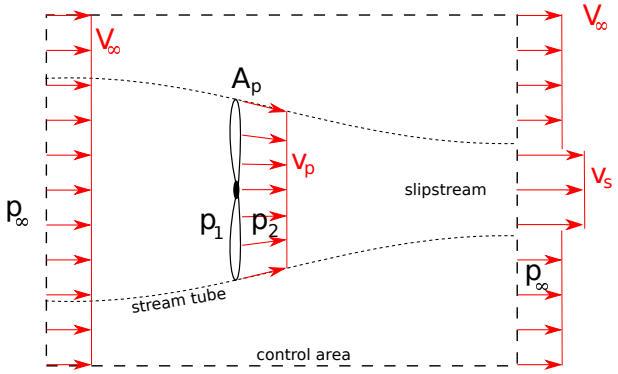

Figure 2.1: Model for the actuator disk theory, adapted from [6]

The thrust can be described as either a change of momentum or as the force on the disk surface A_p exerted by the pressure:

$$T = \rho v_p A_p \left(v_s - V_\infty\right) \tag{2.1}$$

$$T = \left(p_2 - p_1\right) A_p \tag{2.2}$$

Using the pressure difference in front and behind the disk gives

$$v_p = \frac{v_s + V_\infty}{2} \tag{2.3}$$

which indicates that the velocity through the propeller plane is the mean value of the free stream velocity in front of the propeller and the slipstream velocity behind the propeller [6].

Figure 2.2 shows a propeller blade element at a distance r from the shaft. The rotational velocity is described as $2\pi nr$, and V_∞ is the free stream velocity. The resultant

relative velocity V encloses the advance angle φ. From this, a non-dimensional coefficient, the advance ratio, can be derived:

$$J = \frac{V}{nD} \tag{2.4}$$

This ratio defines the distance achieved in one revolution of the propeller and will be used further since it enables a direct comparison between different propellers.

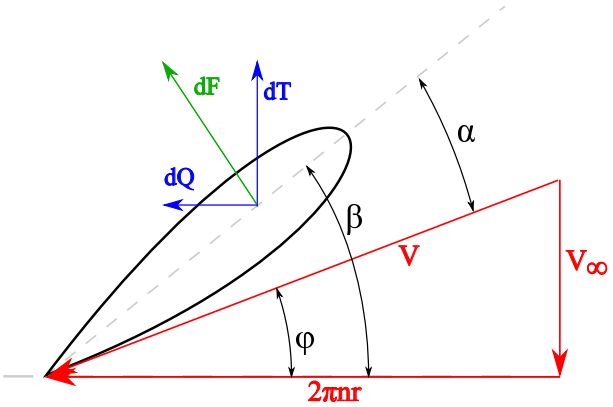

Figure 2.2: Forces acting on a propeller blade element, adapted from [6]

The thrust dT is in the direction of the freestream velocity V_∞ and the torque is in the rotational direction of the propeller. The definitions are as follows:

$$\begin{aligned} dL &= c_l \frac{1}{2} \rho V^2 c dr \\ dD &= c_d \frac{1}{2} \rho V^2 c dr \\ dT &= dL \cos\phi - dD \sin\phi \\ dQ &= (dL \sin\phi + dD \cos\phi)\, r \end{aligned} \tag{2.5}$$

where c_l and c_d is the lift and drag coefficient, respectively, ρ the density of the fluid, and c the chord length. To obtain the total blade thrust, an integration over all elements of the blade has to be performed from hub to tip. For the total propeller thrust, this has further to be multiplied by the number of blades.

Further on, the coefficients of thrust C_T and power C_P are needed, which are defined as follows:

$$\begin{aligned} C_T &= \frac{T}{\rho n^2 D^4} \\ C_P &= \frac{P}{\rho n^3 D^5} \end{aligned} \tag{2.6}$$

where T is the thrust, n the rotational speed and D the diameter of the propeller. These coefficients are also used to compare different propeller types with each other or to compare between simulation and experiments [6].

The propeller efficiency is defined as

$$\eta_p = \frac{Tv_0}{P} \tag{2.7}$$

where P is the product of the torque and rotational speed, *i.e.* shaft power.

The propeller efficiency is largely depending on the inlet velocity, whereas the turbo efficiency can also be used in static conditions. The turbo efficiency, which relates the jet power to the shaft input power, was derived by A. Lind [4] as:

$$\eta_t = \frac{T}{2P}\sqrt{\frac{2T}{\rho\frac{D^2\pi}{4}\left(1-\left(\frac{d}{D}\right)^2\right)}+V_\infty^2}+V_\infty \tag{2.8}$$

and assumes incompressible flow.

2.1.3 Airfoils and 3-D effects

The flow around airfoils can usually be regarded as two-dimensional. In our case, however, a three-dimensional analysis is necessary as a finite blade span has to be dealt with. Vortices, and thus losses created around the blade tips, are of particular interest. Figure 2.3 shows the pressure distribution around a blade with the suction side above the wing and the pressure side below the wing profile. At the tip the pressure differences adjust since a flow around the blade tip takes place, which also decreases the lift at the tip. With the flow at the tip having different directions, a swirl starts to form in the flow field behind the wings. These trailing vortices are dissipated further behind the wings. In general, the behaviour of aircraft wings and propeller blades are similar, therefore the wing theory can also be applied to propeller blades, to a great extent.

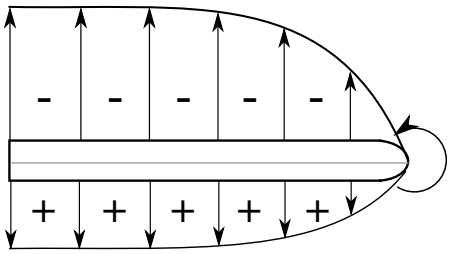

Figure 2.3: Flow around finite airfoils, adapted from [6]

As there is a vortex field behind the propeller, the propeller blades also create induced drag, similar to aircraft wings. Therefore the induced velocities have to be added in Figure 2.2, as can be seen in Figure 2.4. To include the influence of the propeller vortex field we need to combine the actuator disk theory and the blade element method [6].

The potential benefits of the Boxprop include a reduction of the losses created due to tip vortices as well as a decrease of wing induced drag. Kroo [7] compares mono

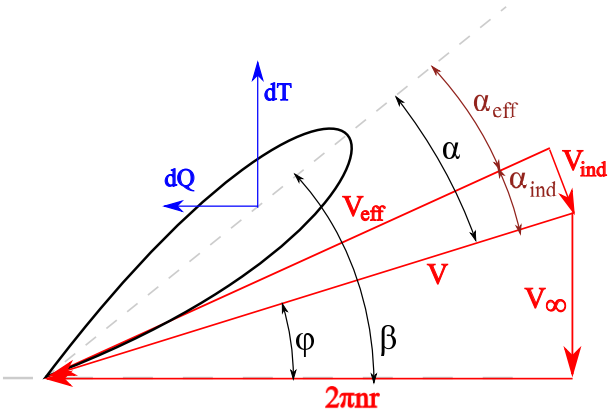

Figure 2.4: Forces acting on a propeller blade element with included induced velocities, adapted from [6]

and multiplanes regarding their drag and efficiency, showing that multiplanes in general generate less induced drag than monoplanes for a given wing span. The box wing in particular achieves the lowest drag for a given span and height, and has the best span efficiency.

2.1.4 Blade pitch

To have high efficiency at all flight conditions, *e.g.* cruise, take-off, and landing, the blade pitch needs to be adjustable. For this, a special hub design is needed and the manufacturing of the blades becomes more complicated and time consuming. Thus, it would only be of interest to include this feature if a metal propeller were about to be tested in the test rig. In this thesis work, all propellers were made using rapid-prototyping techniques and thus come with a fixed blade pitch angle. The manufactured propellers are designed for take-off conditions, suitable for static testing or testing at low wind speeds. The GPX313 has a blade pitch angle of 25.9° at 75% radius.

2.2 Flow characteristics and CFD

In this section, the main flow characteristics that influence the aerodynamic performance of the propeller, and its implementation and set up in the CFD simulations will be described.

2.2.1 Basic equations

This sections presents basic equations that were used for experiments and CFD, but are not in the focus of the present work.

The governing equations that are needed to resolve the flow field are the Navier-Stokes equations in their conservation form, which are the continuity, momentum and

energy equations. Since the flow that is treated is turbulent, an averaging of the turbulent quantities is necessary, which results in the Reynolds Averaged Navier-Stokes (RANS) equations.

By time averaging the Navier-Stokes equations additional unknowns in form of Reynolds stresses are introduced, yielding more unknowns than available equations. Turbulence modelling has to be used to relate the Reynolds stresses to the mean parameters of the flow. Common turbulence models are, among others, the $k-\varepsilon$ model and the $k-\omega$ model.

The turbulence model used in previous works [4] was the SST $k-\omega$ turbulence model and has been further employed since it is the most recommended for aerodynamic and rotational flows. The Menter SST $k-\omega$ model is based on the Wilcox $k-\omega$ model using a different transformation from the ε to the ω equation, as well as different model constants, blending functions for the transition between the near-wall formulation and the free stream formulation and limiters for improved performance in flows with adverse pressure gradients [8].

The characteristic dimensionless number used to describe the turbulence in a flow field is the Reynolds number, defined as:

$$Re = \frac{\rho V_\infty l}{\mu} \tag{2.9}$$

where l is the characteristic length and μ the dynamic viscosity. The critical Reynolds number for the transition from laminar to turbulent flow around flat plates is about $Re_{crit} = 5 \cdot 10^5$; around airfoils, it is $Re_{crit} = 1 \cdot 10^6$ [9].

Furthermore, the Mach number is defined as the ratio of the flow velocity to the local speed of sound and is thus dimensionless. The speed of sound is defined as the square root of the product of the ratio of the specific heats, the specific gas constant and local temperature, and is therefore largely temperature dependent [10].

$$M = \frac{v}{a} = \frac{v}{\sqrt{\gamma R T}} \tag{2.10}$$

2.2.2 Boundary layer theory

In the wall-near region, there are three flow layers with different characteristics, the viscous sub-layer, the buffer layer and the log-law layer. They are defined using the dimensionless wall distance y^+:

$$y^+ = \frac{\Delta y u_\tau}{\nu} \tag{2.11}$$

where Δy is the distance to the wall, $u_\tau = {\tau_w}/{\rho^{\frac{1}{2}}}$ is the wall friction velocity, calculated from the shear stress and the density of the fluid and ν is the kinematic viscosity of the fluid.

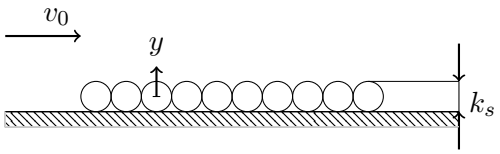

Figure 2.5: Representation of the sand roughness height, adapted from [11]

The viscous layer is very thin with $y^+ \leq 5$ and the thickness of this layer can be estimated as

$$\delta_v = \frac{\nu}{u_\tau} \tag{2.12}$$

The dimensionless velocity, defined as $u^+ = {}^{U}/_{u_\tau}$ with U being the mean velocity, and the dimensionless wall distance are linear throughout the viscous sub-layer, therefore $y^+ = u^+$.

The buffer layer serves as a transition between the by viscous stresses dominated viscous sub-layer and the log-law layer, which is dominated by turbulent effects. The log-law layer passes into the outer layer afterwards which is mainly the turbulent free stream and thus free from viscous effects. The range of the buffer layer and the log-law layer are given slightly different in literature [8] [11].

2.2.3 Wall treatment

Wall functions are used for $y^+ \leq 11.63$ [8]. The Menter SST $k-\omega$ turbulence model uses the $k-\omega$ formulation in the near-wall region which is blended into a $k-\varepsilon$ formulation in the fully turbulent region.
The CFD-software ANSYS CFX basically uses three different wall functions: the standard wall functions, scalable wall functions and an automatic near wall treatment for ω-based turbulence models. The first one is obsolete and only included for compatibility reasons. The second one uses a Low-Re number formulation when using a refined mesh, with $y^+ \leq 2$ to resolve the boundary layer. For $y^+ \geq 2$ wall functions are used until the ω-treatment is blended into the $k-\epsilon$. The automatic near wall treatment is used by default in the standard $k-\omega$, baseline $k-\omega$, SST and ω-Reynolds Stress models. Using the scalable wall function is only recommended if the viscous sub-layer can be neglected and also if $y^+ \geq 11.06$, which is the definition ANSYS CFX uses for the intersection between the viscous sub-layer and the log-law region [12].

2.2.4 Surface roughness

Roughness can be understood as particles of different geometric shape but with a certain height k_s, also denoted sand roughness height, covering the surface or wall, as shown in Figure 2.5.

The dimensionless sand roughness is defined as the ratio of sand roughness height to

wall layer thickness:

$$k_s^+ = \frac{k_s}{\delta_v} \tag{2.13}$$

In general, three regimes are distinguished which correspond approximately to the layers within the boundary layer:

hydraulically smooth	$0 \leq k_s^+ \leq 5$
transition region	$5 \leq k_s^+ \leq 70$
fully rough	$k_s^+ \geq 70$

In the hydraulically smooth regime roughness elements are assumed to be within the viscous sublayer, therefore no difference to smooth surfaces is expected. Roughness effects get more important in the transition region and as soon as the roughness elements reach the overlap layer the flow is independent of the Reynolds number [11].

The last regime is essential for the simulations in ANSYS CFX, since the roughness is implemented using the automatic wall functions, which do not work in the fully rough regime. For higher roughness values, the scalable wall functions have to be used which require the editing of the CFX command language (CCL).

Thus for a hydraulically smooth surface, $k_s^+ \leq 5$ is required. For a given blade speed, dimensionless velocity $u^+ = {}^U/_{u_\tau}$ and known kinematic viscosity, the limit for a smooth surface can be estimated. From Kim, Moin and Moser [13], u^+ can be assumed for a flat plate to be around 18 at low Reynolds numbers. At higher Reynolds number and including pressure gradients, *e.g.* an airfoil, u^+ is slightly higher. Thus for a Boxprop with a diameter of $0.15m$, a rotational speed of $26000rpm$, an advance ratio of $J = 0.77$ and an estimated $u^+ = 23$, the calculated length scale is $l^+ = 1.5\mu m$ and the maximum sand roughness needed to still be in the smooth regime at $k_s^+ \leq 5$ would be around $k_s = 10\mu m$.

Usually roughness is described by an equivalent sand roughness $k_{s,eq}$ which is depending among others on the geometry of the particles on the surface, their height, diameter and distance to each other. Values for $k_{s,eq}$ are obtained from experiments and are available for a variety of different industrial materials [11]. Correlating $k_{s,eq}$ to measured roughness on a surface is not easily done, since no universal correlation exists. Adams and Grant [14] or Flack and Schultz [15] propose models to correlate equivalent sand roughness to measured roughness.

2.3 Experimental Evaluation

The experimental work in this thesis is based on the previous thesis work [1], [2] and [3] of which the last two included experiments of box bladed propellers. This section aims to describe the basic theory used while designing and evaluating propeller and rig parameters.

2.3.1 Aerodynamic test similarity

For most aerodynamic experiments down scaled models are used, especially in the early stages of design and development. To obtain usable data from these experiments and models, the nature of the full scale phenomena must be understood and implication of different scaling and their issues acknowledged. Most important dimensionless numbers needed in this case are the Mach number (Eq. 2.10), Reynolds number (Eq. 2.9) and advance ratio (Eq. 2.4).

To be able to compare down scaled models, they should have a geometric similarity and the same Reynolds number. Since compressible flow is considered, the Mach number for both scaled down and full-scale model should also to be the same [16].

Scaling down a propeller has an additional limiting factor compared to static models since advance ratio is of interest. There are therefore three dimensionless numbers that is connect to each other in various ways that have to be considered in scaling a propeller for wind tunnel testing. Worth noting is that changing diameter or rotational velocity has a large impact on rig design since the thrust and power produced by the propeller, as given in equation 2.6, is changing non-linearly by a factor of n^2, D^4 and n^3, D^5, respectively.

If a propeller is scaled down and a constant Mach numbers is sought after, a decreased diameter implies a increased rotational velocity to keep relative tip Mach speed constant.

For a real example the counter rotating open rotor engine AI-PX7 can be used as a reference. That engine has a diameter of $4.26m$ and is designed to fly at Mach 0.75 at an altitude of $10668m$ over sea level and generates a thrust of $19kN$ [17]. The cruise advance ratio is at $J = 3$, whereas the take-off advance ratio would be of $J = 0.6$.

Only realisable cases for the static and dynamic tests will be considered, which are roughly limited to an advance ratio $0.2 \leq J \leq 1.1$, a Mach number $0.2 \leq M \leq 0.7$ and diameter of $0.15m$ to 0.3m. An accurate similarity for full case cruise speed values is thus not possible to maintain with available tools but experiments should be able to tell trends and verify CFD simulations of the propeller model.

Static recirculation and ambient wind speed

Static testing of propellers introduces the problem of knowing the ambient wind speed V and the level of recirculation due the introduced flow of the propeller.

Considering a stepwise increase in propeller rotational velocity and produced thrust. At starting point the ambient wind speed is zero and circulation has not yet occurred. Then, considering the case where the propeller has run for an infinite time in a finite environment all flow would recirculate through the propeller. The initial flow field around a just started two bladed propeller was documented by PIV at static conditions in [18]. It is difficult to quantify at what state the ambient flow field is at a certain point after the propeller start.

Propeller Boundary Correction in Wind Tunnel

A propeller producing positive thrust in a closed wind tunnel such as Chalmers L2 produces a slipstream with a higher velocity than the ambient wind speed. Due to continuity the mass flow must be consistent over the cross-section of the closed wind tunnel, the speed outside the slipstream must therefore have a slower speed than the velocity upstream the propeller. The reduced speed around the slipstream will increase the static pressure relative to the free stream tunnel flow. If a large propeller relative to wind tunnel cross-section is used this effect can have a large impact on the propeller performance and would increase thrust output as if the ambient wind speed would be lower. This phenomena has been examined by Glauert in a [19] where the effect of this reduced wind speed can be found from:

$$\frac{V'}{V} = 1 - \frac{T/(\rho A_p V^2) A_p/A_{L2}}{2\sqrt{1 + T/(\rho A_p V^2)}} \tag{2.14}$$

Where V' is wind speed affecting the propeller, V velocity in the wind tunnel upstream and A_{L2} the cross sectional area in the test section.

2.3.2 Targeted Propeller Performance Indicator

There are four main indicators of propeller performance that the rig needs to be able to quantify: torque, power, propeller efficiency and turbo efficiency as shown in equation 2.6 to 2.8.

During static conditions propeller efficiency drops to zero since $V = 0$. Combining turbo machine efficiency with Actuator Disk Theory (ADT) and incompressible conditions as in equation 2.8 defined by Anna Lind[4] , it is possible to estimate the turbo efficiency of a propeller at static conditions. This makes it possible to compare efficiencies with a non-static case.

2.3.3 Accuracy and Precision

Defining and quantifying accuracy and precision in measurements is vital since no measurement can ever be exactly accurate [16]. Therefore it is important to identify the sources of uncertainties so they can be minimized.

Sensor Accuracy

The accuracy of each measurement has different impact on the final result depending of the order of the usage of the measurement. Studying the main interesting parameters and the usage of each measurement, the impact of each measurement can be quantified.

$$\alpha_{CT} \leq 1 + \alpha_T + \alpha_\rho + \alpha_n^2 + \alpha_D^4 \tag{2.15}$$

Looking at thrust coefficient accuracy shown in 2.15, errors in diameter α_D and rotational speed α_n would give a much larger impact than an error in the load cell

α_T. If conditions are perfectly stable, then timing is of no importance but since the aerodynamics of a propeller are by definition unstable the timing must be considered as a source of error when sampling from multiple sources.

$$\alpha_T = \alpha_{\text{Sensor}}\, \alpha_{\text{Source}}\, \alpha_{DAQ}\, \alpha_{\text{filtering}}\, \alpha_{\text{other}} \tag{2.16}$$

Many measurements have a large number of dependencies, such as the thrust measurement accuracy shown in equation 2.16 for a H-bridge load cell. The excitation source has some error in voltage deviation, the load cell has one accuracy, the analogue decoder has a finite resolution and the filter/statistical post processing introduces some error as well. Any source could therefore include a large number of errors and this reflects the need of high accuracy measurements at all levels.

Sensors or transducers normally have a non-linearity factor. This factor become very important for non-discrete linear measurements such as pressure and load transducers. The non-linearity is the deviation from the calibration curve and is defined differently for different supplier. Futek uses a maximum deviation expressed as percentage of the rated output on increasing load [20].

The accuracy of each individual measurement can for most sensors be quantified by the standard OIML (Organization Internationale de Métrologie Légale). NFW

Sensor Repeatability or Precision

The repeatability of data is dependent on sensor behaviour under load, ambient condition change such as temperature fluctuations and the ability to return to zero load. Different sensors have different limits of repeatability, and most manufacturers have different ways to quantify those. Sensor parameters used in this thesis main are the following:

Hysteresis is the measured difference when a set load is applied by reaching the set point either by lowering from a higher load by increasing from a lower load.

Creep is the measured difference during constant load for a longer period of time when all other ambient conditions are constant.

Temperature effects are the measured effects of temperature changes of the sensor.

Threshold point/minimal sensitivity is the minimal value the load cell can measure and this value can differ from the minimal resolution for some sensors.

Zero Reset error is the measured difference between before and after a test at zero point with slow load release.

Statistical Uncertainty

The accuracy of the input is one limit of the quality of a measurement, this limit can quite easily be calculated given data of each unit as shown above. There are more uncertainties at experimental data collection, which all can not be discussed here. At

any sample collection the aim is to get as close to the true value as possible; this can for instance be achieved by averaging over a number of samples. There are two major problems in this; it is hard to control whether the average value collected is offset from the true value with a bias, and it is hard to know what a sufficiently large sample size is. The bias offset can be due to calibration offset, zero reset values of sensor creep mentioned in the section above. One way to quantify the uncertainty of a mean value is to use confidence factors and sample until a required mean accuracy is reached. Sample mean and standard deviation are defined as:

$$\overline{x} = \frac{1}{n}\sum_{i=1}^{n} x_i \tag{2.17}$$

$$s = \sqrt{\sum_{i=1}^{n} x_i \frac{(x_1 - \overline{x})^2}{n-1}} \tag{2.18}$$

$$\beta_{cp} = \{\overline{x} - \Delta x < \mu < \overline{x} + \Delta x\} \tag{2.19}$$

Confidence can then be measured by using the probability that a mean value would be within a set difference $\pm\Delta x$, where $\Delta x = ks$ with k representing a confidence factor.

$$\beta_{cp} = \int_{-\Delta x\sqrt{n/s}}^{\Delta x\sqrt{n/s}} f_{tk}(y)dy \tag{2.20}$$

Equation 2.20 shows the relationship between a normal distribution $f_{tk}(y)$ and the confidence level for a given number of samples and sample standard deviation.

This method only works if the distribution does not exhibit periodic shedding that can offset the balance from the normal distribution. This can be problematic at propeller testing since samples will be periodic by their nature, both by aerodynamic blade loading and mechanical unbalance. The average and confidence level have to be approximated by another method then, or a method to neutralise the unbalance. A bias offset can be reduced by a number of methods including repeating very similar ambient conditions.

2.3.4 Vibration

Vibrations are due to mechanical imbalance, aerodynamic fluctuations due to blade load and from the power supply. Large vibrations can disturb the flow field around the airfoil, as well as the measurements. Vibration due to mechanical unbalance in any rotating part would have a periodic cycle and must be considered when sample rates are considered.

Mechanical Imbalance

There are three kinds of imbalance mentioned in various places: static, coupled and dynamic.

- Static imbalance is when the axis of inertia is parallel to the axis of rotation, like a non-centred disk on an axis.
- Coupled unbalance is when the axis of inertia crosses the center of gravity but is non-parallel with the rotational axis.
- Dynamical unbalance is when the axis of inertia is not parallel to the rotational axis nor intersects with the axis of rotation.

A schematic illustration is shown in figure 2.6.

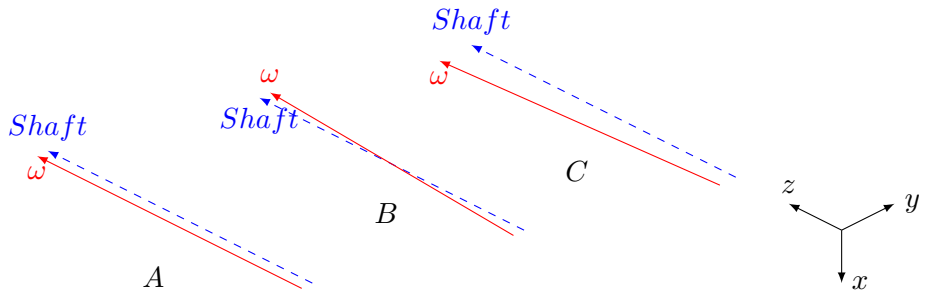

Figure 2.6: Different Types of Mechanical Unbalance

Let's assume that the axis of rotation is the z-axis in the Cartesian coordinate system. The angular momentum around the z-axis becomes:

$$\mathbf{L}_0 = -\mathbf{I}_{xz}\omega\mathbf{e}_x - \mathbf{I}_{yz}\omega\mathbf{e}_y + -\mathbf{I}_{zz}\omega\mathbf{e}_z \tag{2.21}$$

Calculating the time derivative:

$$m\ddot{\overline{x}} = F_x \qquad m\ddot{\overline{y}} = F_y \qquad 0 = F_z \tag{2.22}$$

$$-\mathbf{I}_{xz}\dot{\omega} - \mathbf{I}_{yz}\omega^2 = M_x \tag{2.23}$$

$$-\mathbf{I}_{yz}\dot{\omega} - \mathbf{I}_{xz}\omega^2 = M_y \tag{2.24}$$

$$-\mathbf{I}_{zz}\dot{\omega} = M_z \tag{2.25}$$

The static balance condition would be when the center of mass is on the rotational axis. Loads can still be induced by the torque of the M_x and M_y, and to reduce this, the inertia I_{zx} and I_{yz} needs to be zero. This is what is considered dynamical balancing, coupled unbalanced would be $I_{xz} = 0$ or $I_{yz} = 0$, but not both. Using equations 2.22 to 2.25, the mechanical unbalance can be quantified and possibly identified. The ISO 1940/1 [21] can be used to quantify unbalance.

Vibration due to Aerodynamics

Pressure difference as in wakes from wing profiles can produce a cyclic load on the blade that can introduce blade load. The geometry of the box-prop makes flutter unlikely but the cause of the blade load is still present. In an NTIS report [22] blade fatigue calculations are calculated by periodic load from this phenomena where maximum loads are at static start conditions.

2.3.5 Manufacturing

The surface texture of an object as designed does usually not correlate perfectly with the one of the manufactured object mainly due to the manufacturing process. The deviation from the designated surface may have different origins stated in [23] of some are:

- Error in form. This could arise as a deviation in straightness, planarity or roundness from the desired shape possibly, due to manufacturing or faulty handling.
- Waviness of the surface, possibly due to vibrations run-out, or form error of a milling tool.
- Roughness of the surface, due to manufacturing techniques leaving scratches, or marks in the surface or impurities during casting.

Figure 2.7 shows the surface profiles of aforementioned shape deviations.

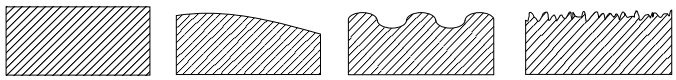

Figure 2.7: Overview of different deviations of shape, from left to right: ideal shape, error of form, waviness and roughness

For measuring roughness on an object, a profilometer is typically used which gives the arithmetic roughness R_a defined as

$$R_a = \frac{1}{n}\sum_{i=1}^{n}|y_i| \tag{2.26}$$

where y_i is the distance of the average height at measurement i and n is the number of measurements. The roughness profile may look similar to the one as depicted in Figure 2.8.

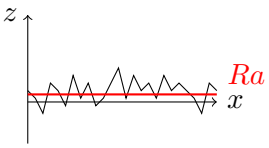

Figure 2.8: Representation of the arithmetic roughness R_a measured by a profilometer

Thus, the usual measured roughness height is R_a in microns, R_{RMS} and R_{zd} are also common. Further 3D scanning is available, which also produces a more detailed surface profile.

Leading edge defects

Airfoils are designed to accelerate air from the stagnation point gradually around both pressure and suction side. If the leading edge at the suction side has defects the acceleration can become larger than intended by design and local deceleration with separation or recirculation bubbles as a result This phenomenon has been numerically investigated for compressor airfoils in [24]. In [24] a physical description of the phenomena and an associated graph describing the velocity history along choord length at the suction side for a perfect and a non-uniform leading edge airfoil is illustrated. This graph is reproduced in Figure 2.9. For a perfect blade at the design point the velocity increases smoothly along the chord but for a non-uniform leading edge there is a spike in velocity followed by a rapid decreases below the normal that slowly recovers. At larger defects a recirculation bubble can occur where even a very small bubble may introduce early transition to turbulent flow. The result of this is a turbulent layer over a large part of the airfoil which increases skin friction and therefore the performance of the blade in general much like a grid line on a airfoil.

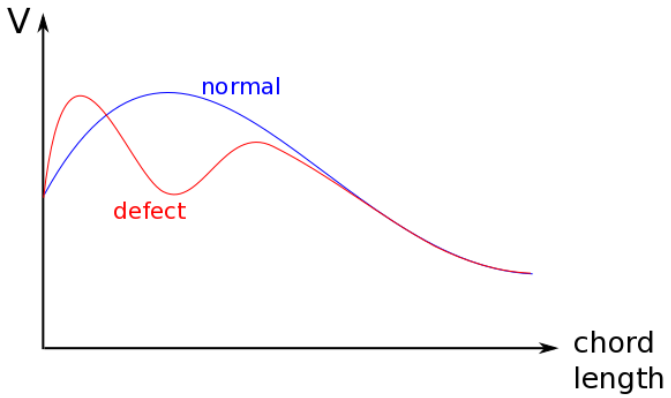

Figure 2.9: Velocity at suction side of the propeller from along the coord

Trailing Edge Discontinues

The trailing edge shape for airfoils and propellers have been investigated in the aerodynamic community for over a half decade. There is two ways to increase the trailing edge thickness, either by adding material on the diffusion side of the airfoil or by cutting off a part at the end of the chord. The later was investigated in [25] where a trailing edge increase of less than 0.5% of the chord was concluded to have small impact on the performance on a NACA 0009-64. The drag increase was increased rapidly by increasing the chord from trailing edge from 0.07% to 1.6% at lower lift coefficients. Airfoils with

increased chord thickness due to increased trailing edge have been studied in a NACA report from 1954 where investigation on non swept airfoils was studied [26]. The report shows among other things trends of rapidly increased drag on blunt trailing edges compared to sharp trailing edges, without large difference of lift in the 0.61 Mach range.

3

Methods

3.1 Basic design procedure

The main geometry of a Boxprop is generated using a Matlab script, the BBCode, first developed by S. Adriansson and further developed by A. C. Patrao. The main features of the BBCode are explained in previous Master Theses [1] and [2].

Input parameters are, *e.g.*, the propeller diameter, the number of blades, the blade profile, axial and chord displacement angles, sweep parameters and parameters defining the shape of the catenary stacking line. BBCode then generates the geometry in Matlab, as well as an Excel file with the points defining the Boxprop geometry that can be read into a CAD program.

3.1.1 CAD geometry

Catia V5-6R2013 by Dassault Systèmes has been used to generate a 3D geometry from points from BBCode. The points and splines have been imported to Catia using a modified Dassault Systèmes Excel script called "GSD_PointSplineLoftFromExcel.xls" which is included in all full Catia V5 installations. The script imports points and splines to generate a blade, the user then has to complete the hub and loft the splines. The coordinates of the points can be updated through Catia's design table and therefore the procedure to iterate similar blade geometry can be automated to an certain degree. If there is a change in points, probably due to a change in geometry, updating of the points might fail and thus corrupt the geometry due to a non-working loft command. The possibility of using Catia's design table and the increased control of import parameters motivates the change from the previously used Autocad Inventor in this project.

3.1.2 FE Analysis

FE analysis was used to check if there were any critical stresses or high level of deformations to the blade at different loads. Only loads resulting from rotational forces were considered in the FE simulations. A deformed geometry could be saved in .stp format, which makes it suitable for further usage.

3.1.3 Manufacturing

Catia V5-6R2013 has been used to design all non-propeller part such as mechanical supports. All in-house manufacturing has been done at Chalmers Prototype Workshop. Mastercam X8 has been used to generate g-code used to manufacture aluminium parts in the Haas mini mill and Haas ST-10 lathe. Makerbot replicator X2 has been used to produce supportive parts in Polylactic acid (PLA). The scatter shield has been manufactured by Plastmekano where the polycarbonate sheet has been bended at $180°C$.

3.1.4 CFD soft- and hardware

For the CFD simulations the softwares ANSYS Workbench and ANSYS CFX were used. This includes the DesignModeler, Meshing and Preprocessing modules in Workbench, as well as the Solver and Post-processing in CFX. The geometry files that have been imported into the geometry of the computational domain were either created in Autodesk Inventor (this applies for the 'old design' of the GPX313) or in Catia, which was the case for all geometries except the previous GPX313. The simulations were carried out on the cluster beda at Chalmers Centre for Computational Science and Engineering (C3SE).

3.1.5 Blade naming convention

There is two propeller series mentioned in this thesis, GPX (GKN Propeller Boxblade) and GPS (GKN Propeller Single Blade). There is a three digit number which is the model and iteration number. Occasionally a propeller ID for the manufactured propellers can be mentioned as well, *e.g.* GPX-313-B2.

$$\underbrace{\text{GPX}}_{\text{Series}} - \underbrace{3}_{\text{Model}} \underbrace{13}_{\text{Iterations}} - \underbrace{B2}_{\text{ID}}$$

Throughout this project, consistent naming of the blades has been used. Figure 3.1 shows the definition of leading blade and trailing blade, and also gives the wind direction, which is in negative x-direction. The rotational direction is positive along the x-axis.

3.2 CFD

This section deals mainly with causal research regarding the effects on the manufactured Boxprops but also presents new Boxprops.

All simulations were realised using ideal air at sea level conditions and at a temperature of $25°C$ and the following inlet conditions were used:

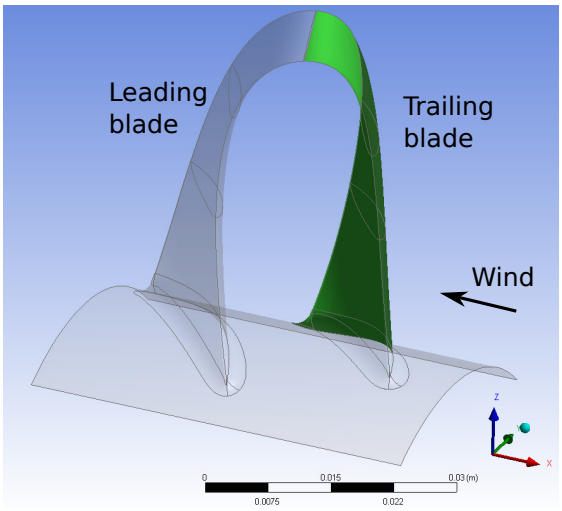

Figure 3.1: A single blade of the Boxprop with a marked trailing blade, showing the definition of leading blade, trailing blade and the incoming wind direction. The rotational direction is positive along the x-axis.

- $T_{stat} = 298.2K$
- $p_{stat} = 101325Pa$
- $a = 340.3^{m}/_{s}$

The inlet wind speed and the rotational speed varied depending on the case simulated. The simulations were all steady state simulations using the SST turbulence model with automatic wall functions in fully turbulent conditions. The interface between the rotating 3D domain and the non-rotating 2D domain (as shown in Figure 3.3) is a frozen rotor interface and the side walls use periodic boundary conditions, as only one blade of the propeller needs to be simulated. The here referred 2D domain needs to be attributed a thickness in CFX, but is treated as two dimensional.

3.2.1 Studies involving the GPX313

GPX313 is the design which was developed in previous Master Thesis works. To solve and understand the discrepancies between the simulation and experimental results, existing simulations developed by PhD-student Alexandre Capitao Patrao and based on the first CFD simulations on the Boxprop by A. Lind [4] have been taken as reference. The purpose is also to confirm the geometry and mesh that are used work fine. This is to be sure that further CFD simulations can be done in this way. There are two different computational domains depending on the inlet velocity, thus denoted high speed and low speed case. The studies that have been realised concern the roughness of the propeller blades, the wall functions used within the SST turbulence model, a mesh study, a variation in rotational speed, and a CFD simulation of the deformed GPX313. Also realised

was a study of the nacelle geometry, requiring the construction of a new computational domain. Not realised were studies using a difference turbulence model, a domain study or different discretisation schemes. The main parameters from the reference cases mainly used in the following studies are given in Table 3.1.

Table 3.1: Main parameters of both reference cases, high speed and low speed

Parameter	High speed case	Low speed case
J	0.77	0.15
Number of cells	33760200	39990508
Rotational speed	2722.714 $^{rad}/_{s}$	2722.714 $^{rad}/_{s}$
Blade walls	smooth	smooth

The low speed case uses a larger domain than the high speed case which explains the increased number of cells. Also, the number of cells is only valid for the 'old GPX313'. After changing the CAD-software from Autodesk Inventor to Catia, the number of cells increased due to adjustments at the trailing edge and the fillets connecting hub and blade. A comparison between both methods did not yield different results, thus using the new Catia model should not have disadvantages. Mostly, the old design was used for the GPX313 studies, unless stated otherwise in the respective section.

Roughness

Since it was assumed that roughness might play a major role in the performance of the Boxprop, but no measurements of the actual roughness could be realized in the beginning of the project, a range of different values for the equivalent sand roughness was chosen. Different roughness values in the range from $k_{s,eq} = 5\ \mu m$ to $k_{s,eq} = 70\ \mu m$ were applied to the blade and blade hub geometry in CFX-Pre. This has been done for the existing high speed and low speed domain, as different results were expected for different wind speeds.

All cases used the automatic wall functions that are integrated in ANSYS CFX. To implement the surface roughness in ANSYS CFX, the boundary condition of the blade had to be switched from smooth to rough walls with the respective equivalent sand roughness $k_{s,eq}$. Apart from this, neither geometry, mesh nor further set up has been changed with respect to the reference cases.

The use of larger roughness values would require to change from automatic to scalable wall functions in ANSYS CFX which need to be edited in CLL. This has not been done since there was no indication that larger roughness values would be needed due to missing roughness measurements on the manufactured propellers and the lack of an ultimate correlation between the measured roughness and the equivalent sand grain roughness

Near wall mesh resolution study

In the simulations, the turbulence model used was the SST $k-\omega$ turbulence model. This model uses the low Reynolds number formulation as long as $y^+ \leq 2$, otherwise wall functions are used. To estimate the effect of the wall function on the high speed reference case, a total of five cases have been studied where the initial total height of the inflation layer has been maintained but the first layer height and the number of layers were changed. An overview of the changes made with respect to the reference case is given in Table 3.2, Case0 being the reference case.

For the reference case, $y^+ < 2$ was achieved except at a small area at the leading edges of the blade. Thus it can be assumed that the low Reynolds number model is used throughout the reference case. Although the first case (Case1) has slightly higer y^+ values than the reference case, they are also mostly within the $y^+ \leq 2$ limit and thus also employ the low Reynolds number model. All other values have a mean $y^+ > 2$, therefore wall functions were utilised.

Table 3.2: Overview of parameters used in the simulations to verify the wall functions

Case	Total number of elements	First layer height	Max. layers	Mean y^+
Case0	33760200	0.000001	22	0.4
Case1	31670618	0.000002	19	0.9
Case2	28770195	0.000005	15	2.1
Case3	26623098	0.00001	12	4.3
Case4	24535512	0.00002	9	8.5
Case5	21443228	0.00005	4	19.2

The change in inflation layer is depicted in Figure 3.2, showing the reference case and two cases with reduced inflation layer resolution, Case3 and Case5.

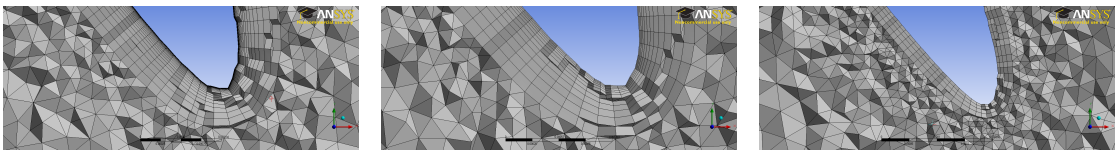

Figure 3.2: Representation of the inflation layer at the leading blade for 3 different cases: the reference case which is Case0, Case3 and Case5 from left to right.

Bulk flow mesh resolution study

The mesh study has been realised using the high speed reference case. The domain, as it is for the reference case, is shown in Figure 3.3. It can be seen that it consists of different subdomains and it is assumed that it makes a difference whether all meshing

domains are treated evenly or only one or two of those domains are changed. Different combinations of mesh size variations have been tested. The computational domain is divided into two main areas, an outer non-rotating and an inner rotating domain, as can be seen in Figures 3.3 and 3.4. The outer domain is the thinner surrounding area, using a hexa mesh with the thickness of one element which is solved as 2D by CFX. Since the Boxprop has five blades in its present configuration, the inner domain comprises one fifth of the propeller, which is subdivided into the blade disk with the blade itself, an upstream as well as a lower and upper downstream area. The mesh sizing is fine at the blade disk, medium at the lower downstream area, and rough at the upstream and upper downstream area. Also, the face sizing of the hub in the entire inner domain and of the blades as well as of the outer domain can be adjusted. The original values are given in Table 3.3. Inflation layers are used to maintain $y^+ \leq 2$ at the hub and the blades.

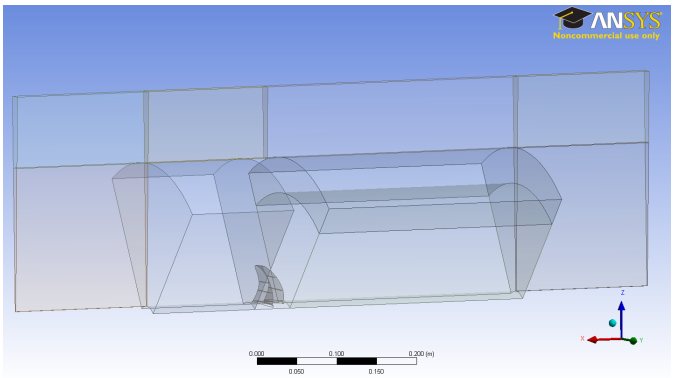

Figure 3.3: Computational domain for the high speed reference case GPX313. The height and width of the different areas *i.e.* upstream, blade disk, downstream, and outer area are given in function of the blade height. The flight direction is to the left.

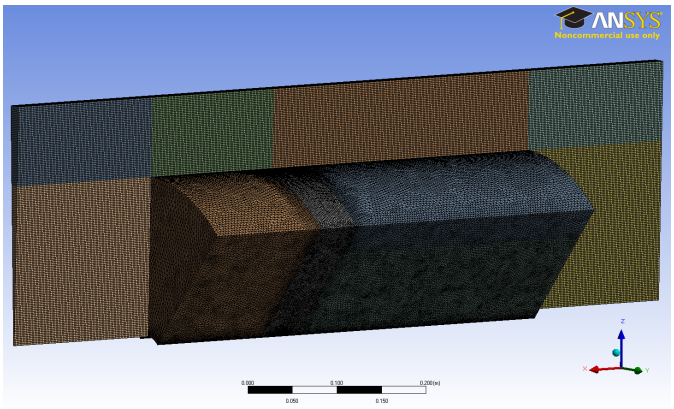

Figure 3.4: Mesh for the high speed reference case GPX313. The 3D domain is built up on an unstructured mesh whereas the outer 2D domain is built up on a hexa mesh. Again the flight direction is to the left.

In this mesh study either the body sizing or the face sizing were changed according to Table 3.3. The inflation layer was left unchanged with respect to the reference case since the influence of the inflation layer has already been considered in the wall functions study (see Section 3.2.1).

Table 3.3: Sizing settings for bodies and faces used in the mesh study

	Body sizing			**Face sizing**		
Case	**fine**	**medium**	**rough**	**Hub**	**Blade**	**Outer area**
original Case	0.002	0.003	0.004	0.001	0.00012	0.002
GPX313 - 1	0.003	0.004	0.005	0.001	0.00012	0.003
GPX313 - 2	0.003	0.004	0.006	0.001	0.00012	0.004
GPX313 - 3	0.0025	0.0035	0.0045	0.002	0.00015	0.0025
GPX313 - 4	0.004	0.005	0.006	0.002	0.00015	0.004
GPX313 - 5	0.003	0.004	0.005	0.0015	0.00013	0.003
GPX313 - 6	0.001	0.002	0.003	0.001	0.0001	0.001

Variation of rotational speed and wind speed

In the experimental tests, the propellers were mostly run with a rotational speed of 13000 rpm to decrease the risk of accidentally breaking them. To correlate the wind tunnel tests with simulation results, two main studies were realised: one maintaining an advance ratio of $J = 0.77$ and varying the rotational speed and the wind speed, and another for a varying advance ratio at a fixed rotational speed of 13000 rpm. For these cases, the reference low speed domain was used with the GPX313 geometry created in Catia.

The cases that were realized with a constant advance ratio used either a common divisor for both the wind and rotational speed with respect to the reference case. The values that were used in the simulations for constant advance ratio are given in Table 3.4.

Table 3.4: Overview of parameters used in the simulations to study the variations in rotational speed for a constant advance ratio of $J = 0.77$

Parameter	**Case1**	**Case2**	**Case3**	**Case4**
Wind speed in $^m/_s$	5	12.5	45	37.5
Rotational speed in rpm	2600	6500	13000	19500

Results from simulations with a constant rotational speed and varying wind speed

can be compared directly to a testing session in the wind tunnel for a constant rotational speed. Therefore a range of cases has been prepared as shown in Table 3.5 that fill the gaps between the already simulated cases of $J = 0.15$ and $J = 0.77$ and go up to the maximum advance ratio for the GPX313.

Table 3.5: Overview of parameters used in the simulations to study the variations in wind speed for a constant rotational speed of 13000 rpm

Parameter	**Case1**	**Case2**	**Case3**	**Case4**	**Case5**	**Case6**
Wind speed in $^m/_s$	9.8	14.6	19.5	22.5	27.6	29.9
Advance ratio	0.3	0.45	0.6	0.7	0.85	0.92

Including protective scatter shield

The propeller test rig includes a scatter shield for safety reasons. This is supposed to have an influence on the results from the experimental tests. In order to establish this influence, a new domain was created including the scatter shield. The scatter shield is integrated using the smallest distance from the propeller as the radius of the shield and including the whole length of the shield which can be seen in Figure 3.5. Here, the scatter shield is the marked area, forming the boundary between the three dimensional inner and the two dimensional outer domains. Since the computational domain is much larger with the scatter shield included, only the blade disk area is realised with an unstructured mesh, including an inflation layer to save computational costs. This blade disk area is then swept to the upstream and downstream areas, which creates a prism mesh and also includes the inflation layer. In the second step, the lower 3D area is swept upwards, creating a hexa mesh in the upper upstream and downstream regions and a prism mesh above the blade disk. The advantage of using the sweep function is that the inflation layer which is set up in the blade disk area for the unstructured mesh is automatically also swept and does not need to be adjusted for the hub in the inlet and outlet area, which caused meshing errors from time to time. The disadvantage may be that a prism mesh is usually used for boundary layer flow, and less for free flow, thus it may be less accurate as a hexa mesh. Since the main areas of interest are the blade and the global flow, this is neglectable. To have a smooth transition between the different mesh sizings and methods, the sweep function is refined at the source face and is coarser at the target face. This is applied to the lower inlet and outlet area, the upper area is refined at the source and target face. The set up for this case is similar to the previous case, except that the scatter shield boundary will be treated as a wall in this case.

Effect of finite nacelle geometry

In addition to the scatter shield, the nacelle that holds motor, load cell and the mounting device has an influence on the flow field. This is valid for the static rig as well as for

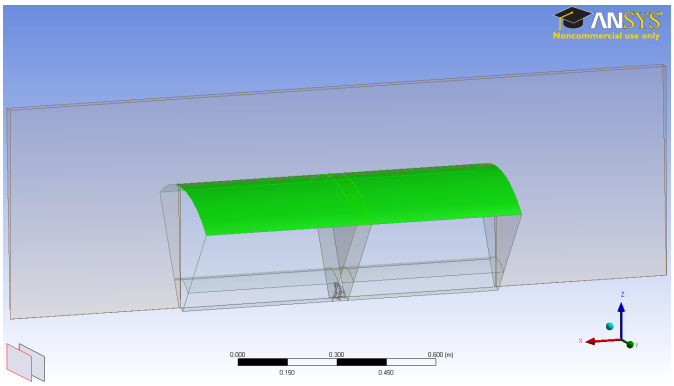

Figure 3.5: Geometry of the computational domain including the protective scatter shield. The actual shield, that is implemented as a boundary condition, is marked. The flight direction is to the left.

the wind tunnel tests, since it is always mounted. In order to reproduce this effect, the large domain generated for the scatter shield simulations, as presented in Section 3.2.1, has been modified in the upstream and downstream area. The domain mainly does not have a hub surface any more, except for the Boxprop blade disk section, and the size, especially the height, was slightly reduced to avoid high Mach numbers at the top of the rotating domain. The geometry of the nacelle has been drawn, revolved and substracted from the lower upstream and downstream areas as shown in Figures 3.6 and 3.7.

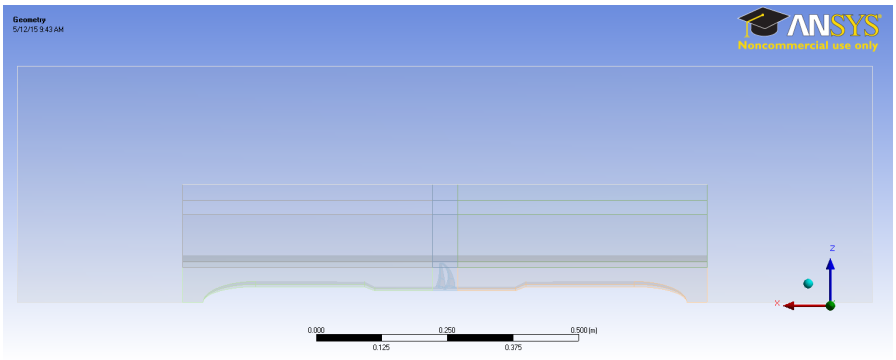

Figure 3.6: Geometry of the computational domain including both the upstream and downstream nacelle. The geometries for both nacelles are identical, but opposing each other. The flight direction is to the left.

The meshing of this geometry was done as an unstructured mesh in the lower part to be able to include the geometries of the nacelle, blade and hub accordingly. Since the use of an inflation layer is not possible for unstructured meshes if adjacent to hexa meshes, the unstructured mesh from the lower part has been swept to the upper part, resulting in a hexa mesh this time due to a different meshing order. The mesh of this case can be seen in Figure 3.8, showing mostly the rotational domain. A close-up is given in Figure

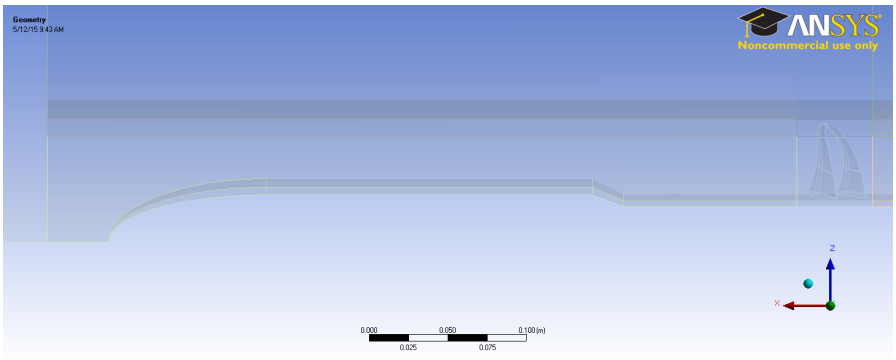

Figure 3.7: Close up on the upstream nacelle. The flight direction is to the left.

3.9, showing the unstructured mesh in the lower part and the hexa mesh in the upper part. Also the 2D outer domain can be seen, with a thickness of one cell over the whole height of the domain.

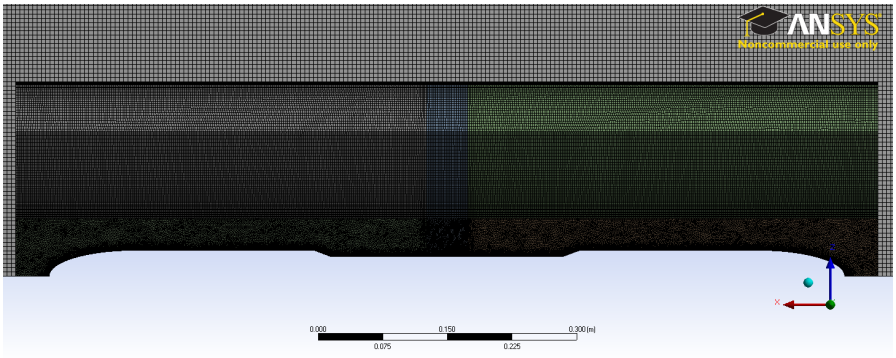

Figure 3.8: Meshed geometry including the nacelle. The lower 3D part is meshed using an unstructured mesh and the upper 3D part is meshed using the sweep function. The 2D outer area is meshed using a hexa mesh. The flight direction is to the left.

Roughness and Nacelle geometry

Since data from the surface measurements was available at the end of the project, a short study could be realized. The measurements were taken at four different points of the propeller, on the inside and outside of each blade. The results from these measurements are shown in Appendix B. As the effect of the roughness is assumed to be different for pressure and suction side, it was decided to weigh the suction side with $^2/_3$ and the pressure side with $^1/_3$. Afterwards, the correlation from Flack and Schultz [15] was used, which yielded an averaged surface roughness of $k_{s,eq} = 21\ \mu m$. This was then implemented in the domain using the nacelle geometry, an inlet velocity of 25 $^m/_s$, and a rotational speed of 13000 rpm to match it to the experimental tests. Thereafter, further cases have been realised, with the same rotational speed but an inlet velocity of 19.5 $^m/_s$

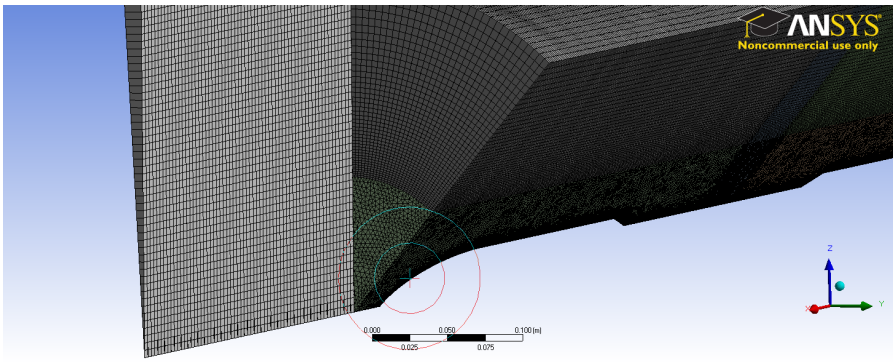

Figure 3.9: Close up on the meshed geometry including nacelle, showing the unstructured mesh in the lower part and the swept mesh in the upper part as well as the 2D outer mesh.

and 29.9 $^{m}/_{s}$ to obtain values for $J = 0.6$ and $J = 0.92$, respectively.

3.2.2 GPX316

GPX316 was designed similar to GPX313 but with 0° cone angle. The cone angle is the angle of the blade tip relative to the flow field. For GPX313 the cone angle is 13°. Also, both blades do not have the same angle of attack, thus the blade angle is different for leading and for trailing blade.

3.3 FE Simulations

ANSYS 15 statical structural - Mechanical has been used for all FE Simulations. A single blade has been simulated to reduce the number of cells. For the axisymmetric boundaries a frictionless support has been used. The boundary at the contact with the axis has been simulated as fixed. The geometry was imported in the format STEP AP214E2.

3.3.1 Material Model

The material data that has been available in Polyjets material datasheet [27] was used together with a standard linear elastic model. Creep has not been simulated.

3.3.2 Mesh

Since FE simulations were used for both mechanical stresses as well as CFD support both aspects had to be considered. The demands from mechanical stresses and deformation were much lower than to achieve similar surface resolution on the deformed mesh as for the original one. Shown in Section 2.3.5 the leading edge has a large impact of the performance of a wing profile and to be able to make a good estimation of the leading edge a high enough number of elements has to be present to capture the shape. The

blade profile is generated by a spline of points with approximately 0.008 mm in distance at the shortest distance. An edge length would therefore be of similar amplitude to be able to track the surface with the same accuracy close to the original blade.

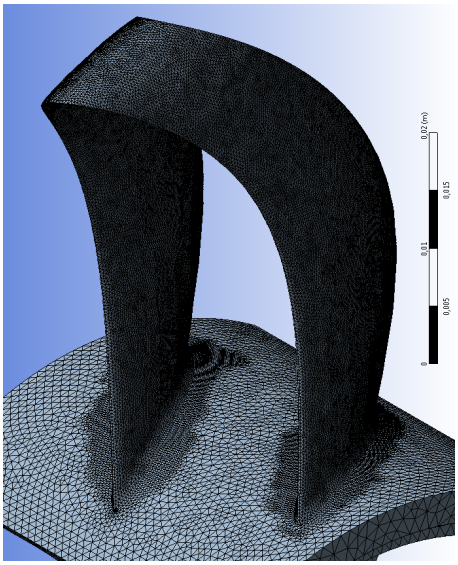

Figure 3.10: Mesh for the a single Boxblade

The face size on the boxblade was 0.00029 m and a size of 0.001 m on the hub. The number of elements of the final mesh was 744491 with 1109014 nodes.

3.3.3 Scripts

Some automated scripts have been used to be able to export result data to FE modeller. First a Javascript was used to name all body surfaces automatically. The naming was necessary to mark the nodes on which the deformation should be tracked on. An APDL (ANSYS Parametric Design Language) script marked and tracked the nodes that were connected to a surface that was named and then exported as a .cbd file. The automated javascript was provided from ANSYS Helpdesk as well as the settings to make the .cbd export.

3.3.4 Exporting Deformed Mesh

Different workarounds and tutorials were tried to export the mechanical deformation to CFD before one method that worked for our geometry was found. A reoccurring problem was to track or generate the blade profile, since it is mathematically complex to regenerate in deformed shape even though it was cut down in many small sections. Exporting the part as a ParasSolid failed since FE solver did not manage to track the surface correctly. The method that was used to export the deformed mesh to CFX was to read the .cdb file with ANSYS 15 FE modeler consisting only of surface nodes of

the deformed blade. FE modeler identified and created surfaces and exported it as a .stl file. The original blade geometry was afterwards deformed to fit the deformed mesh with local average deviation of less than 0.01 mm. The exported deformed geometry and the manually deformed geometry can be seen in Figure 3.11. The yellow surface is the manually deformed and the black mesh is the exported deformed blade. The leading edge difference between mesh and deformed geometry can be seen as large. This is an illusion due to the mesh consisting of straight lines inside a curvature and therefore the visualisation will be small or not visible at all.

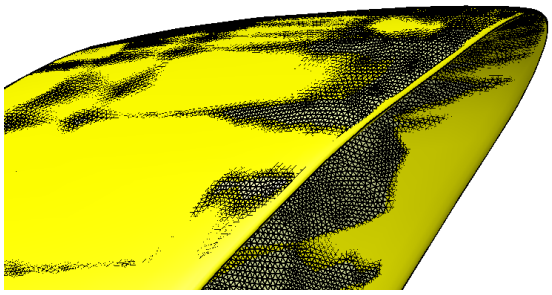

Figure 3.11: Comparison between FE mesh and manually deformed geometry

3.4 As-manufactured defects

The defects of the manufactured propeller were investigated as a source of potential error between simulated and experimental results. The deviation from the CAD geometry can have multiple impact on the experimental results shown in the theory chapter and some can be directly critical causing propeller failure during test. Some internal defects could be identified by visual inspection by using LED light to shine through the material. Trailing edge defects could also be seen by visual inspection. All measurements of geometry and surface roughness were done by external suppliers, some parts of the reports are attached as appendices. The growth of the inner diameter due to creep was measured in-house.

3.4.1 3D Scanning

Manufacturing defects were measured with an Atos Core Mv 300 3D scanner. The accuracy of the scan is 0.01 mm and has a point cloud resolution of 0.12 mm. A .stl file and a report from the scan was delivered by Digital Mechanics.

3.4.2 Surface Roughness

The surface roughness was measured by the Toponova instrument where the surface was measured with Surfascan 3CS delivered by Jenoptik. The blade was measured on pressure and suction side of lead and trailing blade at a near constant radius of 67 mm for the 0.15 m diameter GPX-313 in RGD850. The measurements were taken from trailing edge to leading edge with an offset to ensure a near flat surface for the surface probe. The measurements complies to ISO 3274 with an Ra error of $\pm 5\%$. A conical tip with a radius of 2 μm with a force of 2 mN was used for measurements.

3.5 Experimental Setup

3.5.1 Overall View

Propellers made out of Verogray RGD850 and RGD525 and of diameter 0.15m were tested in both a static rig seen in Figure 3.12b, and propellers of RGD850 of diameter 0.3m and 0.15m were tested in Chalmers L2 wind tunnel seen in Figures 3.12a and3.12c at Chalmers University of Technology. The central part of the rig consists of two counter rotating mounted propeller mounts. The propellers are driven by two BLDC motors mounted on a bi-axial load cell capable of measuring torque and thrust. A H-bride NI decoder, NI-6327 is used to log the load cell values and a 10V external power supply is powering the load cells. A Hall sensor mounted on one of the motors power supply is used to detect the rotational speed and is logged using a NI-6211 and power by a 5V external supply. The motors are controlled with an electronic speed control (ESC) using a PWM signal from the NI-6211. The NI-6211 together with thermocouples are used to log the temperature of the motor and load cell. The ESC is a modified Fulcrum 300A-Pro with increased cooling to be able to work under higher RMS currents than original. Rig control, wind tunnel control, sampling and logging are done in Labview 2013, running test programs made in Matlab 2014 and writing logs to text files. Particle Image Velocimetry (PIV) has been used to document the flow field in the wake of a GPX-313 and GPS-101. Propeller diameters varied from 0.15 m to 0.3 m and the rotational speed from 2200 rpm to 28000 rpm.

In the static case everything is mounted on an aluminium frame with a 12 mm polycarbonate scatter shield. During wind tunnel testing 25 mm plexiglass windows function as protection.

3.5.2 Thrust and Torque Measurement

The thrust and torque are measured with a bi-axial load cell of model MBA500-FSH00747 delivered from Futek mounted between the motor mount and the pilot tube shown in Figure 3.13. The sensor is rated for 100 lbs thrust and 100 lbs-inch in torque, excitation voltage of 10 V and rated output of 2mv/V. Exact data for the sensor can be found in the data sheet [28]. A calibration certificate was delivered with 10 points in the 50 lbs and 50 lbs-inch range of the load cell which was used to convert input voltage to physical

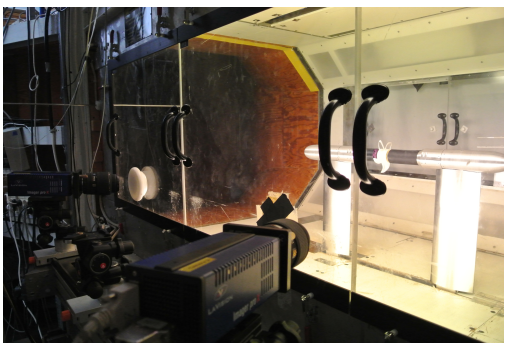

(a) 0.15m Wind Tunnel Setup

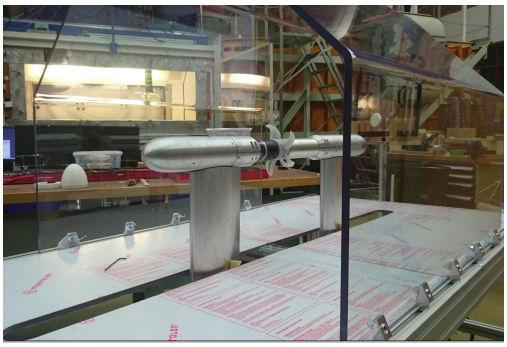

(b) Static Testing Rig

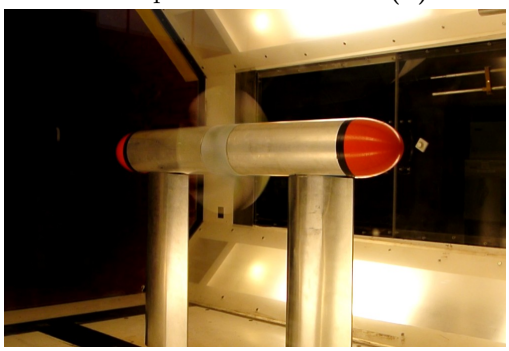

(c) 0.3m Propeller

Figure 3.12: Experimental rig setups

values using:

$$F_i = \frac{V_{out}}{V_{rated}} F_{rated}\, c_i \tag{3.1}$$

F_i is the converted load, V_{out} is the sensor output voltage under load, V_{rated} is the voltage corresponding nearest rated load, F_{rated} is the corresponding load and c_i constant to convert to preferred physical unit. The rated load is taken from the provided certificate. At full range the load cell has a finite minimal resolution, a reduced measuring range reduces the accuracy by a factor ξ which is the ratio between the rated output for the sensor F_{rated} over the range that the experiment is conducted F_{range}. All Futeks MBA sensors have a specified non-repeatability constant of 0.0005. The non-repeatability values are the maximum error measured between two identically conducted tests:

$$\xi = \frac{F_{rated}}{F_{range}} \tag{3.2}$$

The output from the load cell was measured with a H-bridge sensor NI-6237 which can power 150mW in total at four channels. This is not sufficient since one channel consumes 286mW at 10V calculated from the NI-9237 data sheet [29]. Therefore a lab

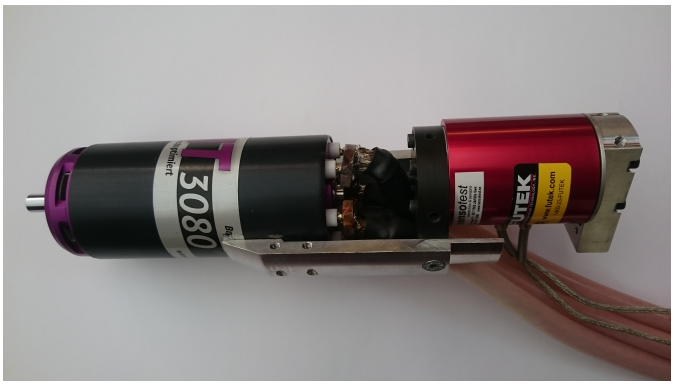

Figure 3.13: Load Cell mounting

linear power supply was used as excitation power for the load cells.

Since the load cell is mounted so it supports the whole propeller and motor assembly the static load had to be considered. The stresses on the load cell were calculated using methods supplied by the manufacturer using a weighted equation of loads on the load cell:

$$\sigma_{max} =\leq 447F_x + 526F_y + 218F_z + 266M_x + 255M_y + 212M_z \tag{3.3}$$

There are three stress levels given by the manufacturer for a life cycle of 10- to 20 million cycles. There is the static maximum load σ_{stat}, fatigue load with non-reversing load σ_{nr} and full reversing load σ_{fr}. If the stresses are below 75% of the given stress values the load cell should hold for more than 100 million cycles. The stress levels from for the sensors used are shown in Table 3.6.

Table 3.6: Table of maximum stress levels taken from [30]

Material	σ_{stat}	σ_{nr}	σ_{fr}
2024-T4 Futek	28000 psi	18000 psi	15000 psi
Static Case	11100 psi	11100 psi	0 psi
Increase per $10m/s^2$	0	5777 psi	5777(-5692)psi

The static load is at 51.4% maximum load and considered not critical. The reverse and partly reverse loads can be critical since large vibration have been measured in previous years. The peak values would be when vibration forces are directed in the same way as the gravitational forces. Such a load case is not fully reversible but offset from zero load by the loads of gravitation. The fully reverse loads would be at peak vibrations minus the gravitational force since then the bias is around zero. The non-reverse stresses σ_{nr} therefore consist of peak loads from vibrations and gravitational forces while fully reverse load σ_{fr} consists of peak vibration loads minus the gravitational forces. A critical

vibration level can then be calculated given the static case.

Temperature of the load was logged during the testing to be able to identify errors and approximate cooling time needed between test cycles.

During load the load cell suffers from creep. The creep due to the load of the propeller load is very low since a very low range of the load cells rated output is used. There is though creep from the static load but that was only noticed during longer periods and by continuously resetting the load cell to zero between each measurement this error could be minimized.

3.5.3 Measuring Rotational Speed

The rotational speed was measured with a circumferential current transducer off model HASS 200-S mounted on one supply cable from the ESC to the electric motor. The sensor outputs a voltage proportional to current through the supply cable and this is required as an analogue input to the National Instruments USB-6211 version. The sensor has a minimal sensitivity of $0.625 = V_{inst}/I_{PN}$ with $V_{inst} = 12V$ and $I_{PN} = 0.036A$ in our lowest setting and a maximum rated RMS values at $200A$. The sensor has only been used for steady state conditions, and response time has not been of major concern. The HASS 200-S merely requires 5 μS to reach 90% step of I_p. The frequency bandwidth of the transducer is 50 kHz well above our needs with a highest frequency of $866.667Hz$. The sampling frequency of the NI-6211 was set to 50 kHz, to match the frequency of the transducer, and to be able to study the behaviour of the ESC at different load.

The RPM measurements were controlled with a optical RPM measuring device from Biltema after the rig set up was changed to ensure correct RPM measurements.

3.5.4 Hub Pressure Difference

During testing it was noticed that very small changes in distance between hub and trailing nacelle had a large impact in measured thrust. To compensate for this error pressure probes were installed in front and behind the propeller. The installation of the pressure probe could not be on the surface of the hub due the lack of possible guide channels, therefore the probes were installed near the surface behind and in front of the hub as shown in Figure 3.14. The front probe was also fitted as close to the center as possible so rotational swirl in the hub would have a lower interference. A FCO510 was used to measure the pressure difference and the results from a test with a polished GPX-313 is shown in Figure C.3. The force correction is then calculated by taking the pressure difference times the area of the hub.

3.5.5 Measuring Vibrations

Vibrations were measured with a SDL800. The unit meets the ISO2954 accuracy, it measures RMS and peak value and can log data both to a SD-card and serial by RC232. The maximum vibration frequency is 10 kHz. It has a remote magnetic adapter that has been mounted vertically on the upper side of the motor at the calculated point of gravity

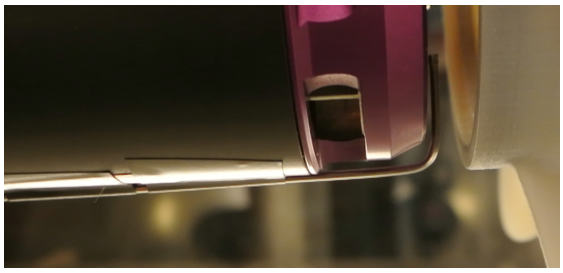

Figure 3.14: Front Pressure Probe

of the load cell supported mass. The sensor has been used to measure vibrations in static case. The sensor would disturb the flow field in the wind tunnel and was therefore not used in there.

3.5.6 Motors, Motor Control and Power Supply

All motors powering the rig have been provided by Lehner-Motoren-Technik, who mainly provide high power density BLDC motors to high end model builders. Motor models 3080/6 and 3080/8 have been used, where the first two digits are the series, the next two describe the model and the final digit is the number of windings. The 3080/6 was replaced by the 3080/8 later in the project when a larger torque demand arose due to an increased propeller diameter. The rated data is presented in Table 3.7, where the † marking shows rated values based on testing the motor in a load cycle that simulates a RC-boat race with their in house cycle. Both motor models were set-up in a star configuration during all testing.

The ESC used was a modified Fulcrum-300A+ Pro. This unit is rated up to $350A$ instantaneously and $300A$ continuously. The ESC overheated with the normal air cooling system included. A modification was introduced to increase the cooling capability by mounting a OTS CPU cooler with a cooler mount in aluminium. The ESC is controlled by a 8 kHz PWM signal with a 15-20 ms period representing 0-100% load.

Four 12 V led-acid batteries of model RS-689-5863 capable of $100Ah$ each were used to power the rig.

3.5.7 Data Acquisition

Labview 2013 was used as an interface to the rig. Large time scale averaging methods were used, so acquisition did not need to be well timed between different sources. Thereby statistical analysis could be determined by the nature of the source and fairly independent of processing time and sampling timing.

The DAQmx tabular calibration tool was used for conversion to physical units from load cells and thermocouples. The express averaging function was used to filter the load-cell input signals. The rotational speed was gathered continuously with a sample rate of 40 kHz and a sample size of 10000. The VI square wave produced the period which a combination of trimmed mean values and median was used to determine the RPM.

Table 3.7: Motor, ESC and Power supply rated continuously output to the left and maximum at output at 26000RPM to the right

	$T_{cont^*}[Nm]$	$P_{cont^*}[Kw]$	$RPM_{cont^*}[10^3]$	$Volt$	amp	$T_{max}[Nm]$	$P_{max}[Kw]$	$RPM[10^3]$	$Volt$	amp
3080/6	2,7	10	35	40	261†	4,2	11.6	26	30.6	400
3080/8	3,0	8.8	28.9	44	212†	4,3	11.7	26	41	301
Pro+ 300A	-	-	-	60	300	-	-	-	60	350
RS-689-5863	-	-	-	44.4	250⋆	-	-	-	44	600

† Lehner 10 second cycle, ⋆ 6 min continuously

Selected values have been written to a log file every 0.4 second and .csv files have been used to load in program runs to the program. The general schematics of the Labview program is: first all constants for each input and output are set up, thereafter the GUI is started together with data collection and transmission. Log files are written from the first moment. The signals from the NI-9237 device were sampled continuously with DAQmx at a rate of 50 kHz and sample size of 30k. Communication with the wind tunnel and the lab rig took place with Labviews share variables over a local network.

RPM

Pulses acquired from the hall sensor were analysed by a VI-square wave acquisition tool where a square wave was detected by percentile rising edge of 70% with a 15 % negative pulse adjacent before. The negative value trigger before the rise was necessary to capture the main back EMF that occurs once a revolution. Different method to sample the rotational speed were tested with trimmed mean, mean and median; a long sample size with median was by far the most stable and accurate value but needed a few seconds to acquire a big enough sample size and can only be used for steady state tests.

Ambient Conditions

During wind tunnel sessions ambient pressure and temperature were measured with a Furness FCO510 Micronanometer. The same unit was used combined with a Pitot-pipe directed against the flow direction in the inlet of the test section to measure wind speed at the inlet to the test section.

Miscellaneous logged values

During all testing the temperature of the motors and motor controllers was measured with type T thermocouples using analogue input on the NI-6211.

Uncertainty of Sources

The level of uncertainty for input sources are presented in Table 3.8. The values are presented in percentage which are based on conditions in operation point (OP). The operation point is either based on where the largest error is found or based on typical advance ratio $J = 0$ or $J = 0.77$, shown in the table as $case_{J=0.77}/case_{J=0}$. If an isolated test of a sensor has been performed it is presented in column Iso.t and Iso.T % where the first column shows the absolute value and the second one shows the percentage at OP. In column Test the values or error during testing is displayed.

Table 3.8: Uncertainty of each measurement input measurement for worst case values

Load Cell

Source	OP	Suppl.spec	Iso.t	Iso.t %	Test %
Excitation V	$10V$	0.001	$\pm$0.01	$\pm$0.1 %	$\pm$0.1 %
Force N	6/40 N	$\pm$0.2	$\pm$0.01	$\pm$0.17 %	0.297 % std
Torque Nm	0.2/2 Nm	$\pm$5.65e-3	-	- %	0.266 % std

Rotational Velocity

Source	OP	Suppl.spec	Iso.t	Iso.t %	Test %
Hall Sensor S/s	$867S/s$	$\pm$2e-5	-	- %	$\pm$3.85e-3 %

Ambient Conditions

Source	OP	Suppl.spec	Iso.t	Iso.t %	Test %
Pitot tube m/s	$0.6/40m/s$	0.25 %	-	- %	†
Pressure Pa	$100kPa$	0.25 %	-	- %	†
Temperature K	294,15K	0.25 %	-	- %	†

Analogue to digital decoding

Source	OP	Suppl.spec	Iso.t	Iso.t %	Test %
NI-9237 Force mV	$0.023mV$	$2.29\mu V\star$	$\pm 0.3962\mu V$	$\pm$0.17 %	0.297 % std
NI-9237 Torque	$0.016mV$	$0.168\mu V\star$	-	- %	0.266 % std

OP=Approximated operational point, † = Only averaged data, −= No test conducted, $\star$ NI Absolute accuracy without noise factor

Uncertainty of Dimensionless Coefficients

Using equation 2.15 the accuracy of each measurement was quantified. The accuracy is divided in three parts, measurement uncertainties which would provide a random bias offset (Source 1), uncertainties that would create a constant bias offset (Source 2) and error if assuming all compensation is faulty (Source 3). In Table 3.9 the uncertainties

for each dimensionless number have been quantified using values mainly from Table 3.8, some values are approximated and the accuracy of those are discussed in Section 5 . FE simulations have been assumed to be ±30 % wrong in deformation.

Table 3.9: Uncertainties of Dimensionless Numbers

	Source lvl 1	Source lvl 2	Source lvl 3
C_T	±0.51 %	±1.24 %	3.82 %
C_P	±0.49 %	±1.39 %	5.25 %
η_{prop}	±0.77 %	-	9.07 %
η_{turb}	±1.16 %	±1.18 %	11.07 %

−= No Valid data

3.6 Experimental Procedure

Experiments have been conducted very early during the thesis work to evaluate the status of equipment and material from previous thesis work. This work will only briefly describe important old tests and focus will be on the final testing procedure.

3.6.1 Propeller Evaluation

Before any tests the propeller was studied for visible damages. Common defects on the blade were irregular trailing edges and tip crack damages from manufacturing. If tip crack damages were detected the propeller was not used for testing but for other purpose as surface measurement. Blades that had trailing edge irregularities were still used but under closer surveillance during stress since an already bad trailing edge could loose more parts and thereby increase the unbalance of the propeller.

During testing the amplitude of periodic load could be seen in the load cell raw input graph in Labview and by documenting amplitude while testing at a set load an increased vibration could be seen. If there was a change in sound characteristics the test was stopped immediately.

Creep has been measured in the inner diameter of the propeller where an increased diameter by test time was noticed early in the test program and was afterwards documented together with runtime. The inner diameter was measured with a curricular inner t-spool and an external micrometer.

3.6.2 Balancing

Propellers and hub were balanced manually using the Du-Bro 499 Tru-Spin Prop Balancer. The balancing was done with either adding material or sanding away material from the balancing ring added to the hub. The method employed was to first balance the

statical balanced. The statical unbalance could be done in the RC-Balancer. The reason for balancing propellers was that large vibration was measured with the old testing rig and it was noticed that larger vibrations were measured with propeller than without propeller. Balancing the propeller and redesign a new hub mount with higher tolerances between the propeller and the hub reduced the peak vibrations. The main source of vibrations with balance propeller and new hub is the motor vibrations and the hub and propeller have a dampening effect due to increased inertia.

3.6.3 Polishing Blades

Polishing blades was done manually by submerging the blade completely in water and sanding with 3M Scotch-Brite Light Gray Ultra fine. The sand roughness of 3M Scotch-Brite correlates to a grit of 800-1000. Each surface was polished evenly by 30 passes. Areas with a higher surface roughness was then further polished until a even result was achieved. To avoid blade angle defects due to polishing, it was made sure that traces of the printing process was visible evenly. A comparison taken with a WiKi USB Digital Microscope of a non-polished and a polished (40 passes) surface made at the pressure side of the root trailing edge on the trailing blade can be seen in Figures 3.15a and 3.15b respectively. The pictures have increased contrast and decreased brightness to emphasise the structure.

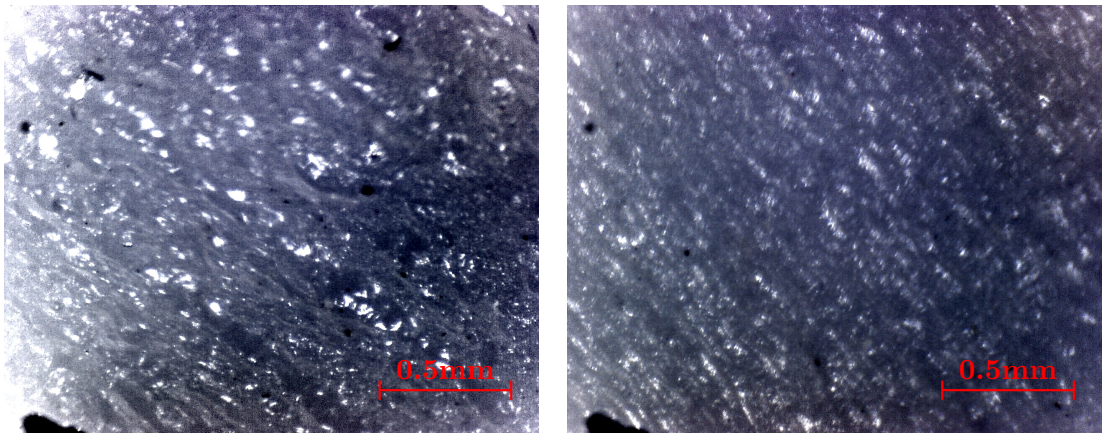

(a) Non-polished blade surface **(b)** Polished blade surface

Figure 3.15: Surface Difference Between Polished and non-polished surface

3.6.4 Calibration

Sensor calibration has been described in each section respectively. The calibration was repeated between both wind tunnel sessions and after bigger change in test programs. Thermocouples have been calibrated using three know temperature points at accuracy of 0.5 degree. The accuracy of the thermocouples did not have a large impact since they were mostly used for temperature difference.

3.6.5 Test Program

The test program was loaded to Labview through a .csv file where each row represents a input value. There were both binary and numeric value inputs. Binary values were: load sensor reset, RPM sampling start and force sensor sampling start and program running. Values that could be set was target RPM, wind speed and time for each interval. This method avoids large labview programs and simple changes can be made in the preferred text editor or program.

1. When started the program checks if temperature for motor and motor controller is below maximum and that the RPM sensor is not reading any RPM.
2. Force reset is set to high and starts to reset load cell values to reach a value in range of e-6.
3. The motor and the wind tunnel is started and the RPM is set to a near zero thrust at current wind speed.
4. The RPM sensor is started ad 2000-6000RPM dependent on configuration and the motor is accelerated to target values.
5. Statistical analysis is started at the RPM input.
6. The main sampling starts after a set time when stable conditions are reached.
7. The propeller RPM is lowered to a near zero thrust state again to cool the motor.
8. The motors stops when near wind zero speed is reached.
9. At zero wind condition the temperature of the motor is checked the error of the load sensors are measured and the program restart from point two again until all values have been iterated.
10. Program shuts down and put output values to zero and stops writing to log.

During the mounting of the propeller the load cell is completely detached from supporting elements. The PIV setup and procedure is mentioned in its own section.

3.6.6 Static Condition Testing

Test procedures in the static rig differ from wind tunnel sessions due to the lack of controlled ambient wind speed and that the load is higher on the motors and load cell during all test at the same RPM in the wind tunnel. There is no ambient wind speed so the motors are constantly under load while running the propeller statically. This means that during the cooling cycle the propellers are still loaded and cooling is delayed compared to wind tunnel sessions.

During a propeller test the flow field around the propeller is unclear and constantly changing. This makes it impossible to use long time scale sampling method and the

accuracy of sampling both load cell data and RPM are reduced. The sampling domain is reduced by a factor of 20 since below this value vibration noise was picked up.

Testing of previous equipment has been done under static conditions and later only propeller vibration and blade stress tests by exceeding the planned test speed by 20% have been realised. Blade deformation can be measured in the static rig using a triggered PIV signal.

3.6.7 Chalmers L2 Wind-tunnel testing

The Chalmers L2 Wind-tunnel is a closed loop, closed cross section with a $2.08m^2$ octagonal cross section of dimensions 3.0 $m \times 1.8$ $m \times 1.25$ $m(L \times W \times H)$. The maximum wind speed is $60m/s$ with a contraction ratio of 5.86:1 [31]. The main fan diameter is 2 m having a 6 bladed rotor powerered by a $170kW$ motor. The main fan is followed downstream by stators used as motor support and for cooling the main motor by evacuate hot air through the stators. Fresh air is injected by a $50kW$ cooling fan. Inlet flow temperature is regulated by an intercooler before injected in the main stream. The temperature is thus kept within one degree difference. The rear end of the test section has a breather slot of 20 mm to equalise the pressure. The tunnel is controlled by a Labview 2012 program where the fan mixture levels and wind speeds are set by the operator. The turbulent intensity at the test section was measured before the tests conducted in this thesis by Chalmers Applied Mechanical internal resources and was found to be approximate 0.01%. The test result are attached in Appendix A. The coordinate system used in the wind tunnel is defined as a propeller mounted in pusher configuration using a propeller coordinate system defined in Section 3.1.5. The propeller center was mounted in the center in the X,Z direction. The Y distance from the floor was 0.55 m.

3.7 PIV - Particle Image velocimetry

The PIV technique was used to track the slipstream flow of the propellers at take-off condition. Oil droplets with a diameter of 0.5-1 μm have been used as PIV tracer particles. These have been generated by a fog generator of Smoke Factory DATA || with the fog fluid water-glycol mixture SWEFOG Netural-Pro HD Smoke Fluid. The system has been LaVision GmbH Stereo PIV system FlowMaster with the recording and processing program DaVis 8.2.2.

3.7.1 Optics

The two cameras were Imager Pro x 4M with a resolution of 2048 $\times$ 2048 pixels of a 7.4 μm pixel size and 14bpp. The cameras were equipped with SIGMA AF 105mm f/2.8 EX DG MACRO lenses with LaVision Scheimpflug correctors. The recording frame rate was $5Hz$ in the PIV double frame regime. The seeding particles were illuminated by the second harmonic 532nm of a pulsed Nd:YAG double-head laser of the brand Quantel EverGreen EVG00200 with 200 mJ per pulse with a duration of $10ns$. A 2 mm thick

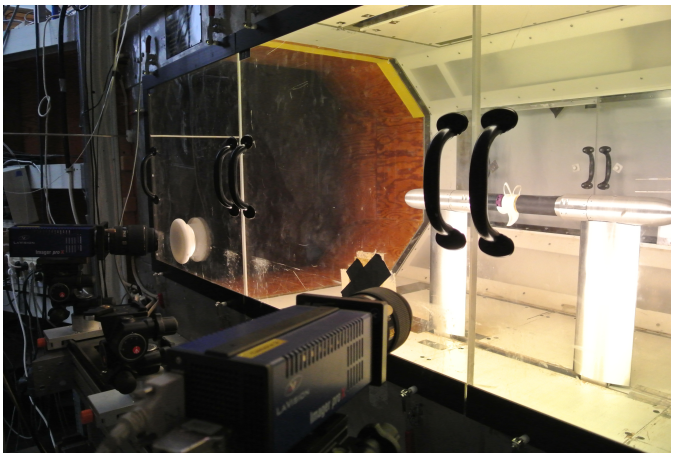

Figure 3.16: PIV Setup in Wind Tunnel

laser sheet was generated by LaVision sheet optics with a cylindrical lens. The time delay between two PIV frames was 40 μs. An raw picture from the camera mounted downstream can be seen in Figure 3.17.

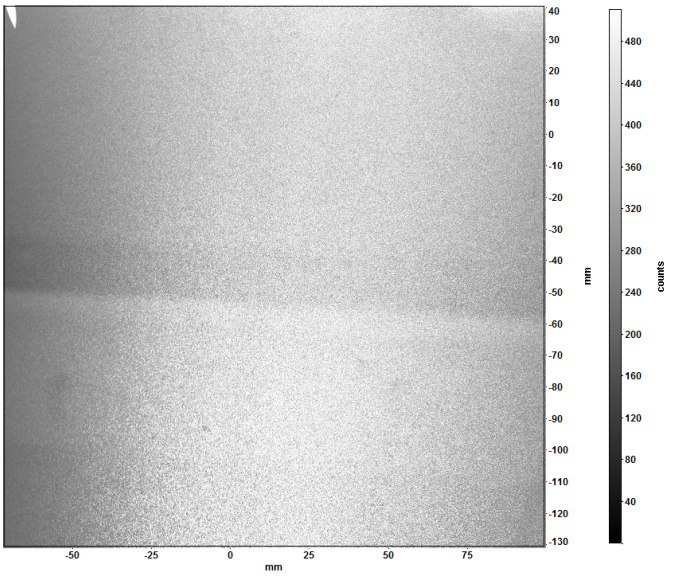

Figure 3.17: PIV Setup Camera capture frame

The physical camera set-up was a ±20 degree offset from z axis in the xz-plane, and can be seen in Figure 3.16. The optical system was calibrated with a double-sided, double plane LaVision calibration target Type 11. To avoid reflection from propeller and details downstream the propeller such as nacelle, black OTS lacklustre paper of $89 g/m^2$ was used to cover the shiny aluminium surface and cameras were adjusted just below the hub and propeller.

3.7.2 Processing

The PIV processing was done with an iterative multi-grid correlation algorithm combined with stereo reconstruction procedure. Four iterations were used, with a final integration size of 16×16 pixels with a 50% overlap between adjacent domain cells. For averaged values a sample size of 100 instantaneous velocity fields were used.

3.7.3 Experiential Procedure

The wind tunnel was filled with smoke with a wind speed of $3m/s$ and low external air mixture rate so as to not disperse the smoke. The PIV unit was used to continuously control the smoke level until a sufficient amount of particles could be tracked. At the correct level of smoke in the wind tunnel, the mode for the wind tunnel was changed to an 20% fresh mixture rate to have a overpressure in the wind tunnel and the wind speed was increased to a near $25m/s$ and the rotational speed to 13000 rpm. After stable conditions were reached, 100 images were captured as described above. The data was then processed and exported as a comma-separated values text file including time and velocities, and also saved as image files.

4

Results

This chapter presents the results from both the CFD simulations and the experimental tests.

4.1 CFD

4.1.1 Studies involving GPX313

Roughness

The correlation between major performance values and the surface roughness was studied for high speed and low speed cases. The high speed case uses an advance ratio of $J = 0.77$, while the low speed case uses an advance ratio of $J = 0.15$. Figures 4.1 and 4.2 show the results for $J = 0.77$, normalised against the reference case. Figure 4.1 displays the trailing blade, leading blade, and whole blade thrust for increasing equivalent sand roughness. It can be seen that for increasing equivalent sand grain roughness, $k_{s,eq}$, there is a light increase in the trailing blade thrust, opposed by a more obvious decrease in the leading blade thrust. This is also reflected in a decrease of the total blade thrust. In the range from 40 to 70 μm equivalent sand grain roughness, the thrust is approximately constant.

As can be seen from Figure 4.2, both the whole propeller and the turbo efficiency drop drastically with increasing equivalent sand grain roughness $k_{s,eq}$. The turbo efficiency drops by 12% for $k_{s,eq} = 70$ μm compared to the smooth reference case, and the whole blade efficiency by 9%. Since the blade thrust decreases for increasing roughness, so does the coefficient of thrust. Also, the coefficient of power experiences a light increase, just as the torque is increasing.

Figure 4.3 shows the main performance parameters for the low speed case with $J = 0.15$. Here the same trends are identifiable but less intense. The whole blade thrust is not depicted, but the trend is the same as in Figure 4.1 before, with a light increase

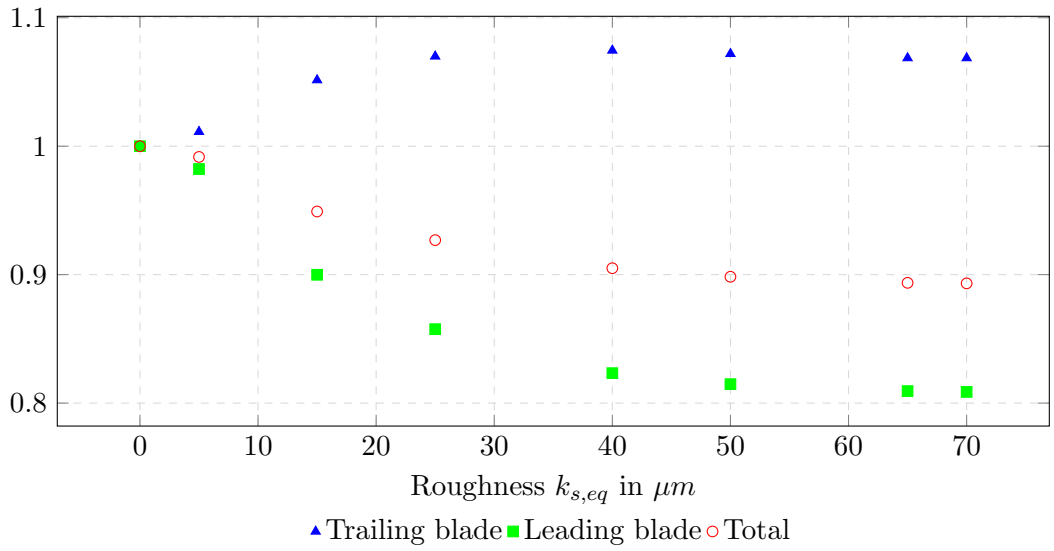

Figure 4.1: The thrust of trailing blade, leading blade, and the whole blade normalised with the smooth reference case for different equivalent sand roughness $k_{s,eq}$ at $J = 0.77$

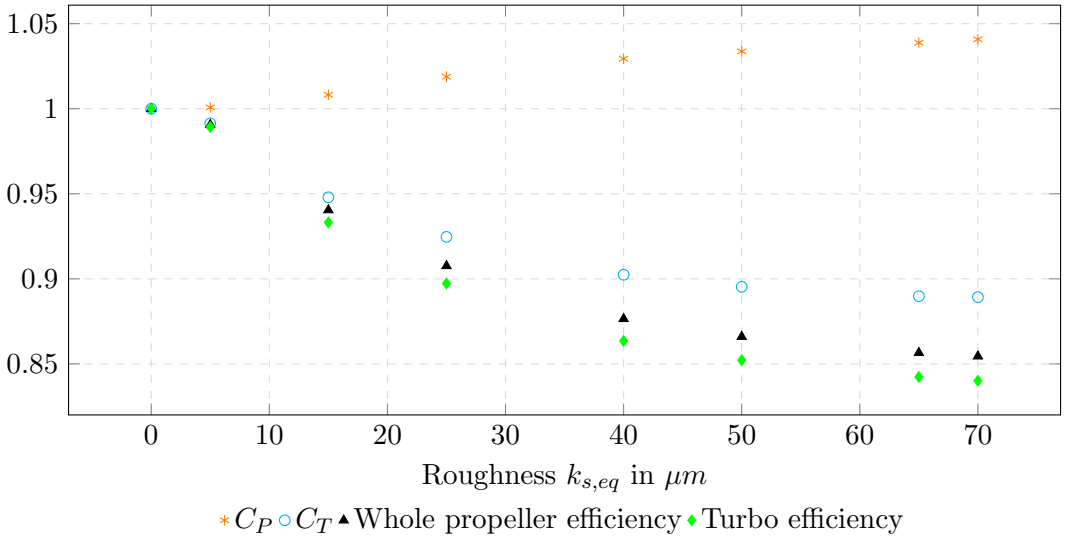

Figure 4.2: Performance parameters normalised to the smooth reference case for different equivalent sand roughness $k_{s,eq}$ at $J = 0.77$

in trailing blade thrust and a decrease in leading blade and thus total thrust which is less intense for the low speed case compared to the high speed case presented earlier. The efficiencies are also slowly decreasing as before, but with a lesser intensity compared to the high speed case as they loose less than 8% with respect to the reference case. Again, C_T decreases, and C_P increases with increasing roughness, but this is also less intense than in the high speed case. It can be observed that the parameters are slightly

unsteady as were thrust and torque since the simulations did not converge exactly to a steady state, and that consequently the performance parameters vary slightly depending on from which timestep they were evaluated.

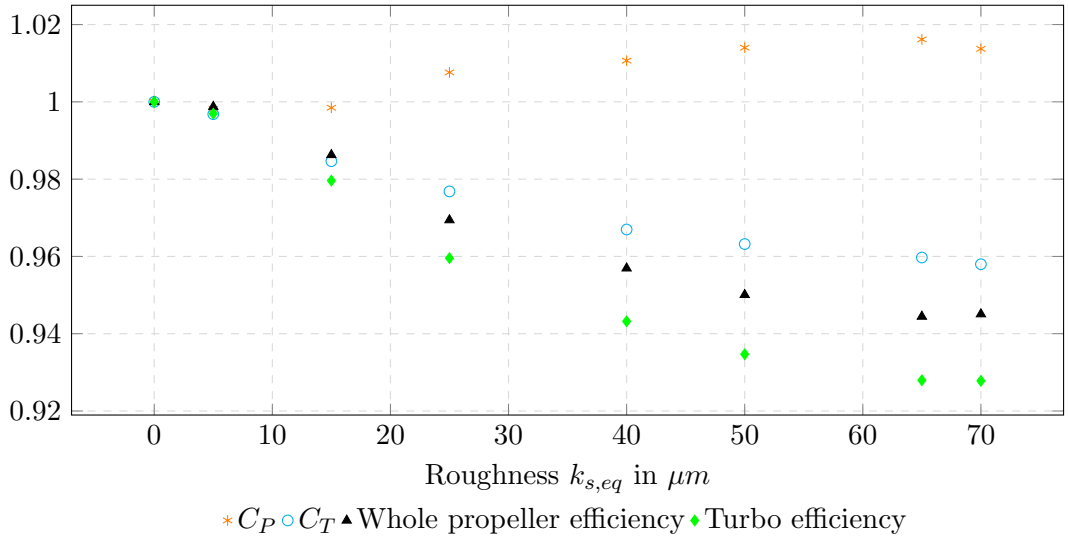

Figure 4.3: Performance parameters normalised with the smooth reference case for different equivalent sand roughness $k_{s,eq}$ at $J = 0.15$

Figure 4.4 shows the contours of the Mach number for the smooth case and a case with an equivalent surface roughness of $k_{s,eq} = 65\ \mu m$ at $J = 0.77$ and 60% propeller radius. Both cases seem quite similar concerning the overall distribution of the Mach numbers. The leading blade (blade to the left in the Mach number plots) has accelerating flow on the suction side as well as a small area of a higher Mach number than the free stream Mach number behind the leading edge on the pressure side. The trailing blade also has accelerating flow on its suction side as well as on most of its pressure side, originating from the flow field of the trailing blade. One difference between both plots is a larger area with a Mach number that is higher than the free stream Mach number on the leading blade pressure side for the case with a higher roughness. The more obvious difference is the shape of the wake after both leading and trailing blade. The wake itself is about twice as thick for the rough case and the turbulent boundary layer starts building up much earlier.

Figure 4.5 shows the same cases but this time at 95% propeller radius, close to the joined blade tips. The overall tendency is similar to Figures 4.4 described earlier, in particular considering the development of the wake behind the blades. It can also be noticed that the local Mach numbers at the blades are now higher, since the plots are taken at a larger radius.

Figure 4.6 illustrates the sectional thrust on each blade section at various radii up to 95%. It can be seen that the pressure in x-direction on the trailing blade is up to 16 $^N/_m$ less for the rough case than for the smooth case at the same conditions. The difference

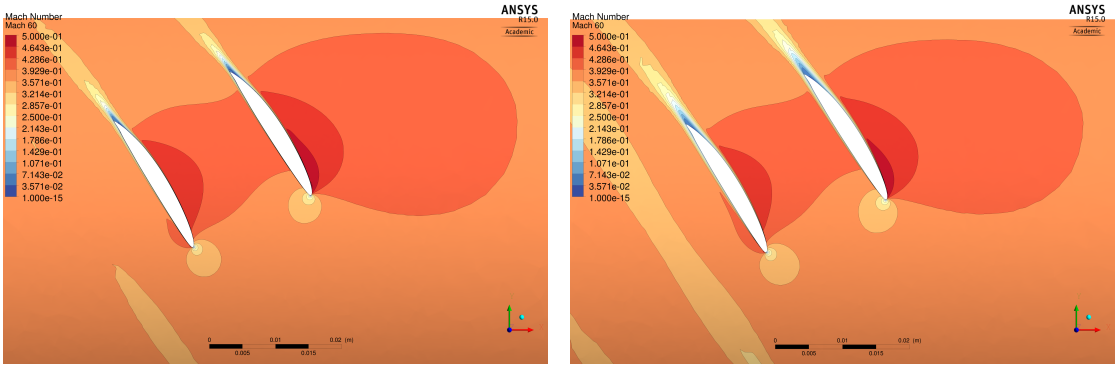

Figure 4.4: Contour of Mach number at 60% of propeller radius for a smooth case ($k_{s,eq} = 0$, $J = 0.77$) on the left side and a case with equivalent sand roughness of $k_{s,eq} = 65\ \mu m$ at $J = 0.77$ shown on the right side. The flight direction is to the right in both cases.

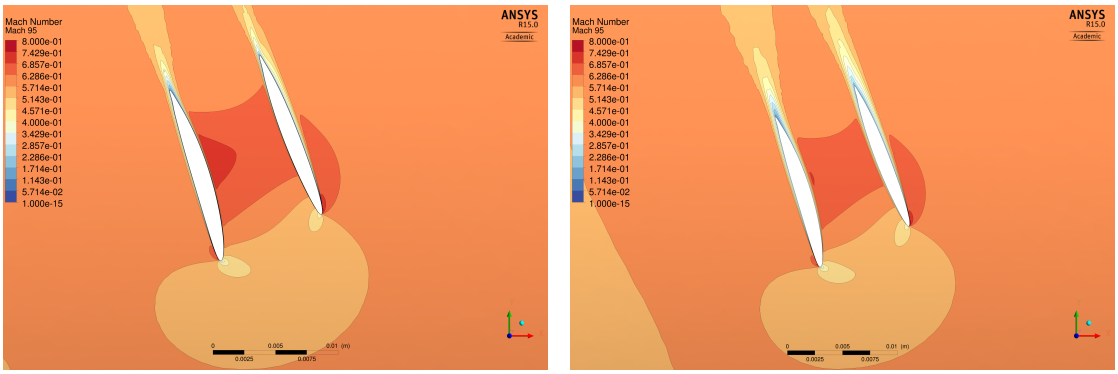

Figure 4.5: Contour of Mach number at 95% of propeller radius for a smooth case ($k_{s,eq} = 0$, $J = 0.77$) on the left side and a case with equivalent sand roughness of $k_{s,eq} = 65\ \mu m$ at $J = 0.77$ shown on the right side. The flight direction is to the right in both cases.

on the leading blade on the other hand is less serious closer to the hub with a difference of about 3 $^N/_m$ until 65% of the propeller radius is reached. Here, the rough propeller actually outperforms the smooth one by up to 11 $^N/_m$. Values below $^r/_R = 0.41$ are not included as it is the hub geometry only. The same applies for the values $^r/_R = 0.95$ to $^r/_R = 1$ which is the blade tip area.

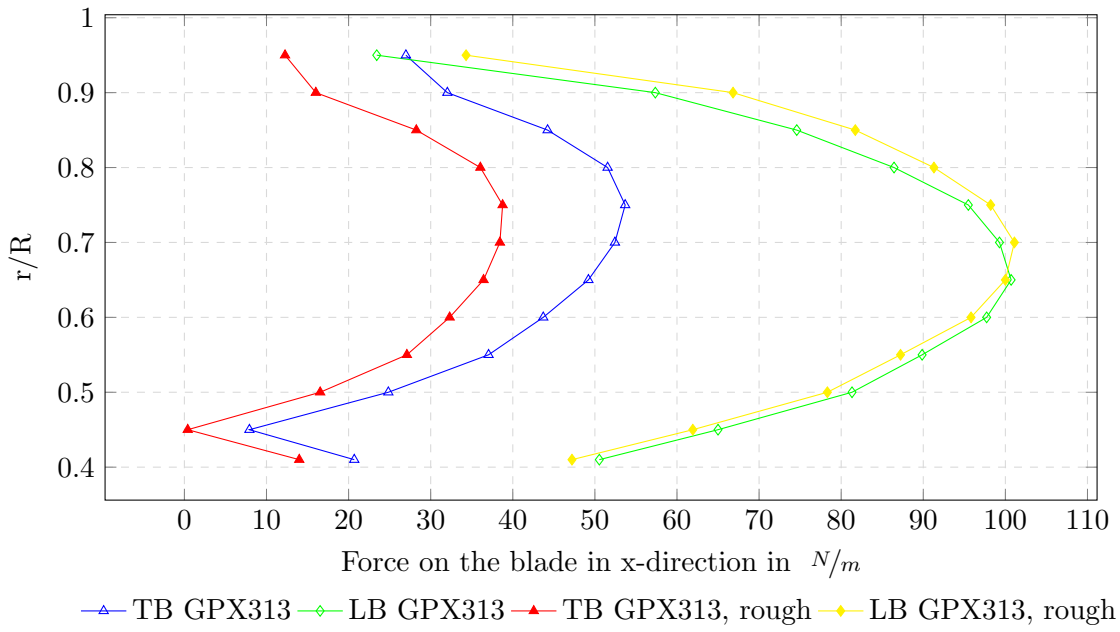

Figure 4.6: Force on the leading blade (LB) and trailing blade (TB) in x-direction for a smooth and rough ($k_{s,eq} = 65$) case run with $J = 0.77$

Near wall mesh resolution study

Table 4.1 shows the main results for all cases presented earlier in Table 3.2 and Figure 4.7 shows the performance parameters for all cases. The blade thrust is almost constant for the first three cases, but increases for Case4 and Case5. Both the whole blade as the turbo efficiency are almost constant until Case3 but increase rapidly for Case4 and Case5. This points to an overestimate in propeller and turbo efficiency when using the automatic wall treatment. Neither the coefficient of power nor the coefficient of thrust show a clear tendency up to the fourth case. Only for Case5, a rapid increase in both coefficients, C_P and C_T, is visible which is according to the torque and thrust values, respectively.

Bulk flow mesh resolution study

The mesh study as described in Section 3.2.1 did not give apparent differences in thrust or thrust and power coefficients and efficiencies. All performance parameters are within a limit of $\pm 1\%$ of the reference case.

Table 4.1: Comparison of main results for the near wall mesh resolution study at $n = 26000rpm$ and $V = 50\ ^m/_s$, Case0 is the reference case.

Parameter	Case0	Case1	Case2	Case3	Case4	Case5
Total propeller thrust $[N]$	23.32	23.36	23.40	23.31	23.47	24.52
C_P	0.25	0.25	0.25	0.25	0.25	0.26
C_T	0.20	0.20	0.20	0.20	0.20	0.21
η_{prop} [%]	59.1	59.3	59.6	59.6	60.2	61.9
η_{turb} [%]	71.7	71.9	72.3	72.2	73.1	75.6

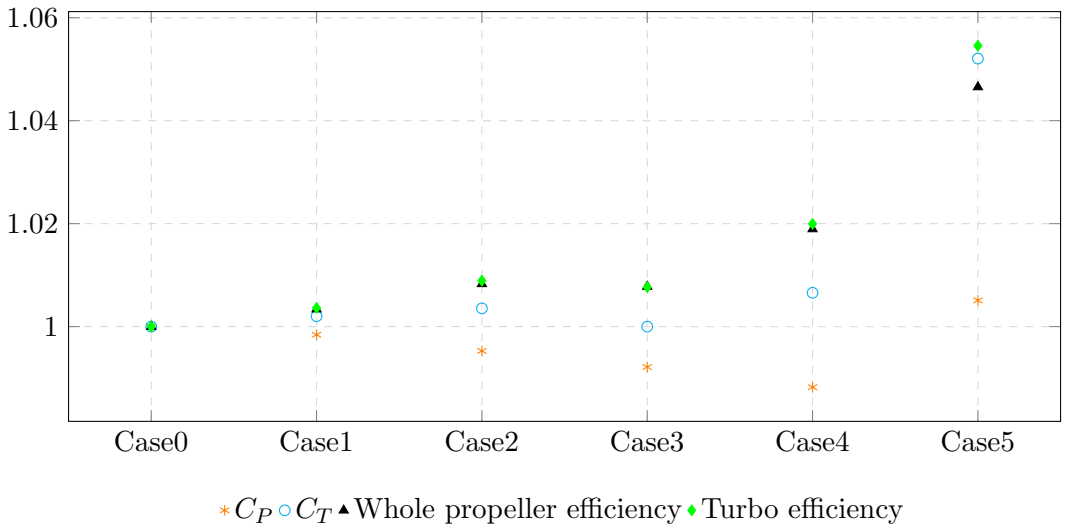

Figure 4.7: Performance parameters normalised with the reference case using different inflation layers at $J = 0.77$

Variation of rotational speed and wind speed

Figures 4.8 and 4.9 represent plots of the thrust and the performance parameters at a constant advance ratio of $J = 0.77$. It can be seen that the thrust increases slowly with increasing rotational speed and wind speed. All performance parameters increase rapidly from very low values in the low rpm-range and then slowly approach the reference values. Figure 4.10 gives a more detailed view of the high rpm-range. The largest difference between 13000 rpm and 26000 rpm concerns C_T, and is less than 6%.

The results for the simulations with variation in wind speed with constant rotational speed are presented together with the measured values in Section 4.3 for better comparison with the experimental data and are also used as further reference.

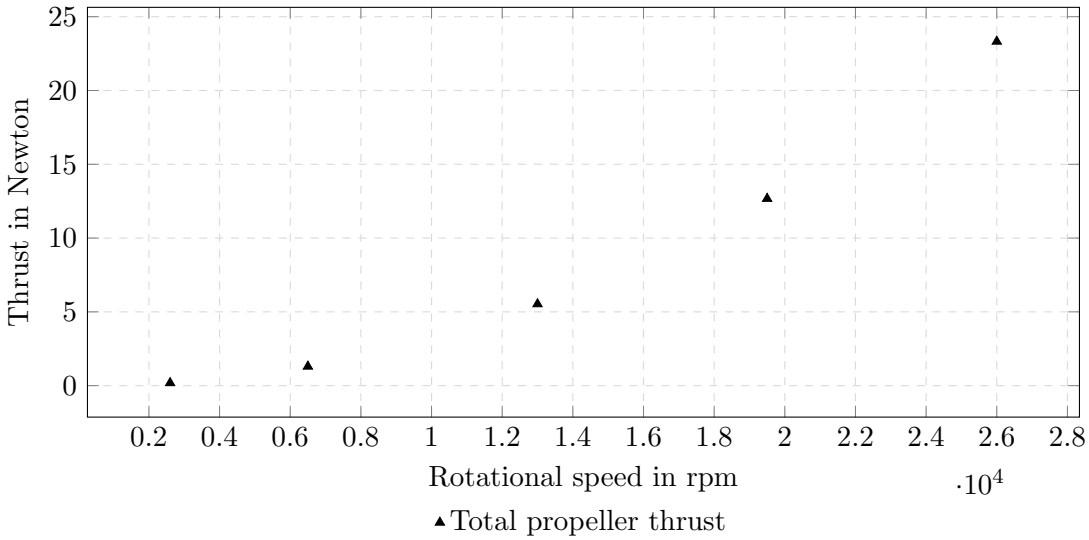

Figure 4.8: Total propeller thrust for different rotational speeds at a constant advance ratio $J = 0.77$

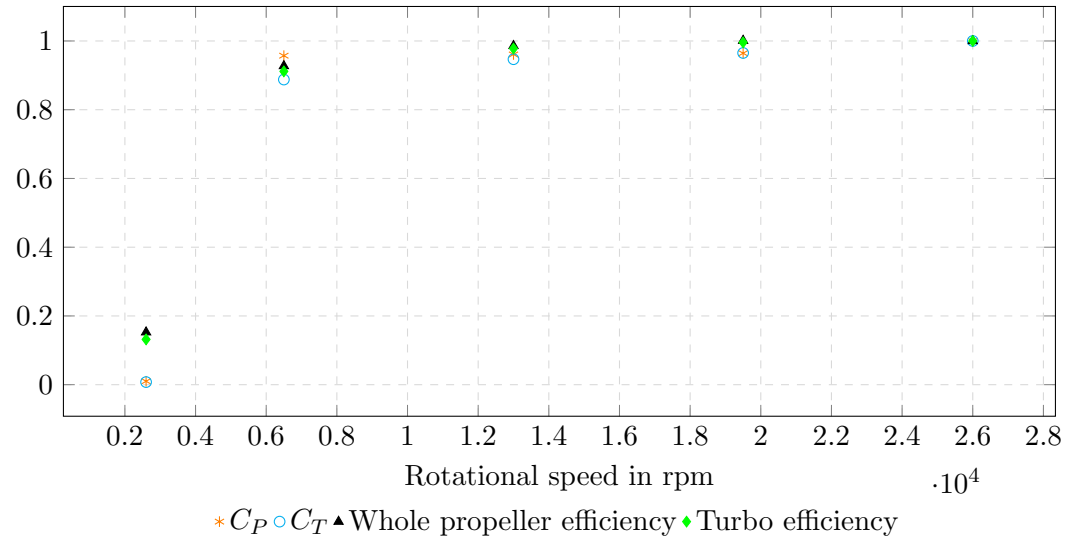

Figure 4.9: Performance parameters for different rotational speeds at a constant advance ratio $J = 0.77$

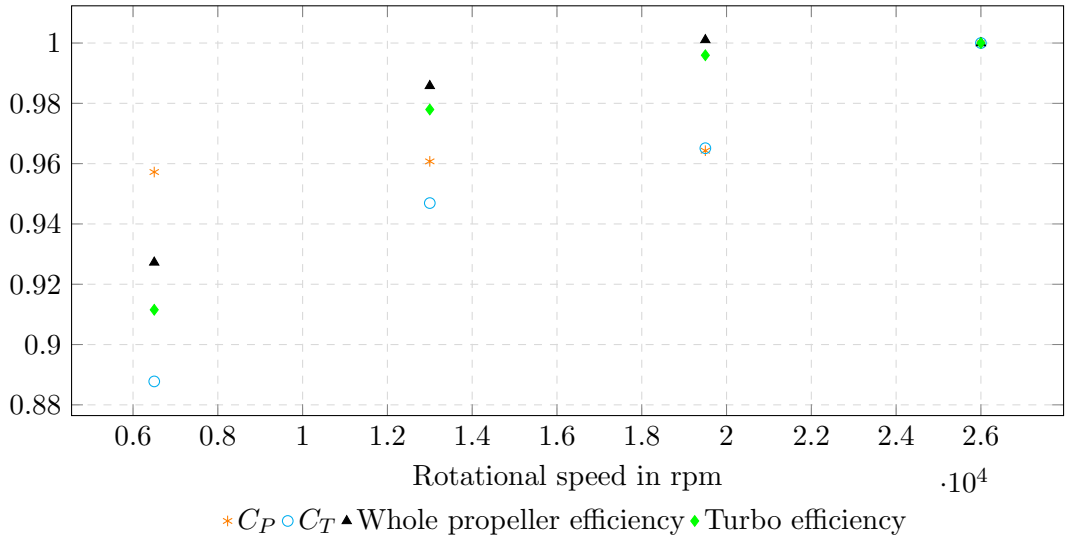

Figure 4.10: Performance parameters for the higher range of rotational speeds at a constant advance ratio $J = 0.77$

Including scatter shield

Due to problems running the simulation with the included scatter shield, there are no results available. Since the computational domain aimed to depict the real case, the scatter shield had a length of $1m$ with a radius of $0.374m$. This radius corresponds to approximately 8.3 times the blade height, which is larger than the top frozen rotor interface for the low speed domain. Also, the upper boundary was not set as frozen rotor here this time, but as a wall. This resulted in high Mach numbers at the top of the domain which for their part caused the simulation to crash. It has been tried to reduce the time scale to help the simulation converge and to change the wall boundary for the scatter shield to a free slip wall, but none of those measures succeeded.

Effect of finite nacelle geometry

Figure 4.11 shows the force acting on the blade in x-direction, with and without a finite nacelle, using the GPX313 in both cases. The first case is one with reduced wind speed and rotational speed compared to the cases presented earlier ($J = 0.77$, $n = 13000\ rpm$ and $V = 25\ ^m/_s$) and the second one uses the same operational conditions, but with the added nacelle geometry. Both cases follow the same tendency, although being slightly offset. The trailing blade for the case with included nacelle experiences a high negative thrust close to the hub. Since the total thrust for the case with nacelle added is actually higher than for the case without nacelle, more sections would need to be analysed to quantify the forces on each blade.

Table 4.2 compares the values of the main parameters for the case with and without nacelle geometry added. It can be seen that the nacelle case produces more thrust and yields better efficiency and the coefficient of power is only slightly higher than for the normal case.

Table 4.2: Comparison of main results between GPX313 without and with nacelle geometry at $n = 13000\ rpm$ and $V = 25\ ^m/_s$.

Parameter	Without nacelle	With nacelle
Total propeller thrust $[N]$	5.529	5.7710
C_P	0.2448	0.2461
C_T	0.1873	0.1954
$\eta_{prop}\,[\%]$	58.26	60.44
$\eta_{turb}\,[\%]$	70.08	73.16

Roughness and Nacelle geometry

Figure 4.12 shows the performance parameters for a nacelle case with no roughness added to the blades, normalised with the ideal CFD case, which was not depicted in

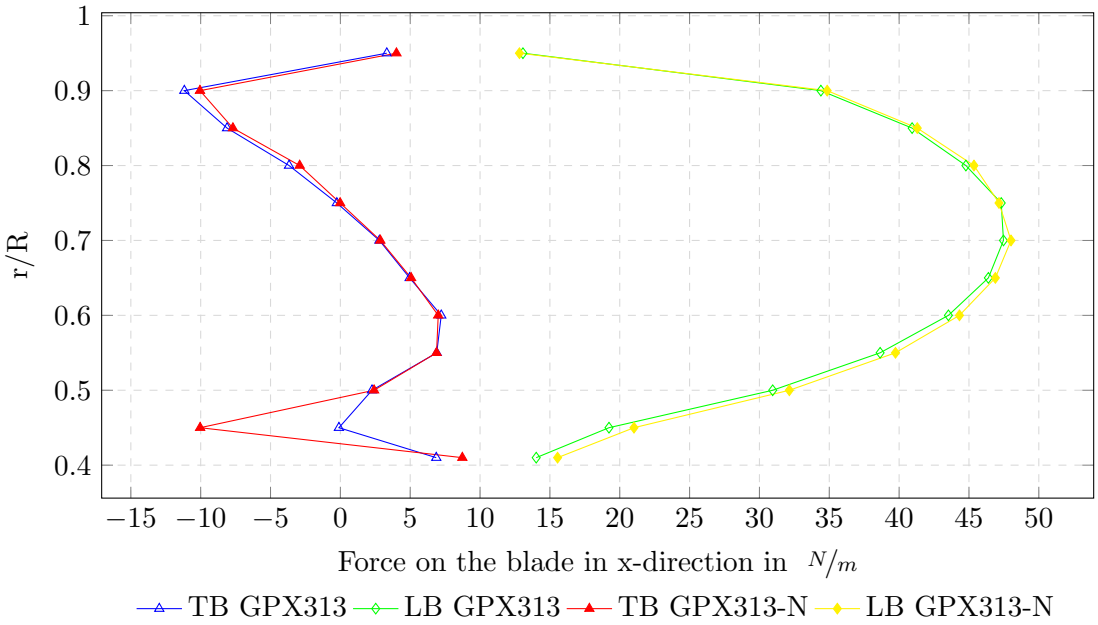

Figure 4.11: Force on the leading blade (LB) and trailing blade (TB) in x-direction for GPX313 with reduced wind and rotational speed maintaining an advance ratio of $J = 0.77$ and GPX313-N, with the geometry of the nacelle added, at the same conditions otherwise.

Section 4.1.1. It can be seen that all values, except C_P at $J = 0.6$ are higher than the ideal reference case. With increasing advance ratio, C_T increases more than C_P, also affecting the efficiencies.

Figure 4.13 shows the performance parameters for the nacelle case with rough blades, again normalised with the ideal CFD case. This time, for the $J = 0.6$ and $J = 0.77$ cases, the efficiencies are below the efficiency of the ideal CFD case, since C_P is higher than C_T, but still increasing with increasing advance ratio. This changes for $J = 0.92$ where C_T is larger then C_P and also the efficiencies are larger than for the ideal CFD case.

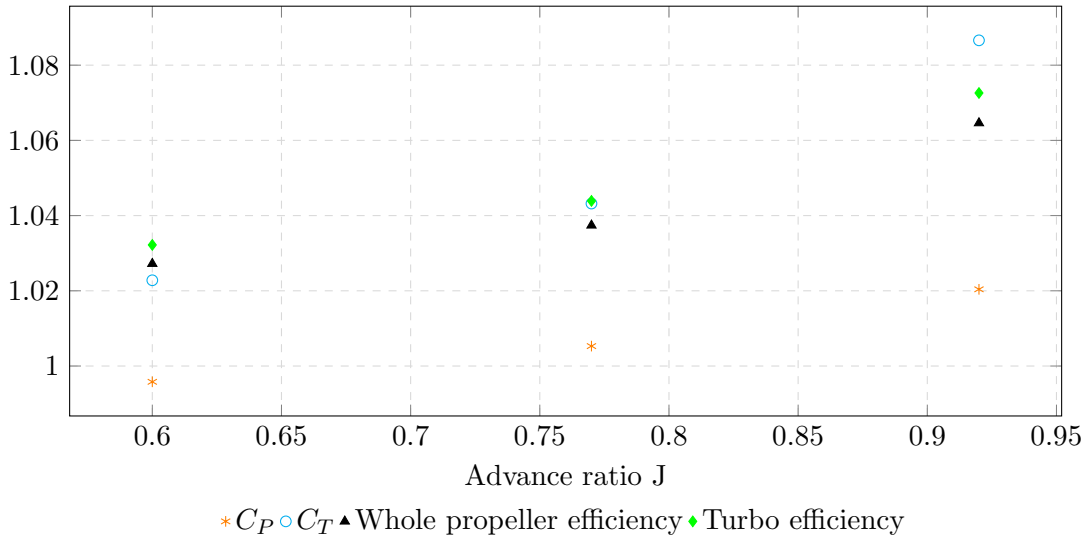

Figure 4.12: Performance parameters of the nacelle case with smooth blades normalised with the values of the case without nacelle geometry and without roughness added for varying advance ratio at 13000 rpm and 25 $^m/_s$

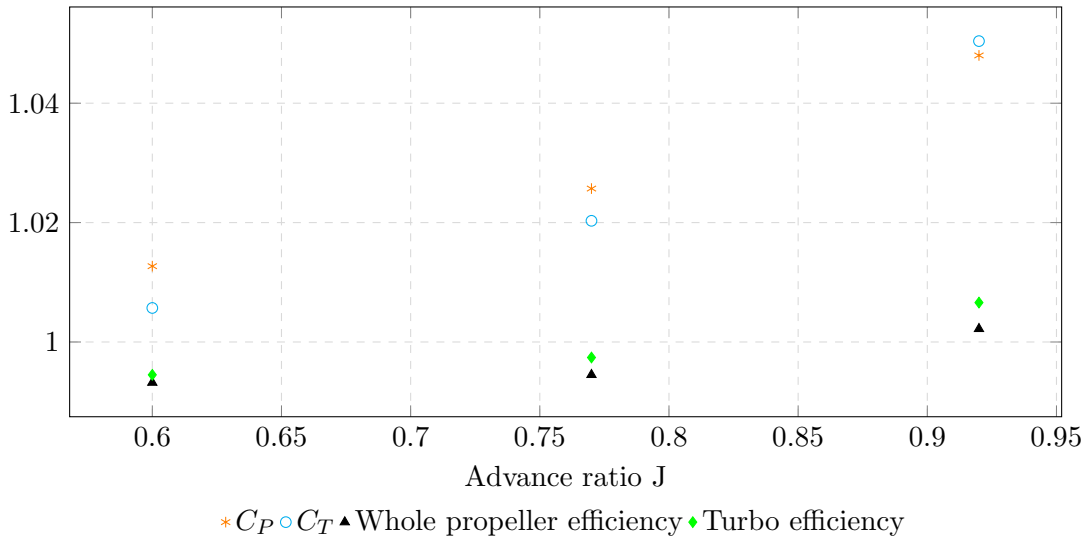

Figure 4.13: Performance parameters of the nacelle case with rough blades normalised with the values of the case without nacelle geometry and without roughness added for varying advance ratio at 13000 rpm and 25 $^m/_s$

Deformed GPX313

Figures 4.14 and 4.15 show the contours of Mach number around the blade for a normal GPX313 and a deformed GPX313,respectively, both at 13000 rpm and 25 $^m/_s$. Most affected is the trailing blade, especially at the tip. Here the Mach numbers increase

and also the turbulent boundary layer increases more compared to the undeformed case, resulting in a wider wake behind the blade. Those effects are only small for the leading blade.

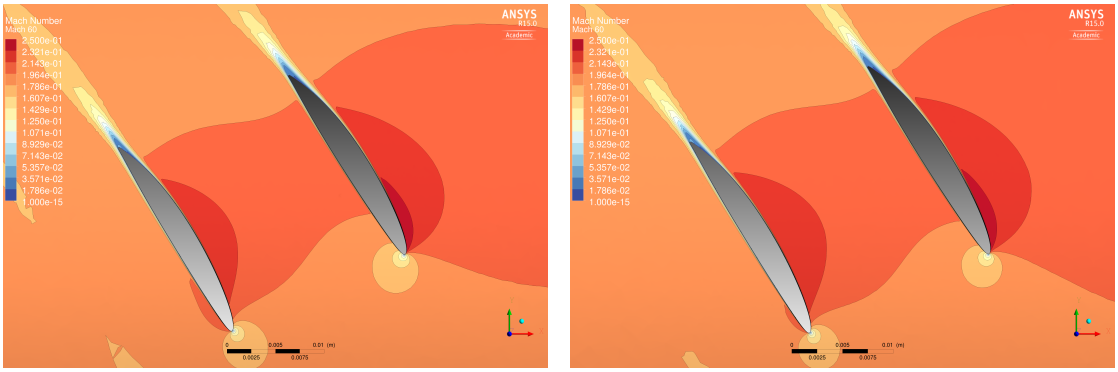

Figure 4.14: Contour of Mach number at 60% of propeller radius for the GPX313 on the left side and the deformed GPX313 on the right side at 13000 rpm and 25 $^m/_s$). The flight direction is to the right in both cases.

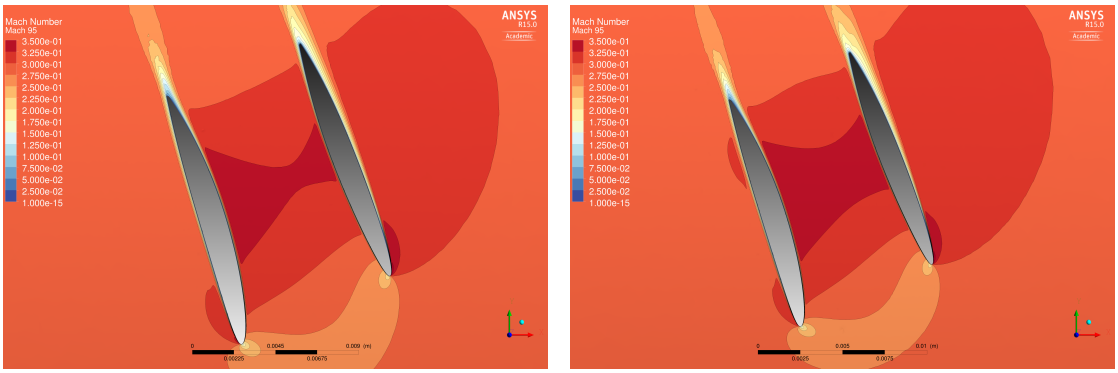

Figure 4.15: Contour of Mach number at 95% of propeller radius for the GPX313 on the left side and the deformed GPX313 on the right side at 13000 rpm and 25 $^m/_s$). The flight direction is to the right in both cases.

Figures 4.16 and 4.17 show the pressure distribution on leading and trailing blade for the normal and deformed GPX313, both at 13000 rpm and 25 $^m/_s$. Considering the leading blade, the main differences are at 60% and 80% of the radius, resulting in increased thrust for the trailing blade of the deformed propeller. At the trailing blade, the pressure difference is slightly higher at 80% of the radius for the deformed blade, otherwise both plots are quite similar.

Table 4.3 gives the values of the main parameters for the undeformed and deformed blade geometry of GPX313. It can be observed that the deformed shape yields a higher propeller thrust, C_T, C_P and turbo efficiency. The propeller efficiency is only slightly smaller for the deformed GPX313.

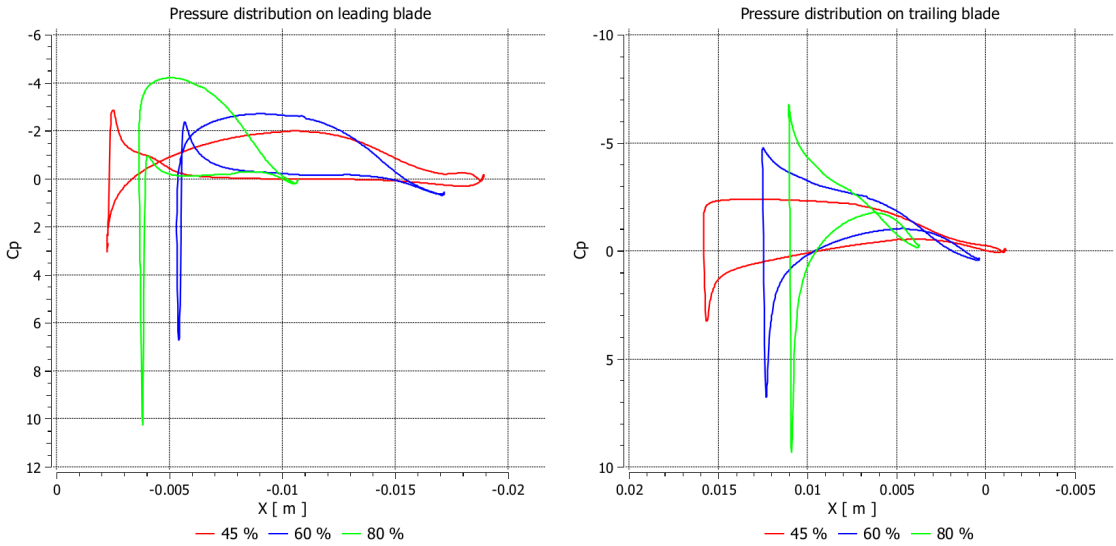

Figure 4.16: Pressure distribution on leading and trailing blade for GPX313 at 13000 rpm and 25 $^m/_s$

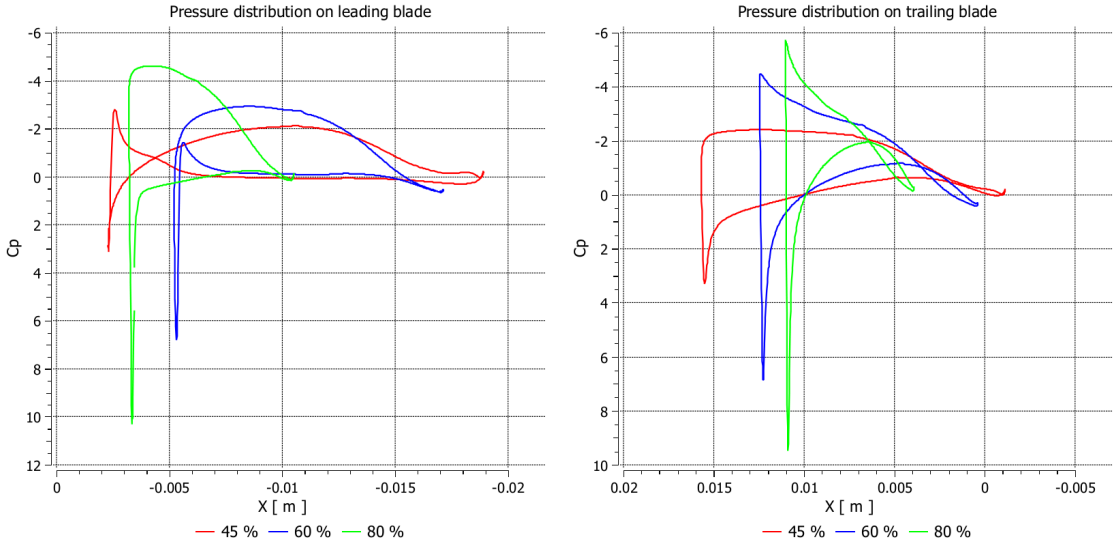

Figure 4.17: Pressure distribution on leading and trailing blade for the deformed GPX313 at 13000 rpm and 25 $^m/_s$

Figure 4.18 shows the performance parameters of the deformed GPX313 normalised with the undeformed GPX313 for varying advance ratios. All values are increasing for increasing advance ratios. Also it can be noticed, that C_P is increasing less than C_T. This results in larger efficiencies than for the undeformed case at high advance ratios

Table 4.3: Comparison of main results between the undeformed and deformed GPX313 at $n = 13000\ rpm$ and $V = 25\ ^m/_s$, $J = 0.77$.

Parameter	GPX313	Deformed GPX313
Total propeller thrust $[N]$	5.53	5.83
C_P	0.245	0.252
C_T	0.187	0.194
η_{prop} [%]	58.26	58.24
η_{turb} [%]	70.08	70.48

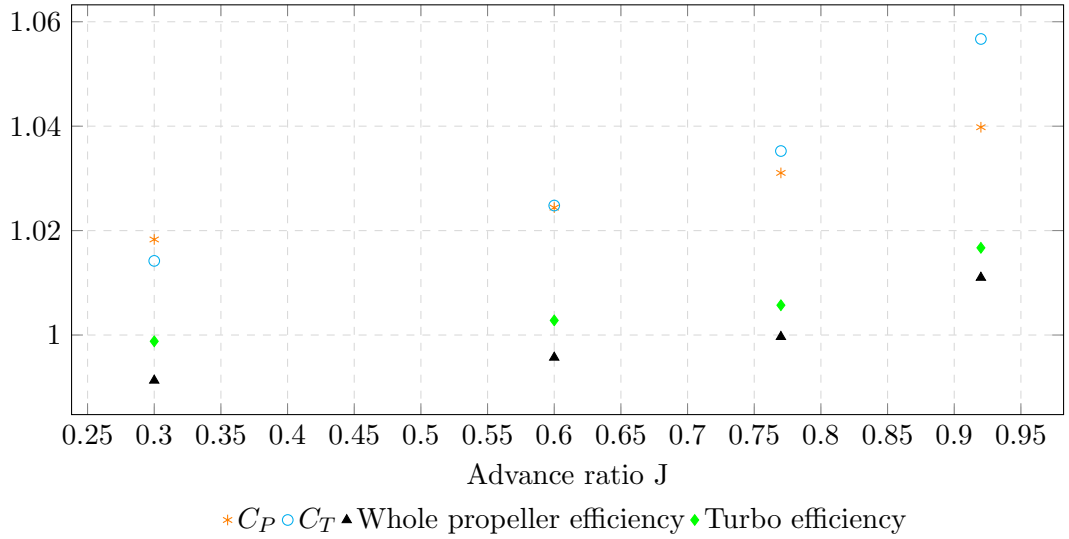

Figure 4.18: Performance parameters of the deformed GPX313 normalised with the values of the undeformed GPX313 for varying advance ratio

4.1.2 GPX316

Figure 4.19 shows the pressure distribution on leading and on trailing blade for the GPX316 at 45%, 60% and 80% percent of the total propeller radius. It can be seen that at all three radial positions thrust is generated along the leading blade, with pressure distributions that are similar to those of conventional blades. On the contrary, the trailing blade does not add to the thrust generation but, beginning at approximately mid-chord, increases the drag.

For comparison, Figure 4.20 shows the pressure distribution of the GPX313 which indicates that still the leading blade generates more thrust than the trailing blade, but still the trailing blade contributes considerably to the total thrust generation. Drag is produced only in the tip area, and more for the trailing blade.

An overview of the main results of the GPX313 and the GPX316 is given in Table 4.4

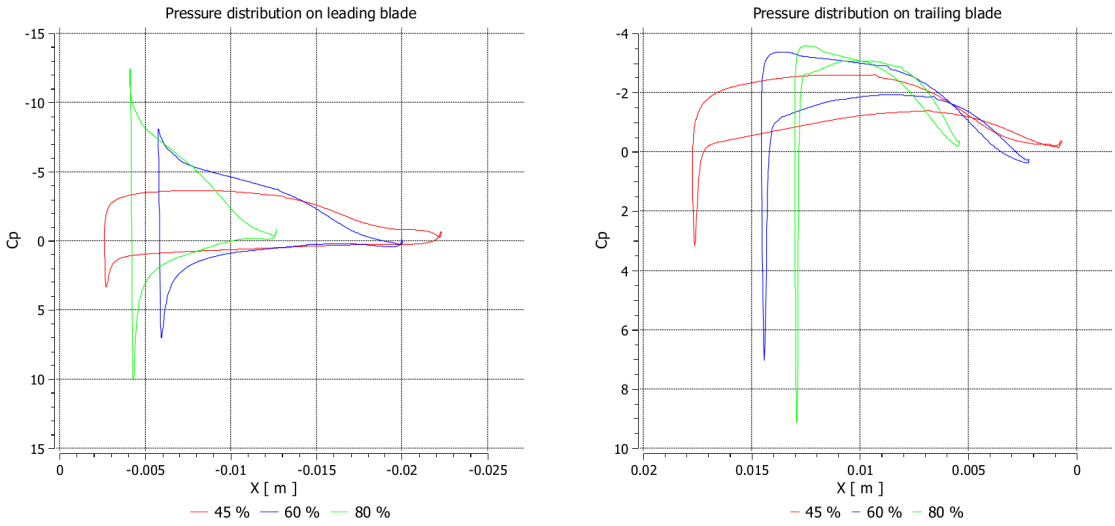

Figure 4.19: Pressure distribution on the leading and trailing bade of GPX316 at 45%, 60% and 80% percent of the total propeller radius

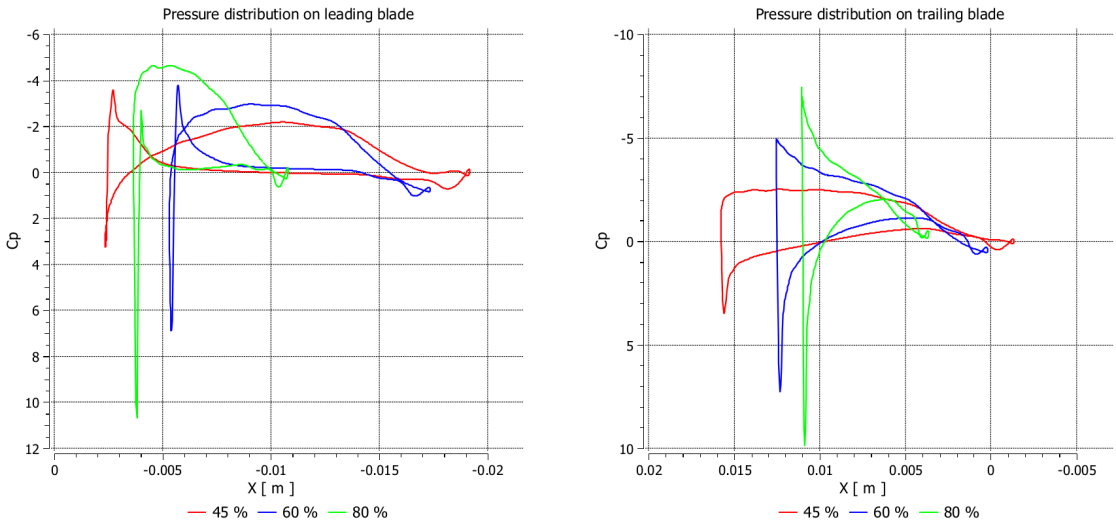

Figure 4.20: Pressure distribution on the leading and trailing bade of GPX313 at 45%, 60% and 80% percent of the total propeller radius

for comparison. As stated earlier, the GPX316 produces significantly more thrust in total even though only one blade contributes to the thrust generation. Also, the turbo efficiency is slightly higher. The propeller efficiency is however lower than that of the GPX313 due to a larger percental increase in torque than in thrust.

Table 4.4: Comparison of main results between GPX313 and GPX316 at 26000 rpm and 50 $^{m}/_{s}$

Parameter	GPX313	GPX316
Total propeller thrust $[N]$	23.32	31.47
C_P	0.255	0.371
C_T	0.198	0.274
$\eta_{prop}\,[\%]$	59.10	56.70
$\eta_{turb}\,[\%]$	71.66	72.40

4.2 FE Simulations

This section presents stresses and deformation for the GPX-313 with a diameter of $0.15m$, followed by a section GPX-313 with a diameter of $0.3m$. If nothing else is stated the results show the FE simulation using values from the material Verogray RGD850. Rotational velocities are given in rad/s. Note that each plot have different scales on color bars.

4.2.1 Stresses

Figure 4.21 illustrates the stresses due to rotational speed at 2722 and 1361 rad/s for a 0.15 m diameter GPX-313 propeller. The highest stresses can be observed on the pressure side in the central area of the leading blade and at the root of the leading edge of the trailing blade. The root of the leading edge has a very local high stress level. The stresses are at safety level of 1.04 for the 2722 rad/s and 4.2 at 1361 rad/s. Safety level is defined as $\frac{\sigma_{uts}}{\sigma}$.

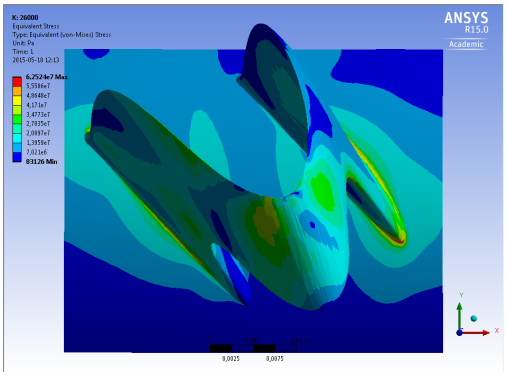

(a) Stresses seen from top View, case $2722 rad/s$

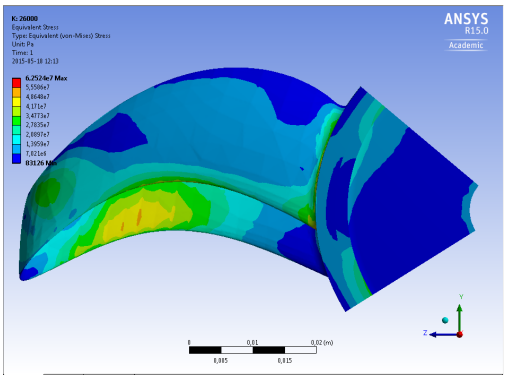

(b) Stresses seen from TE $2722 rad/s$

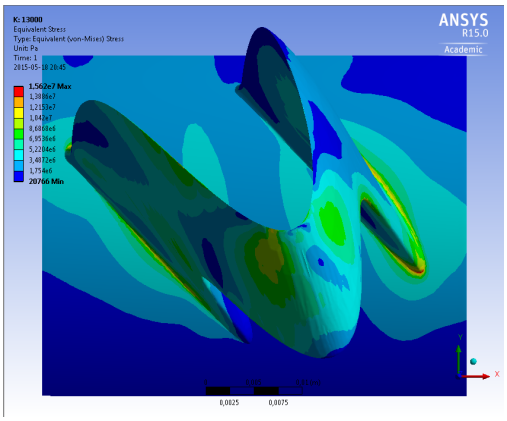

(c) Stresses seen from top View, case $1361 rad/s$

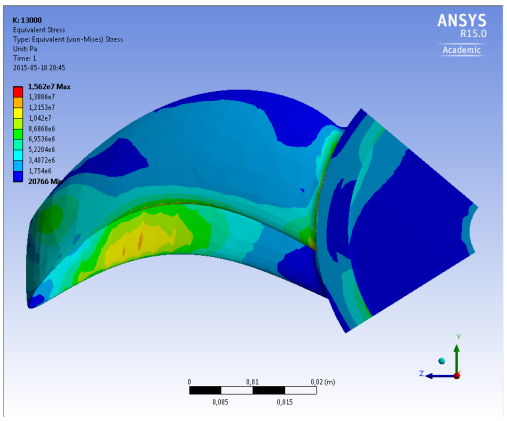

(d) Stresses seen from TE $1361 rad/s$

Figure 4.21: Propeller Stresses for GPX-313 0.15 m Diameter at 2722 and $1361 rad/s$

4.2.2 Deformation

Figure 4.22a illustrates the deformation due to rotational speed for a 0.15 m diameter GPX-313 at a rotational speed of $2722 rad/s$ and for a rotational speed of $1361 rad/s$ in Figure 4.22b.

The deformation is near four times as high for the $2722 rad/s$ case than for the $1361 rad/s$ case, which is 2 mm and 0.5 mm, respectively. The leading tip is the the area of highest deformation. There is a change in angle of attack present since the leading edge has a higher deformation than the trailing edge. This change can be seen in Table B.2 and in Figure 4.23. The yellow blade is the deformed blade and the transparent red blade is the undeformed original blade geometry.

In Figure 4.23 it can be seen that the mechanical load has lifted the blade tip and increased the total blade diameter. Most of the leading blade has been forced closer to the trailing blade with a varied change in angle of attack. Roughly the upper half of the

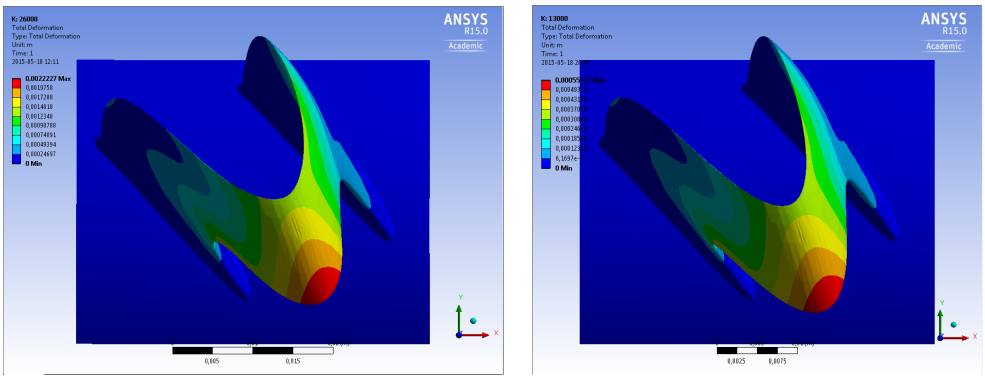

(a) Deformation seen from top view at $2722 rad/s$

(b) Deformation seen from top view at $1361 rad/s$

Figure 4.22: Propeller Deformation for GPX-313 with 0.15 m diameter at 2722 and $1361 rad/s$

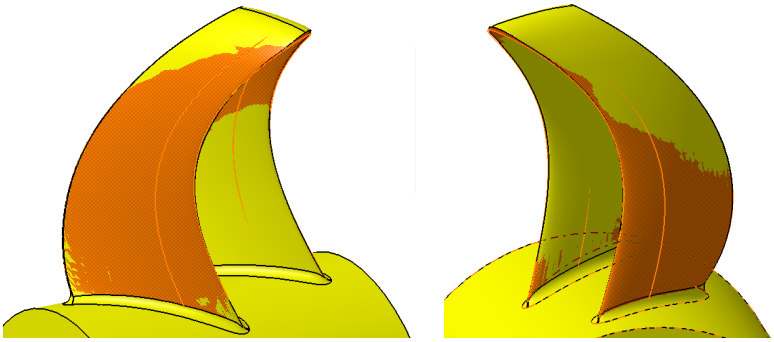

(a) View from Leading Edge

(b) View from Trailing Edge

Figure 4.23: Comparison of deformed geometry and original geometry for 1361 rad/s

trailing blade has been lifted and moved outwards from the hub. The angle of attack shows very small changes except near the tip for the trailing blade.

4.2.3 Large Propeller Simulations

Deformation and stresses from FE simulation for a 0.3 m GPX-313 at $680.5 rad/s$ is shown in Figures 4.24a, 4.24b and 4.24c. Due to the redesign of the hub the larger propeller has a slight different load case than the simulated smaller propeller. The hub is weaker which can be seen in stress concentration near the leading edge of the trailing blade.

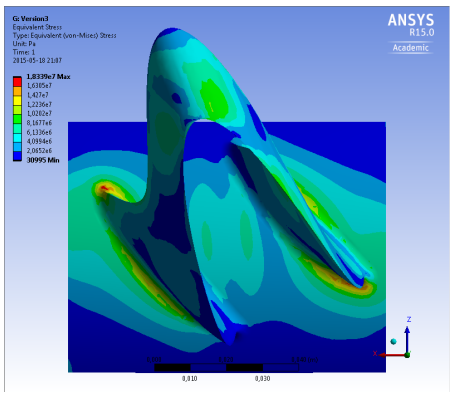

(a) Stresses seen from top, case $680.5 rad/s$

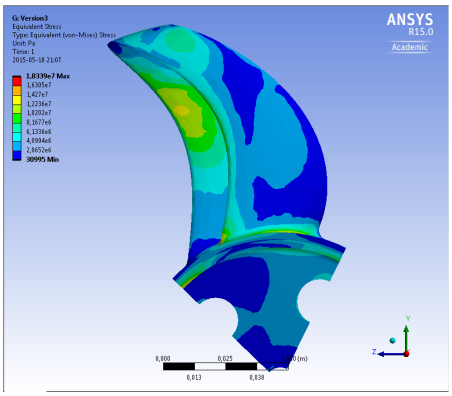

(b) Stresses seen from TE $680.5 rad/s$

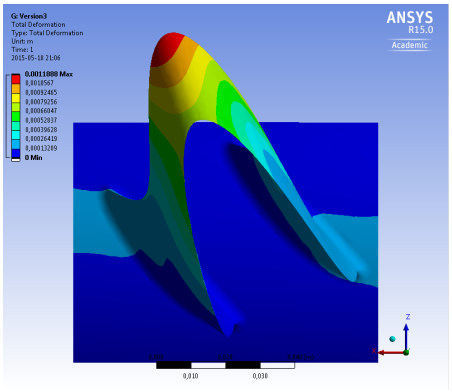

(c) Deformation in Top view, case $680.5 rad/s$

Figure 4.24: Large Propeller Simulations

4.3 Wind Tunnel Results

This section shows results from all experiments realised in the wind tunnel and is divided into one section for propeller performance and one section for the slipstream wake analysis using PIV.

4.3.1 Propeller Performance

Figures 4.26 to 4.28 show the thrust coefficient C_T, power coefficient C_P, propeller efficiency η_{prop} and turbo efficiency η_{turb} for a polished GPX-313 with a diameter of 0.15 m of RGD850 material. The results shown are measured data compensated for motor introduced torque, pressure differences of hub pressures, change in diameter due to mechanical loads and using the Glauert wind speed compensation. CFD data presented in the plots are the ideal case and one case including deformation, nacelle and blade

roughness. All CFD simulations have been realised with versions of the 0.15 m diameter model. The advance sweep was achieved by increasing the ambient speed in the test section, the rotation velocity is targeted for a constant rotational speed but did variate with ±500 RPM depending on load and propeller size.

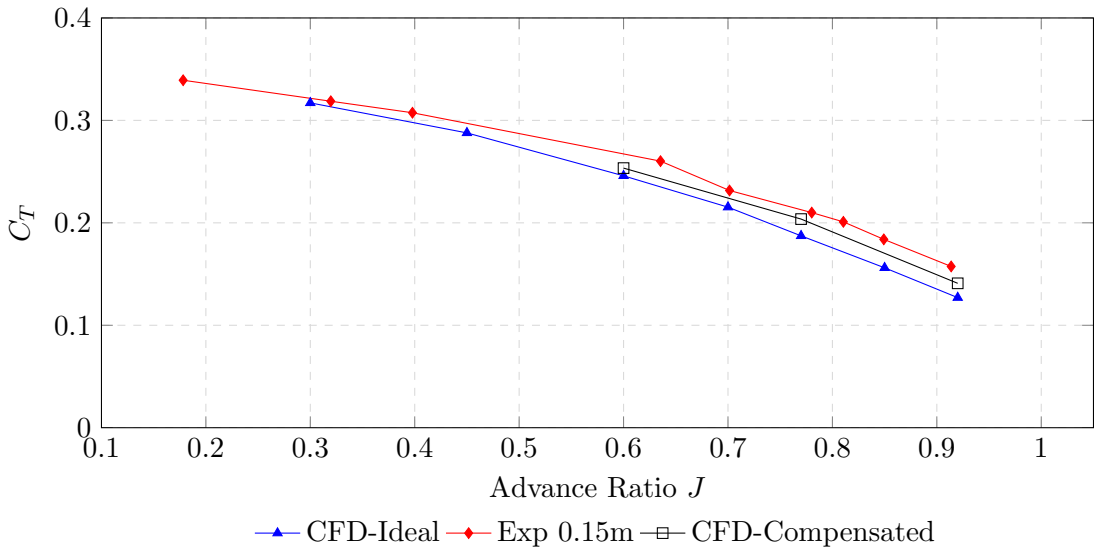

Figure 4.25: Wind tunnel Results

In Figure 4.25 the thrust coefficient is shown obtained from CFD simulations and experimental data relative to advance ratio. The thrust coefficient from the ideal case and the experimental data are following the same trends but the experimental results tends to show higher values with increased advance ratio. The compensated CFD case decreases the deviation between simulated and experimental data by an average of 46%. In the experimental data a deviation from the otherwise smooth curve at $J = 0.7$ can be seen.

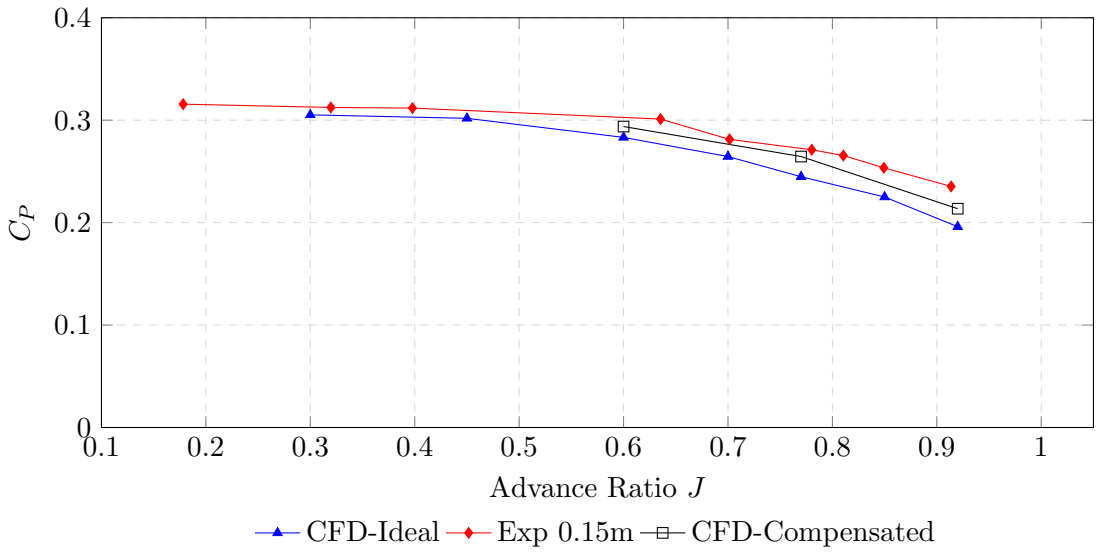

Figure 4.26: Wind Tunnel Results C_P

Figure 4.26 shows that the trends of the power coefficient for the ideal CFD case and experimental data are similar but with an increased deviation at higher advance ratios where the experimental data shows higher values than numerical results. The compensated CFD case shows better correlation with experimental data. In the experimental data a deviation from the otherwise smooth curve at $J = 0.7$ can be seen. It can be observed that the power coefficient for experimental data is near horizontal up to $J = 0.6$ and afterwards decreasing.

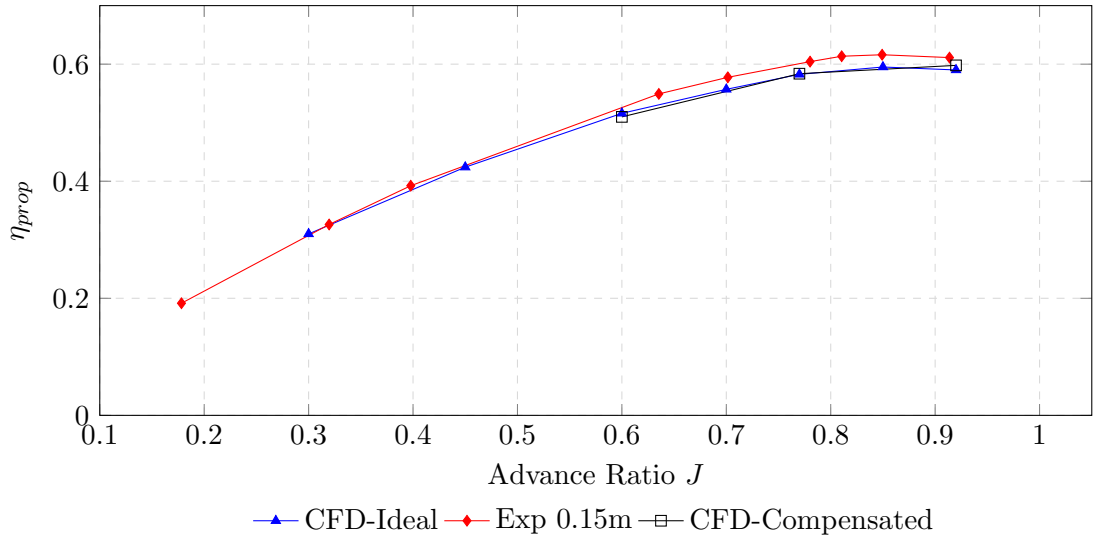

Figure 4.27: Wind Tunnel Results η_{prop}

Figure 4.27 shows the propeller efficiency for the ideal and compensated CFD case and experimental data for the polished 0.15 m GPX-313. The propeller efficiency for the ideal and compensated CFD case are very similar, the experimental data shows higher values in the propeller efficiency.

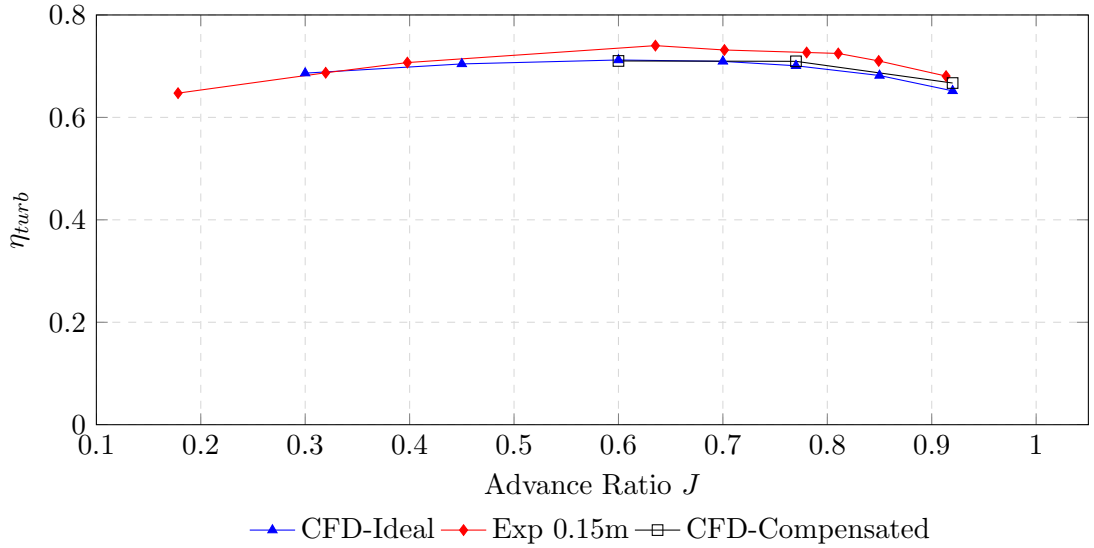

Figure 4.28: Wind Tunnel Results η_{turb}

Figure 4.28 shows the turbo efficiency for the ideal and compensated CFD case and experimental data for the polished 0.15 m GPX-313. The propeller efficiency for the ideal and compensated CFD case are very similar, the experimental data shows higher values than numerical results for propeller efficiency.

4.3.2 GPX-316

The results for a GPX-316 have been normalized to the values of GPX-313 to illustrate the difference in performance of this propeller. In Figure 4.29 a comparison of the dimensionless numbers C_T, C_P, η_{prop} and η_{turb}can be seen.

It can be seen that the GPX-316 tested had a higher drag over the whole range than the GPX-313, it can also be seen that the thrust produced is increased between $J = 0.55 - 0.8$ with a peak of 5.8 %. CFD simulations show a higher increase in drag and thrust as well as a higher ratio between C_T and C_P than measured in experiments.

4.3.3 Polished Non-Polished

Results from testing a unpolished GPX-313 have been normalized to a polished GPX-313 in Figure 4.30, the dimensionless numbers C_T, C_P, η_{prop} and η_{turb} are displayed.

Below $J = 0.6$ the difference between polished and non-polished blade is visible, above this advance ratio the amplitude of benefits of polishing becomes more unclear.

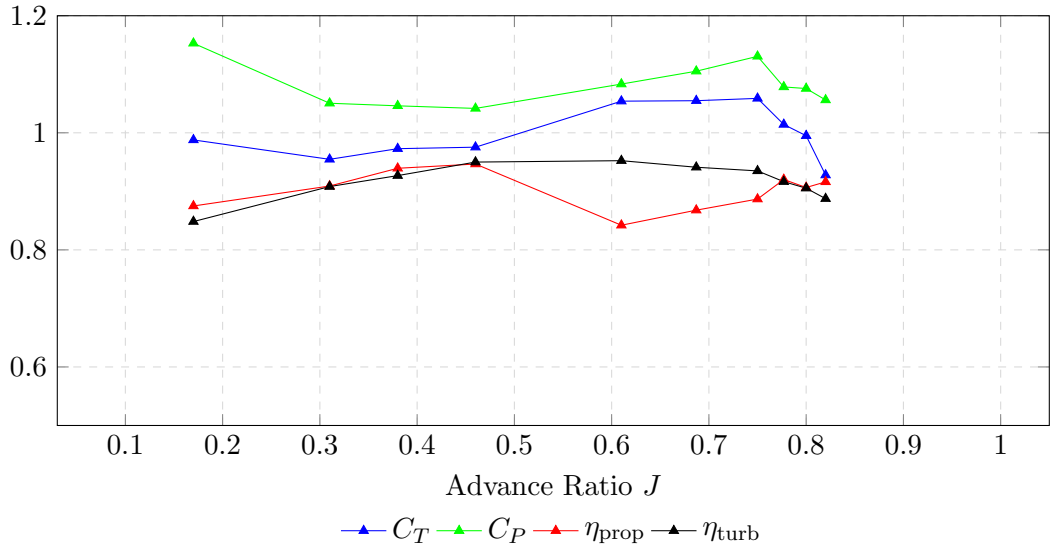

Figure 4.29: GPX-316 normalized to the GPX-313 in RGD525

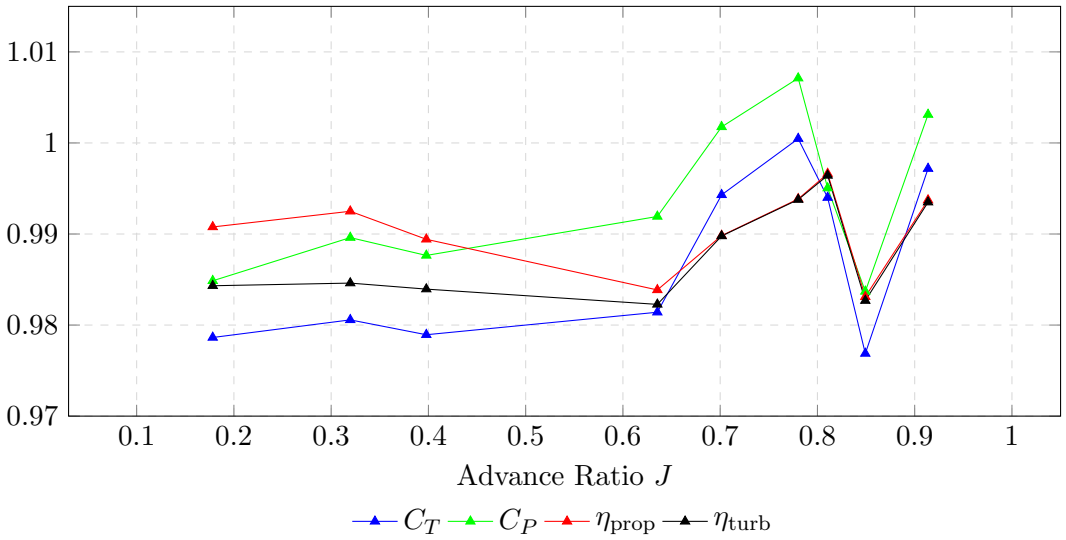

Figure 4.30: Values of non-polished GPX-313 compared with the polished GPX-313 propeller

4.3.4 0.3 m diameter compared with 0.15 m diameter GPX-313

In Figure 4.31 the efficiencies for the larger propeller are lower than for the smaller one at all advance ratios.

In Figure 4.32 the thrust and power coefficient are shown for the large and smaller polished propeller. The power coefficients are very similar between the two cases.

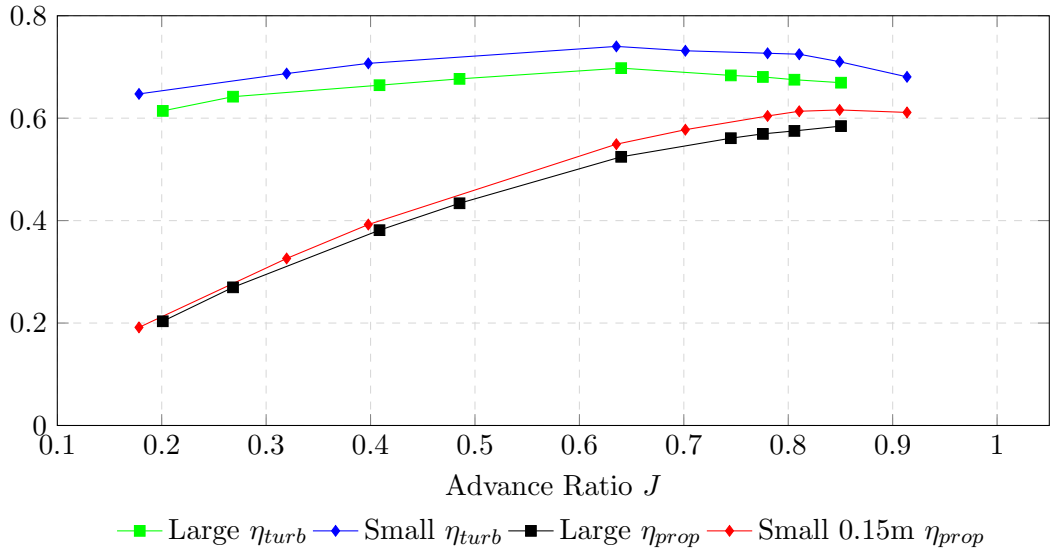

Figure 4.31: Comparison of 0.3 m and 0.15 m GPX-313

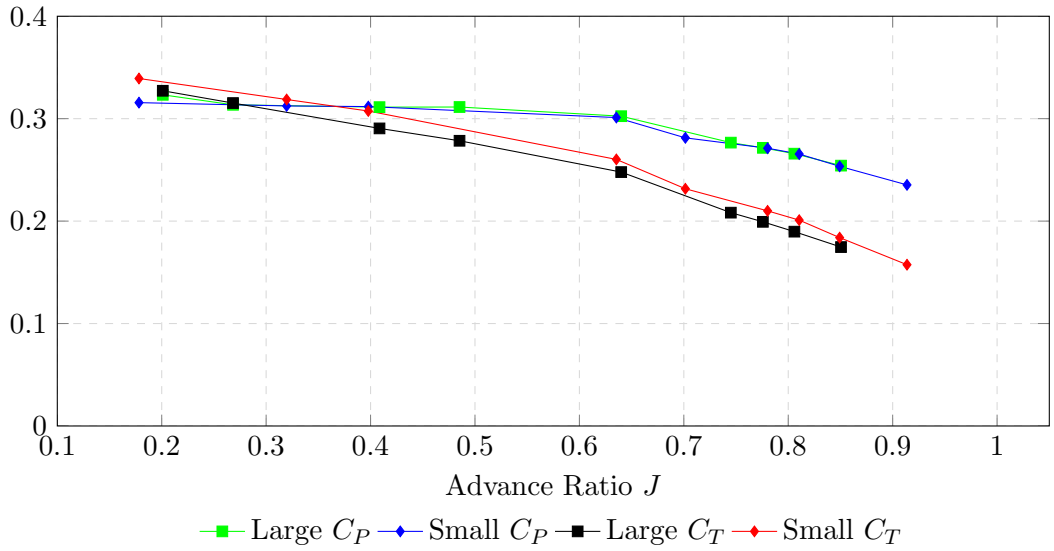

Figure 4.32: Comparison of 0.3m and 0.15m GPX-313

4.3.5 PIV Results

Figures 4.33 to 4.36 show a 24x24bit PIV analysis of the flow field behind the propellers GPX-313 and GPS-101 near 13106 RPM and ambient wind speed in the wind tunnel of $24.5-24.7m/s$. The camera is set up so that the upper left corner of the picture is taken below the trailing hub just behind the propeller. There is a particle on the lens during the tests that can be seen as disturbance near the horizontal center two thirds from the

bottom of the picture. The GPX-313 and the GPS-101 spin in opposite directions and therefore the V_y values and the color scales are inverted between the two cases.

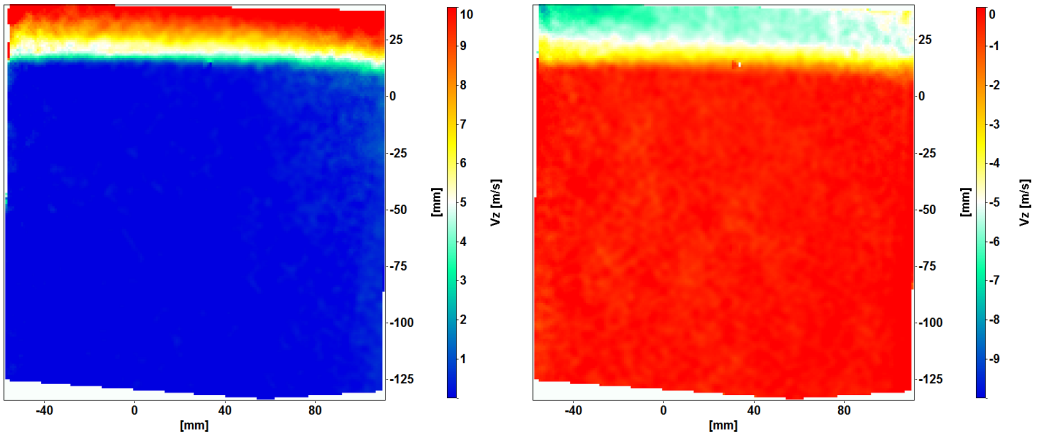

(a) GPX-313 V_y averaged with 100 Samples **(b)** GPS-101 V_y averaged with 100 Samples

Figure 4.33: Comparison in swirl velocities between GPX-313 and GPS-101

In Figures 4.33b and 4.33a it can be seen that the average rotational velocity in the slipstream is higher for the GPX-313 than for the GPS-101. Highest average rotational velocities are $10m/s$ for the GPX-313 and $7m/s$ for the GPS-101 running under the same conditions.

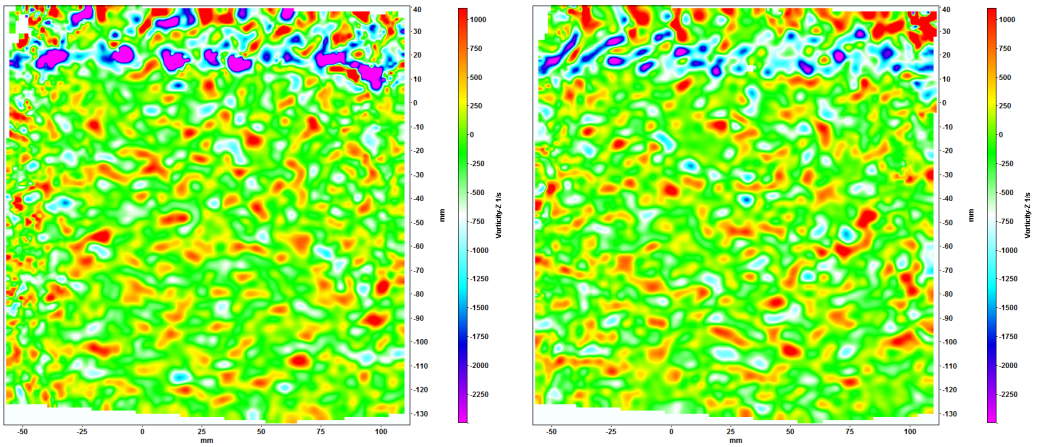

(a) ω_y GPX-313 **(b)** ω_y GPS-101

Figure 4.34: Vorticity ω_y

In Figures 4.34a and 4.34 the instantaneous swirl in the xz plane is illustrated. The two frames from the two propellers are not synchronised to the same position of the two blades. In Figure 4.34a it can be seen that the vortices at tip radius in the slipstream of the GPX-313 do not have a circular shape but are rather kidney shaped. The same

phenomena for GPS-101 is illustrated in Figure 4.34b where the tip vortices are closer to circular.

Figures 4.35 and 4.36 show a comparison between CFD data and PIV data, the image from PIV data have been rotated and scaled to make it easy to see the difference between the CFD and PIV data.

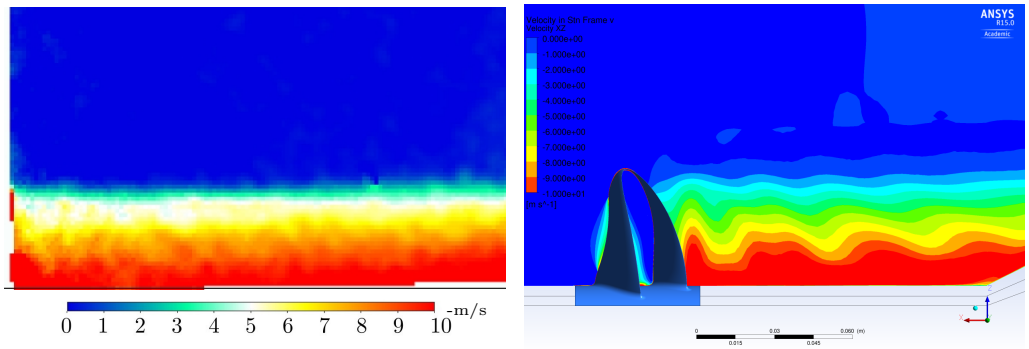

(a) GPX-313 V_y averaged with 100 Samples **(b)** GPX-313 V_y from CFD with Nacelle

Figure 4.35: V_y velocity comparison of CFD and PIV results

Figure 4.35a shows the velocities in y direction from PIV data and CFD in the vertical plane. The velocity scale are of the same range but with different color scales. In Figure 4.35 the rotational velocities behind the physical propeller can be seen to be very similar to simulated data.

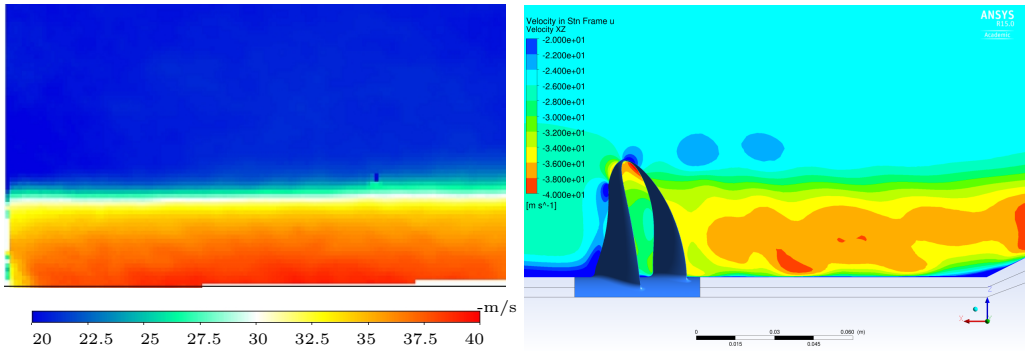

(a) GPX-313 V_x averaged with 100 Samples **(b)** GPX-313 V_x from CFD with Nacelle

Figure 4.36: V_x velocity comparison of CFD and PIV results

In Figure 4.36 it can be seen that the flow field behind the physical and simulated blade are very similar. The flow field outside the slipstream differs with approximately $5m/s$ between the CFD simulations and the PIV results, likely due to that the PIV plane are just downstream the leading support pylon and in that wake the flow field velocity is reduced. In appendix instantaneous data for both GPX-313 and GPS-101 can be found in Figures D.1 to D.4.

5

Discussion

5.1 CFD

5.1.1 Surface roughness

In Chapter 4.1.1 it was shown that the roughness has an important effect on aerodynamic propeller performance. The studies that were conducted in low and high speed conditions yielded a decrease in thrust and efficiencies for increasing roughness. This decrease was less intense for the low speed cases than for the high speed cases, which shows the dependence between flow velocity and roughness heights.

The results for the cases with an added equivalent sand roughness of $k_{s,eq} = 5\mu m$ may be questionable, as the mean y^+ value was still smaller than 2 and according to [11], a Low-Reynolds number model can not be used to include roughness effects.

In general, the added roughness caused an increase in trailing blade thrust, but a decrease in leading blade thrust. Since the thrust decrease on the leading blade was more important, the whole propeller thrust decreased as well, about 10% for the high speed case and 4% for the low speed case. The decrease in thrust was followed by an increase in drag and torque. Since the coefficients of power and of thrust are directly connected to the torque and thrust values, respectively, C_P increased slightly whereas C_T decreased accordingly.

The decrease in efficiencies is quite important for increased roughness, since the loss for the high speed case is about 15% compared to the reference case and about 7% for the low speed case with the total propeller efficiency loosing less points than the turbo efficiency.

Figures 4.4 and 4.5 show the difference between the smooth and a rough case. It can be seen that the flow is attached for the smooth and the rough case. However, the turbulent boundary layer thickness increases for a case with added roughness, leading to the formation of a broader wake behind the blade. This can be observed for both the leading and the trailing blade. The leading blade produces in the smooth case more

thrust than the trailing blade, leading to an unbalanced loading of both blades. This can be seen is due to interference from the flow field of the leading blade with the trailing blade. With roughness added to the blades, the leading blade looses performance, from which the trailing blades benefits, as there is a slight increase in thrust.

Figure 4.6 shows a comparison of the force acting on the blade in x-direction with varying blade height for the smooth and a rough case. As before, the differences in trailing blade performance are quite small, with the rough case performing slightly better at the upper blade half. The leading blade in contrast looses a lot of thrust with roughness added, which then sums up to a decrease in total thrust. Also, the leading blade performance is evenly affected over the whole height of the blade.

Unfortunately, a precise correlation between the values of the measured roughness to the equivalent sand roughness could not be presented, and only a possible range could be identified. It can also be noted that adding roughness to cases with a low inlet velocity results in a longer time needed to solve those cases. Nevertheless, it was shown that small roughness effects may have a large influence on the aerodynamic performance of a Boxprop.

5.1.2 Near wall mesh resolution study

The aim here was to estimate the influence wall functions could have on the accuracy compared to the original mesh that used the Low-Reynolds number model, in particular with regard to the automatic wall functions used in the roughness studies. It could be shown in Figure 4.7 that the deviation from the reference values was rather small for the first cases and in all cases less than 1%. The deviation from the reference case was more important for Case4 and especially Case5, which reached a mean y^+ value of around 20. Also to be noticed is that the thrust on the respective blades, coefficients and efficiencies are acting contrary to the ones yielded from the roughness studies. Therefore it seems reasonable to assume that the use of the automatic wall functions did not ameliorate the results from the roughness studies, but rather worked against them.

Further on by using the wall functions it could be shown that the number of elements could be decreased by up to 10 million almost without noticeable change in the general performance parameters. Therefore, if only they are sought for or for initial simulations it is worth considering using rather wall functions and save computational costs.

5.1.3 Bulk flow mesh resolution study

By maintaining the inflation layer as it was given for the reference case and changing the mesh sizing, a reduction of about ten million elements could be achieved. It is also noteworthy that there was no noticeable difference in thrust, drag, C_T or C_P. It could be shown, that a decrease of about ten million elements would still yield consistent results. The difference between the performance parameters for each set-up was less than $\pm 1\%$. In combination with a change in inflation layer, as described in 5.1.2, a even larger decrease in elements would be possible, making meshing and solving the cases much faster. This would be recommended for initial simulations or for faster meshing

processes, since a working mesh and small inflation layer can likely be refined later on. This would make those simulations computationally quite inexpensive, yet sufficiently accurate at the same time for general propeller performance.

A decrease in mesh size was not considered for the realised studies, since the studies that used this domain were mostly completed by the time the mesh study was finished.

5.1.4 Variation in rotational speed and wind speed

The plots presented in Chapter 4.1.1 justify the choice of a rotational speed of $13000rpm$ in the experimental tests. In Figure 4.8, the thrust has dropped to roughly one fourth compared to the reference case with $26000rpm$. Since this matches the conditions in the wind tunnel quite good, the case with $13000rpm$ and $25^m/_s$ has been taken as a reference for experimental tests as well.

The efficiency depicted in 4.9 does not change that much in the area of high rotational speed. It only decreases significantly from its reference value when a rotational speed between 6500 and $2600rpm$ is reached. The decrease in propeller efficiency is less than 2% and the decrease in turbo efficiency less than 3% for $13000rpm$. Thus running the experiments with a lower rotational speed is still sufficient and gives acceptable data considering the original design point of the propeller. However, common wind and rotational speed is desired if CFD and experimental data should be compared.

The simulation results shown in Figures 4.25 to 4.28 agree with the general tendency of the experimental data. The C_T values are fairly well captured, whereas the simulated results for C_P are approximately 5% lower than the experimental values. The efficiencies on the other hand are slightly higher in the simulations than in the experimental tests, with less deviation for η_{prop} at low advance ratio and more constant deviation for η_{turb}.

The cases with the varying advance ratio were simulated using a smooth blade and hub surface, since the actual roughness of the blades was unknown at this point of time, with no measurements available. It may still be plausible that a deviation of about 10% from the smooth case exists, considering a higher roughness and a wind speed of $25^m/_s$ and a rotational speed of $13000rpm$.

5.1.5 Including scatter shield

No results were available due to problems with the computational domain as described earlier. Nevertheless, since the experimental tests have been run predominantly in the wind tunnel, the importance of verifying the influence of the scatter shield diminished.

5.1.6 Effect of finite nacelle geometry

The aim was to estimate how much influence the nacelle has on a Boxprop with $0.15m$ diameter. As expected, the geometry of the nacelle causes a slower velocity field right in front of the propeller. Figure 4.11 shows that this influences the leading blade at 45% of the propeller radius directly which produces less thrust at this point. Otherwise, the values of the case with the cylindrical hub and the case with the finite nacelle geometry

do not vary largely, but the case with added nacelle produces more thrust and has slightly higher efficiencies. This is due to the decreased velocity directly in front of the propeller.

Compared to the normal case, the case with added nacelle produced about 4% more in thrust (and thus C_T) whereas the propeller torque did not change more than 0.5%. The efficiencies were also in the range of 4% higher and the drag force increased about 13%.

The computational domain was adapted to fit the geometry of the nacelle and was built from scratch. Although it shows consistent results for all cases that were realised, a mesh and domain study would be advisable for further verification of this domain.

5.1.7 Roughness and nacelle

This study was realised at the end of the project, when roughness measurements were available. This can just show a first trend how the performance parameters vary.

The nacelle geometry with smooth blade surfaces gave an increase in all performance parameters as could be seen from Figure 4.12. When a surface roughness of $21\mu m$ was added to the blade, as shown in Figure 4.13, the performance parameters still show the same trend, but did not increase as much as for the case with smooth blades. In fact, the efficiencies only became larger as the case with the smooth blades for the highest advance ratio simulated and the thrust increase was much slower.

It can be noted that the combination of blade roughness and low inlet velocities resulted in a much longer time to solve those cases. It was also planned to include cases at lower advance ratios, which did not converge correctly in the time given.

5.1.8 Deformed GPX313

The slight increase in thrust for the deformed propeller that was presented in Section 4.1.1 is assumed to be mainly due to the larger diameter and the increased cone angle. The variation of the angle of attack on the leading edge due to twist will also have an influence, which would need to be checked on multiple blade sections. The increase in performance parameters C_P and C_T is about 3% for $J = 0.77$ and $13000rpm$ but will be more important at higher rotational speeds as the deformation is four times larger at $26000rpm$. Since this case was realised at the end of the project, gathering a general understanding of the effects seemed to be adequate and no further studies were envisaged.

5.1.9 GPX316

From the plots giving the pressure distribution it can be seen that the GPX316 produces most of its thrust on the leading blade, with a pressure distribution comparable to that of a conventional blade.

5.2 Approximated Uncertainties

Input values that have been sampled and averaged by equipment provided by existing wind tunnel equipment such as wind speed or temperature in the wind tunnel have been approximated with a uncertainty of 0.5% of measured interval which is twice as high as many of the instruments specify. All compensations used at experimental data, as pressure difference at the hub, motor ventilation and Glauert compensation, have been considered as an uncertainty in terms of constant bias offset.

5.2.1 Motor Ventilation

The motor ventilation cooling outlet is upstream of a 0.15m diameter propeller mounted in pusher configuration. The mass flow or swirl of the cooling is varied by RPM and has not been included in the CFD nor in any experimental measurement. This mass flow will interact with the downstream propeller but to which degree is unclear. The motor cooling introduces torque which is shown in Figure C.2 have been used by subtracting the measured torque with the cooling introduce torque. This cooling flow is likely to introduces a swirl to the flow upstream the propeller which would decrease the blade loading, thrust and torque. The compensation used might therefore be over estimating the effect of the cooling flow on torque. The change of the upstream flow field or increased mass flow due to motor cooling have not been documented and therefore not compensated for, losses due to the introduced torque due to cooling have been used which have overall been very small, less than 2% of total torque.

5.2.2 Aft Nacelle

The distance for the aft nacelle has shown to have a large effect during experiments. The aft hub distance has been iterated where a decreased distance from 1cm to 1mm had a large impact on the thrust measured. The leading hub distance was never adjusted even though parts was manufactured to adjust for this. To quantify the effect pressure measurements at the leading and trailing side of the hub were done. These values were then used as if the pressure field was constant on the whole area of the hub. The pressures are shown in Figure C.3.

5.2.3 Blade Deformation

The accuracy of the blade deformation was assumed to have an error of ± 30 %. This was due to a number of assumptions in mechanical properties. Simulations were done with a simplified linear model of the material, conversion from deformed mesh to smooth geometry includes errors and creep in the tested propellers. The error of $\pm 30\%$ was chosen since this would be much larger than estimated errors in modern FE calculations on deformation. A method to validate deformation simulations is presented in future work.

5.2.4 Surface Roughness

The effect of polishing the blades can be observed in Figure 4.30. In the advance ratio range below 0.6 the difference for CT and Cp between a non-polished and polished blade is in the range 1-2%. Above $J = 0.65$ there is a large uncertainty of the results, a part of the errors can be uncertainties in the measurements. No compensations factors were used in comparison between the cases. Since there is no surface measurements after the polishing it is hard to tell if the correlation to CFD accurate. It can be said that there is a noticeable difference in structure between polished and non-polished. This can be seen in figure 3.15a and 3.15b, comparing the surface of the non-polished and the polished blade.

5.2.5 Irregularity in Leading Nacelle

The effects from the leading Nacelle have been captured with CFD simulations but the nacelle in the experiential rig has defects that were not included in the CFD case. These can have a substantial effect on boundary growth upstream the propeller.

5.2.6 Load Cell Torque Verification

The torque measurement precision of the MBA500 has not been controlled in-house and the calibration protocol from supplier is trusted to be accurate. The accuracy given by the supplier and the standard deviation have been used to evaluate the performance but since no verification has been done and as the load cell has been used in previous thesis the accuracy can be questioned.

5.2.7 Pylon Interference

The front pylon creates disturbance downstream that have impact on the propeller performance. PIV data was taken downstream a pylon in the plane where the impact should be largest. In Figure 4.36 a $5m/s$ lower ambient wind speed can be seen in the PIV results than in the CFD results.

5.2.8 PIV Accuracy

There is a decreased accuracy in the upper corner of the PIV measurements. In the upper right corner, which has the most disturbance, this would results in a speed error of about 4% at 40 m/s, but in the bigger part of flow field the error would be around 2% at peak velocities. Since the data has mostly been used to compare flow field characteristics the exact accuracy of the speed has not been of great concern and is therefore not mentioned in the report.

6

Conclusion

This master thesis work is part of an ongoing project and it has contributed to remove a number of the uncertainties arising in earlier theses.

It can be concluded that it is difficult to compare experimental test results gathered from a static test rig to steady state simulations. To further increase the correlation between CFD and experimental data, the rig has, on one hand, been placed in the wind tunnel, and, on the other hand, the CFD simulations have been modified by applying roughness and geometric effects. This resulted in good correlations between testing and simulation data concerning overall trends. The documented compensation factors, such as roughness effects, deformation, and effects from the nacelle geometry yielded an improved coherence between the data.

The surface roughness on the propellers could be obtained at the end of the thesis. Using the correlation of Flack and Schultz, this helped to get an idea of what range the actual surface might be in, for the real geometry as well as for the simulated case. Uncertainties remain regarding the exact correlation and the effect of the roughness on the different blade sides, which may be different on the pressure side and on the suction side.

The effect of polishing the blades was tested experimentally and the polished propeller showed general trends of increased performance. However, the improvement was less than expected assuming the change from the actual measured surface roughness to an almost smooth surface. The change in surface roughness on the polished blades was never measured so it can only be concluded that polishing can improve the performance; to what degree, however, remains unclear.

We can conclude that this set-up should not be run at 26000 *rpm* as in previous theses due to high loads and deformation in propeller blades and vibration. A rotational speed of 13000 *rpm* has been proven to work in terms of vibrations, and FE simulations have shown that mechanical loads are below critical values. Using CFD, it could be verified with a number of simulations maintaining a specified advance ratio of $J = 0.77$

that a rotational speed of 13000 rpm is sufficient to get accurate and comparable data using a wind speed of 25 $^m/_s$ as the rotational speed was lowered after the early static tests.

The additional domain including the nacelle geometry helped to understand the effects of the nacelle on the GPX-313 with a diameter of $0.15m$. This explained the increased performance parameters that have been measured in the experimental test compared to the earlier simplified CFD calculations. The larger $0.3m$ diameter GPX-313 has not been simulated, but could be easily included in this computational domain for further studies if necessary.

Compensation for interference during testing has been used including Glauerts wind tunnel interference for airscrew compensation, pressure difference of the propeller hub and motor cooling introduced torque. These compensations have led to an improved correlation with CFD data.

The larger $0.3m$ diameter GPX-313 was tested with the same tip Mach number and advance ratio as a the smaller polished $0.15m$ diameter GPX-313. The trends from the two propellers were very similar when the compensations mentioned above were applied. The larger propeller had a reduced C_T over the whole testing range.

Finite element methods was used to estimate the stresses and deformations of different propellers. One of these geometries has been exported to CFD to study its aerodynamic performance. The deformed geometry was simulated using the existing computational domains, using a rotational speed of $13000rpm$ and a wind speed of $25m/s$ for direct comparison with the wind tunnel tests. Reasons for an increase in performance parameters may be the increased diameter or the pitch angles. Another effect is the increased cone angle as a consequence of the rotational load. Also, it is assumed that the change of the angle of the leading edge has an effect, which causes the blade to twist slightly. In order to understand this effect, a sectionwise analysis of the blade or additional simulations which isolate the aforementioned effects would be necessary, but could not be realised during this thesis work.

In general, it can be concluded that 3D printed box propellers can be used to validate CFD results but should not be used under high mechanical load due to high deformation and creep in the material.

Overall, we were able to perform experiments of different propellers in the wind tunnel, and obtain accurate CFD calculations of the propeller performance. Due to close results from experiments and calculations, the difference on performance parameters is almost down to measurement errors for the GPX313 and effects that can affect the performance have been identified.

6.1 Future work

To capture the deformation under load properly, and to get an improved shape due to deformations, it might be worth considering using fluid solid interaction (FSI) simulations in the near future.

The blade design can still be improved, *e.g.* with a change in airfoil profile, number

of blades, blade and cone angle, and so on.

To reduce the manufacturing cost in the long run, and to be able to adjust the blade angle, a new hub with modular blades could be designed. As such a hub would most likely increase the total weight of the propeller, either the load cell or the motor will need to be changed since the present rig can not handle an increased weight. The demands on the rig have been reduced in terms of rotational speed, and motors manufactured for lower rpm can be considered.

To reduce uncertainties caused by upstream obstacles of the propeller a single propeller experiment could be designed where the propeller is mounted in a pull configuration. This would require a redesign of the current design or hub but would probably reduce the complexity in CFD simulations.

Counter rotating set-up should be developed and can be tested in the current rig with propellers of $0.15m$ diameter.

As the small propellers still carry some uncertainties, such as surface roughness and deformation due to material and size, it would be advisable to either use propellers with a larger diameter or change the material from plastic to metal. This would involve some further adjustment of the test rig.

Equipment to measure deformation optically by trace points on a blade during load exist at Chalmers wind tunnel lab and can be used to validate deformation of a blade.

Bibliography

[1] S. Adriansson, Design and testing of a box-bladed propeller, Master's thesis, Chalmers University of Technology, Gothenburg, Sweden (2013).

[2] V. Olofsson, J. Pettersson, Experimental investigation of an innovative high speed propeller, Master's thesis, Chalmers University of Technology, Gothenburg, Sweden (2013).

[3] F. Carlsvärd, Experimental test rig design and testing of a box-bladed propeller, Master's thesis, Luleå University of Technology, Luleå, Sweden (2013).

[4] A. Lind, Aerodynamic simulations of an innovative high speed propeller, Master's thesis, Chalmers University of Technology, Gothenburg, Sweden (2013).

[5] P. Marzocca, The naca airfoil series.
URL `http://people.clarkson.edu/~pmarzocc/AE429/The%20NACA%20airfoil%20series.pdf`

[6] E. Torenbeek, H. Wittenberg, Flight Physics: Essentials of Aeronautical Disciplines and Technology, with Historical Notes, Springer, 2009.

[7] I. Kroo, Nonplanar wing concepts for increased aircraft efficiency, in: VKI lecture series on Innovative Configurations and Advanced Concepts for Future Civil Aircraft, 2005.

[8] H. Versteeg, W. Malalasekera, An Introduction to Computational Fluid Dynamics: The Finite Volume Method, Pearson Education Limited, 2007.

[9] J. Anderson, Fundamentals of Aerodynamics, Anderson series, McGraw-Hill Education, 2010.

[10] J. Anderson, Modern Compressible Flow: With Historical Perspective, McGraw-Hill series in aeronautical and aerospace engineering, McGraw-Hill, 2004.

[11] H. Schlichting, K. Gersten, Boundary Layer Theory, 8th Edition, Springer, Berlin, 2000.

[12] ANSYS, Inc., ANSYS CFX-Solver Theory Guide, ANSYS, Inc., Canonsburg, Pennsylvania, 14th Edition (11 2011).

[13] J. Kim, P. Moin, R. Moser, Turbulence statistics in fully developed channel flow at low reynolds number, J. Fluid Mech.

[14] T. Adams, C. Grant, A simple algorithm to relate measured surface roughness to equivalent sand-grain roughness, International Journal of Mechanical Engineering and Mechatronics.

[15] K. Flack, M. Schultz, Review of hydraulic roughness scales in the fully rough regime, Journal of Fluids Engineerig.

[16] J. B. Barlow, A. Pope, W. H. Rae, Low-speed wind tunnel testing, Wiley, New York, 1999.

[17] C. A. Negulescu, Airbus ai-px7 cror design features and aerodynamics, 2013.

[18] J. LEPICOVSKY, Laser velocimeter measurements in a model propeller flowfield, JOURNAL OF FLUIDS ENGINEERING-TRANSACTIONS OF THE ASME 110 (4) (1988) 350–354.

[19] H. Glauert, Wind tunnel interference on wings, bodies and airscrews, [Great Britain] Aeronautical Research Committee. Reports and memoranda no. 1566, H.M. Stationery Office, 1933.

[20] Futek.inc, Futek Glossary of Terms.
URL `https://www.futek.com/files/PDf/Manuals_and_Technical_Documents/FUTEK%20Glossary%20of%20Terms.pdf`

[21] IRD balancing. 2009, he Practical Application of ISO 1940/1.
URL `http://www.irdbalancing.com/downloads/techpaper1balqualityreqmts.pdf`

[22] H. V. Borst, Associates, Summary of propeller design procedures and data volume 1, aerodynamic design and installation, Tech. rep., National Techical Information Serivce (1973).

[23] K.-H. Grote, J. Feldhusen (Eds.), DUBBEL – Taschenbuch für den Maschinenbau, 22nd Edition, Springer, Berlin, 2007.

[24] M. Elmstrom, Numerical Prediction of the Impact of Non-Uniform Leading Edge Coatings on the Aerodynamic Performance of Compressor Airfoils, Storming Media, 2004.

[25] J. Stack, W. F. Lindsey, Test of n-85 n-86 and n-87 airfoil section in the 11-inch high-speed wind tunnel, Tech. Rep. MSU-CSE-00-2, National Advisory Committee For Aeronatics (1938).

[26] J. C. Heitmeyer, Effect of nose shape and trailing-edge bluntness on the aerodynamic characteristics of an unswept wing of aspect ratio 3.1, taper ratio 0.4, and 3-percent thickness, Tech. rep. (1954).

[27] Stratasys - Polyjet, Polyjet Material Data Sheet (5 2014).

[28] Futek, Inc., Futek Model MBA500 Torque and Trhurst Bi-Axial Sensor, Futek, Inc., 10 Thomas, Irvine, CA 92618 USA, 1st Edition (5 2015).

[29] National Instruments Inc., OPERATING INSTRUCTIONS AND SPECIFICATIONS NI 9237, National Intruments, Inc., Austin, TX, USA, 1st Edition (2 2015).

[30] Futek, Inc., Model MBA500 Series - Extraneous Load Factors, Futek, Inc., 10 Thomas, Irvine, CA 92618 USA, 1st Edition (5 2015).

[31] J. Marklund, Under-body and Diffuser Flows of Passenger Vehicles, Doktorsavhandlingar vid Chalmers tekniska högskola, Chalmers tekniska högskola and Chalmers tekniska högskola. Institutionen för tillämpad mekanik, 2013.

A

Chalmers L2 Wind Tunnel

Turbulent Intensity

The turbulent intensity at the test section by Chalmers Applied Mechanical internal resources before this thesis test sessions. The measurement was take by moving a probe through the central part of the cross-section from test section inlet to close to the outlet. The measurements are shown in figure A.1

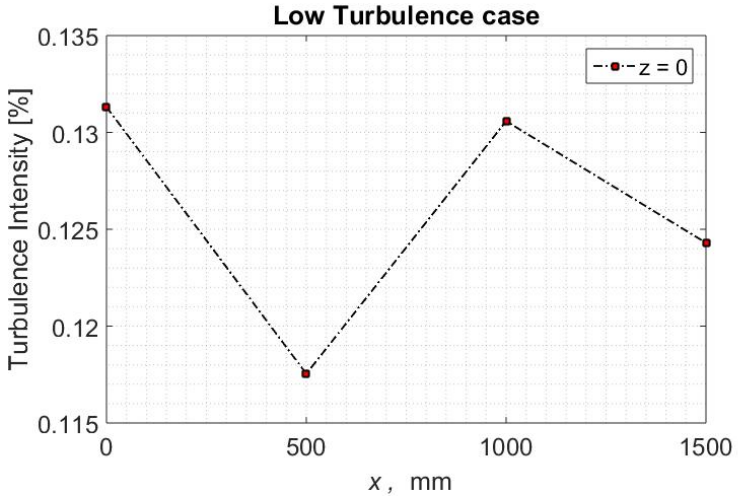

Figure A.1: Measurements by Hot wire in Chalmers L2 Wind tunnel

B

External Measurements

Geometry Measurements

Figure B.1 shows the manufacturing defects using CatiaV5-62013s Deviation tool measuring the height of the surface with an average distance between measured points of every 0.2 mm and point cloud data provided from Digital Mechanics.

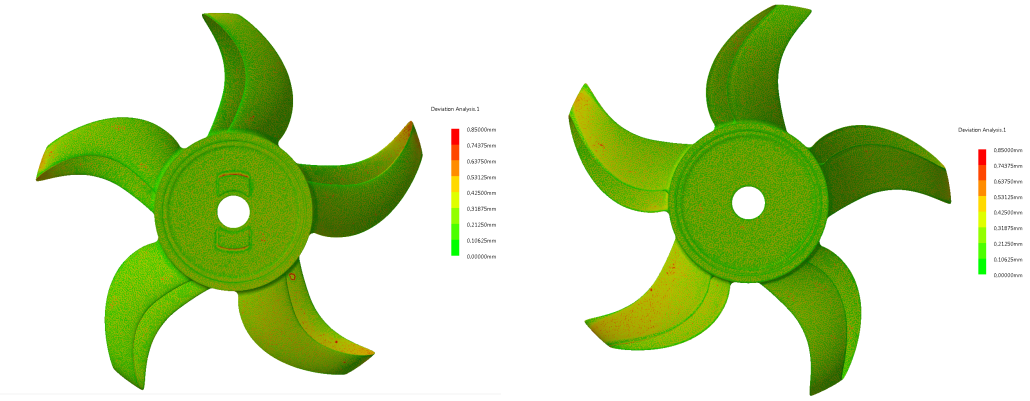

(a) Deviation Analysis Front

(b) Deviation Analysis Rear

Figure B.1: Deviation Analysis

The point cloud had locally very limited number of points and high angle between the scanner and the normal of the surface. A high angle reduces the accuracy of the measurement since the points gets elongated, the best tip scan data are shown in figure B.2b and worst in B.2a. The blade with the highest point quality is the the one pointing upwards in figure B.1.

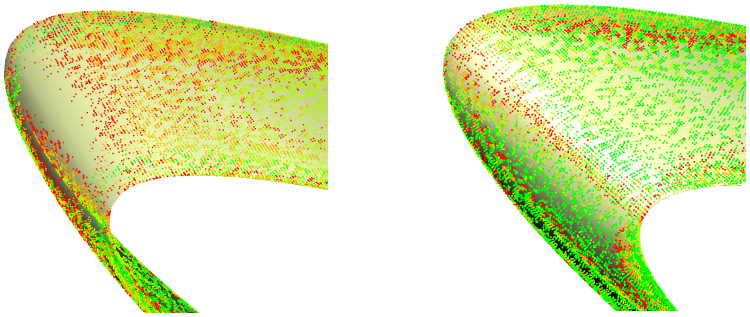

(a) Worst Tip Scan resolution

(b) Best Tip Scan resolution

Figure B.2: Point Cloud Analysis

Surface Roughness

Surface Roughness was done by Toponova AB where measurements are shown in table B.1 and the raw data in figure B.3 and B.4. The measurements was taken a a radius of around 67mm from TE to LE where the outer most edges are not included since the measurement apparatus need a flat surface to start at. The measurements have an uncertainty of ±5% *Ra*.

Table B.1: Surface roughness Measured by Toponova

	Pa	Wa	Ra
LB Pressure Side	7.16	3.76	4.97
LB Suction Side	11.30	6.88	8.20
TB Pressure Side	5.79	3.5	4.3
TB Suction Side	13.60	10.7	6.56

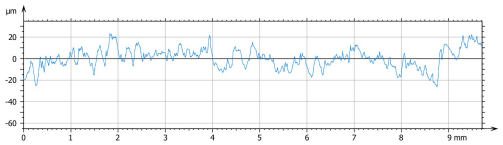

(a) Pa at LB Pressure Side

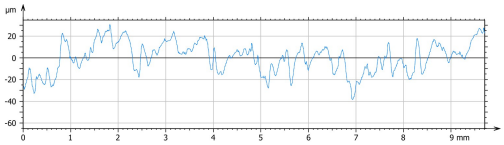

(b) Pa at LB Suction side

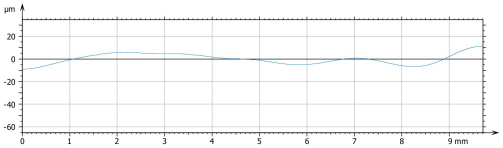

(c) Wa at LB Pressure Side

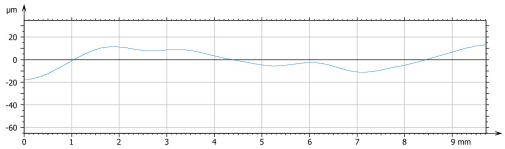

(d) Wa at LB Suction Side

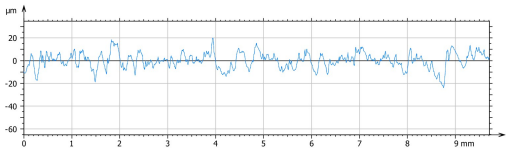

(e) Ra at LB Pressure Side

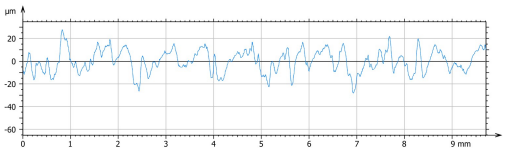

(f) Ra at LB Suction Side

Figure B.3: Leading Blade Surface

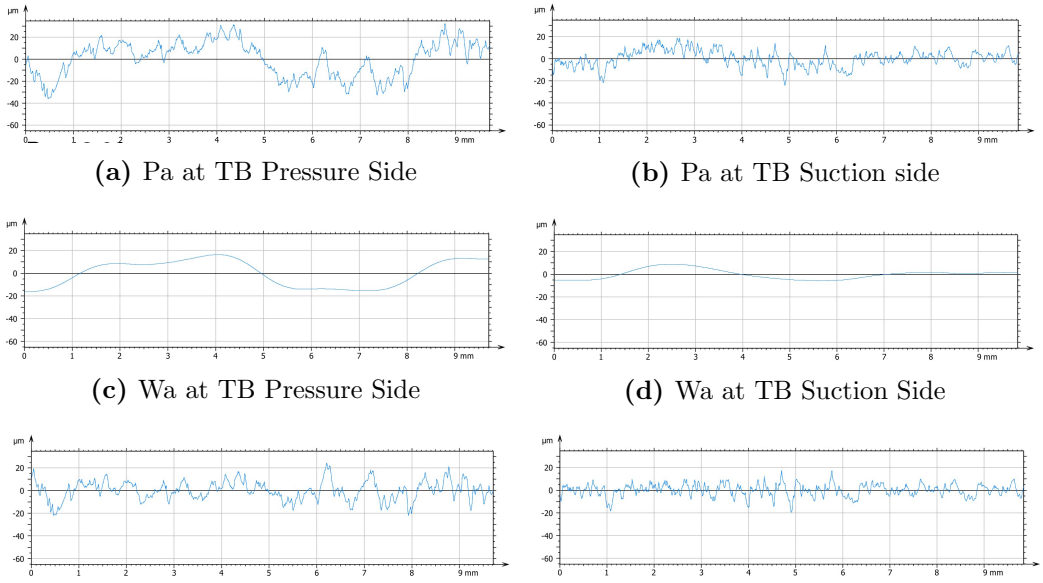

(a) Pa at TB Pressure Side

(b) Pa at TB Suction side

(c) Wa at TB Pressure Side

(d) Wa at TB Suction Side

(e) Ra at TB Pressure Side

(f) Ra at TB Suction Side

Figure B.4: Trailing Blade Surface

Planar Section Deformation

Table B.2 shows the planar angle of change in the blade section for each section. The normal of the of the first plane of measurement is directed from the hub at the root of the leading blade following a spline along the blade profile to the trailing blade. The angle is measured a the trailing edge and is relative to the original blade angle.

Table B.2: Angle change between the deformed and non deformed blade

P.Nr	Angle
1	0
2	0.1
3	-0.5
4	-0.95
5	-1.1
6	1.1
7	1
8	-0.6
9	-0.7
10	0.14
11	0.89
12	1.25
13	-1.39
14	-1.2
15	-0.7
16	0.1
17	0.3
18	0.6
19	0.5
20	0.3
21	0.1
22	0
23	0

C

Rig Equipment Evaluation

Load Cell Precision

MBA500 load cell nr 2 was tested with 49.5-50.5g weight loaded vertically on the load cell. The test was repeated 10 times and results can be seen in figure below.

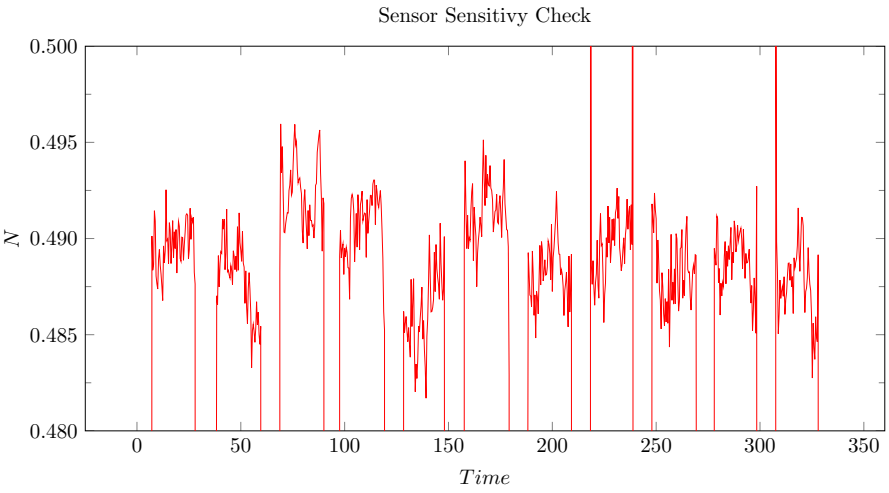

Vibrations

Figure C.1 show vibration measured during testing of old mountings and material. There is a failure marked in the plots which is high speed propeller failure. There is a test mark as new which is vibration measured after redesign hub mount.

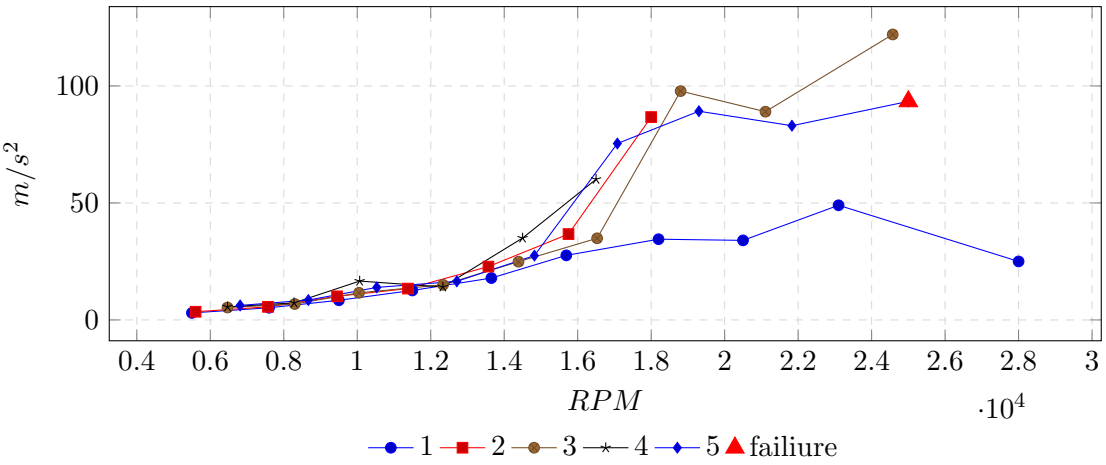

Figure C.1: Vibration from old hub

Motor Introduce Torque

To see the influence swirl from motor cooling the torque was measured without any propeller mounted on the motor.

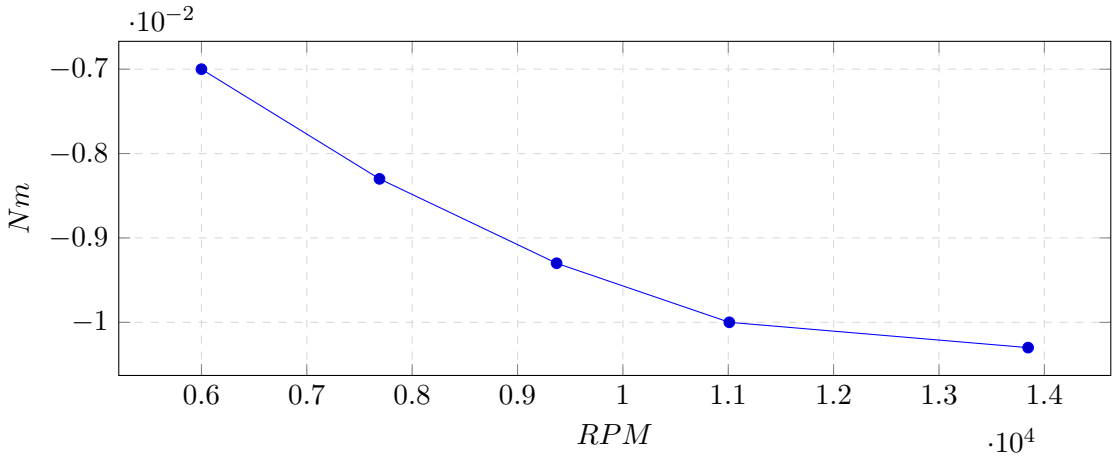

Figure C.2: Motor nr 4 Model-3080/8 Torque without propeller

Hub Pressure interference

The pressure difference between the front and backside of the hub was measured with a FCO510 Micromanometer with two pressure probes. The pressure is shown in figure C.3. The propeller used during the test was the B6 polished GPX-313 0.15m with a rear nacelle gap of 1.5-2mm.

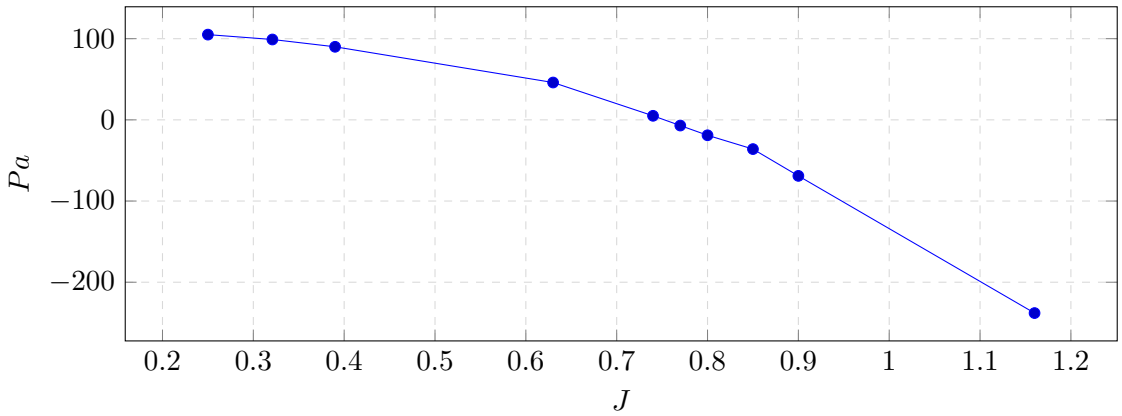

Figure C.3: Pressure difference for GPX-313 hub

D

PIV Results

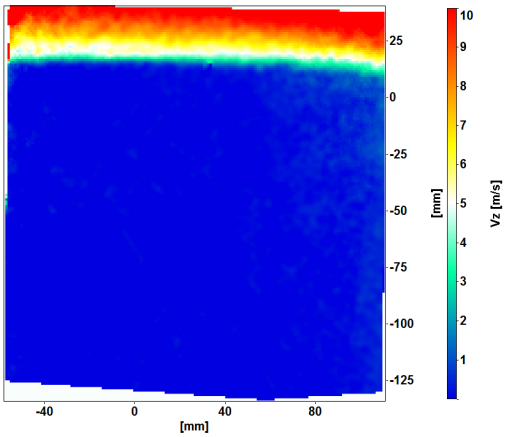

(a) V_y averaged with 100 Samples

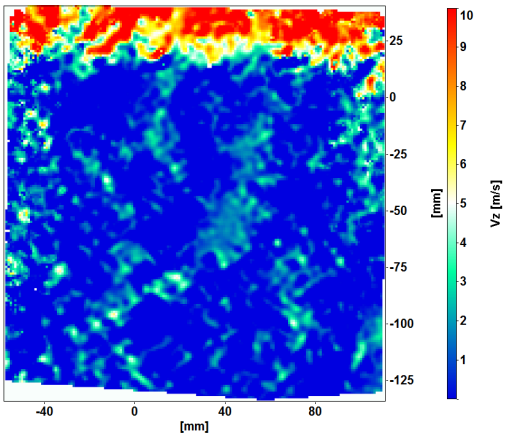

(b) V_y one of Instantaneous Sample

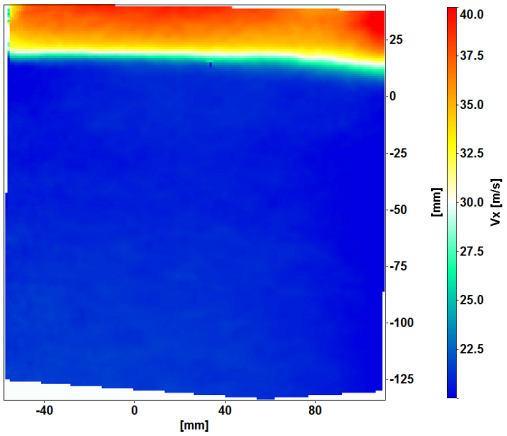

(c) V_x averaged with 100 Samples

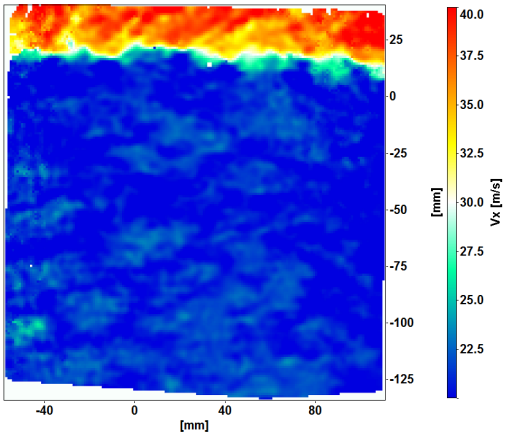

(d) V_x one of Instantaneous Sample

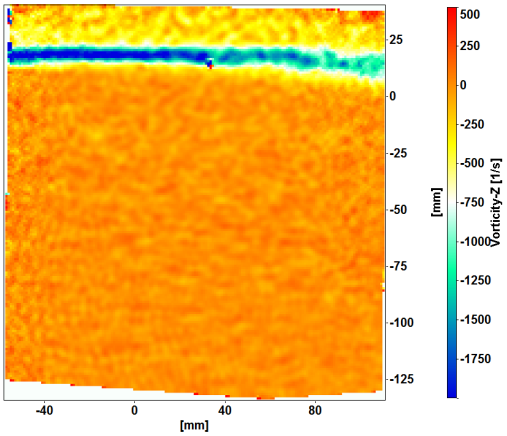

(e) ω_y averaged with 100 Samples

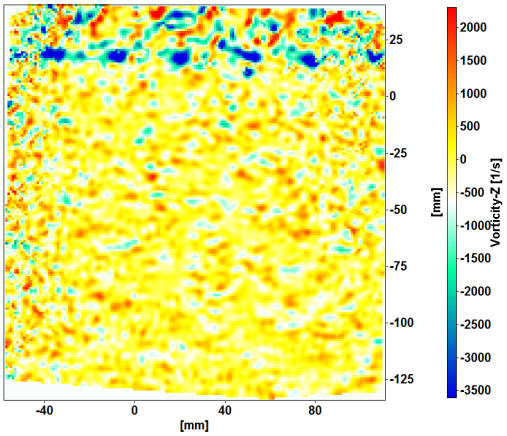

(f) ω_y one of Instantaneous Sample

Figure D.1: GPX-313 at 13106 RPM and 24.5m/s

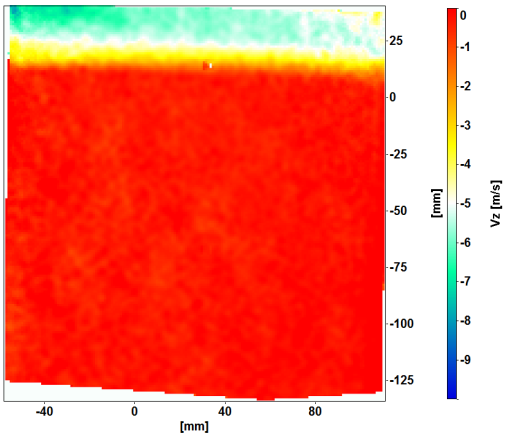

(a) V_y averaged with 100 Samples

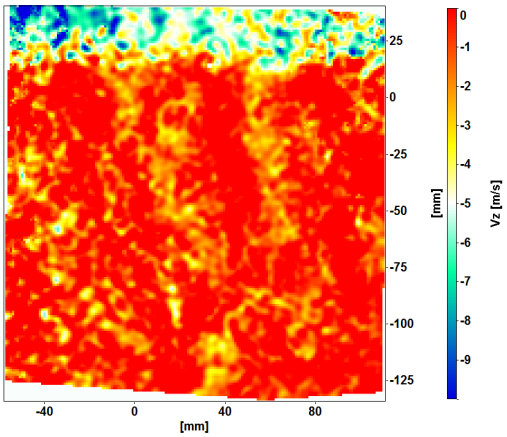

(b) V_y one of Instantaneous Sample

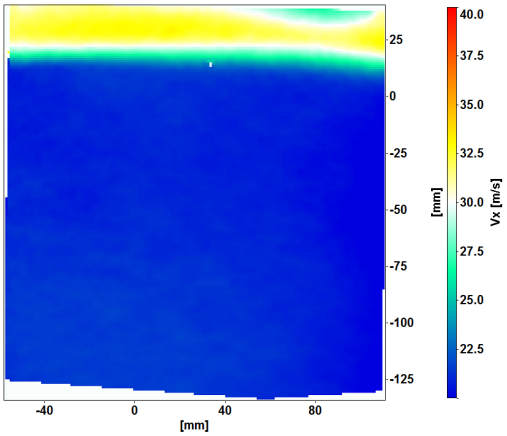

(c) V_x averaged with 100 Samples

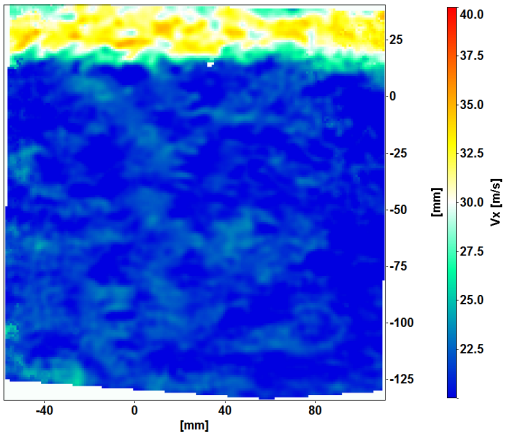

(d) V_x one of Instantaneous Sample

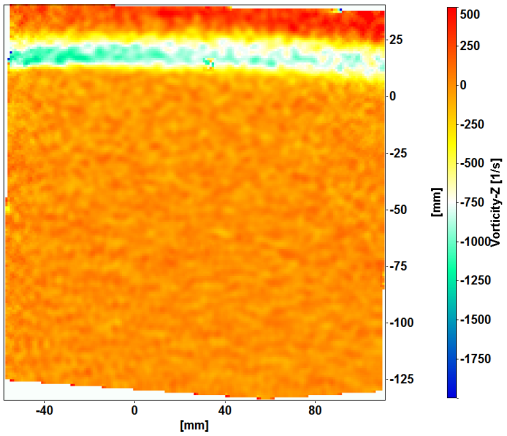

(e) ω_z averaged with 100 Samples

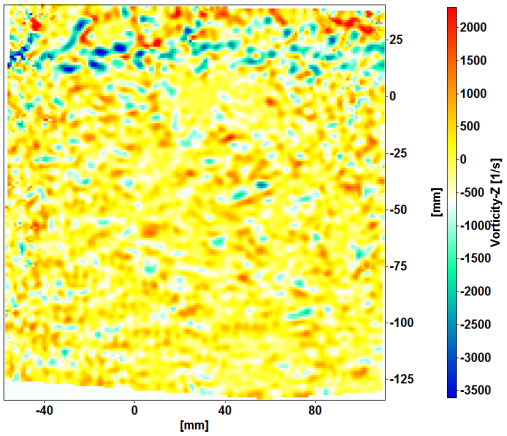

(f) ω_z one of Instantaneous Sample

Figure D.2: GPS-101 at 13109 RPM and 24.7m/s

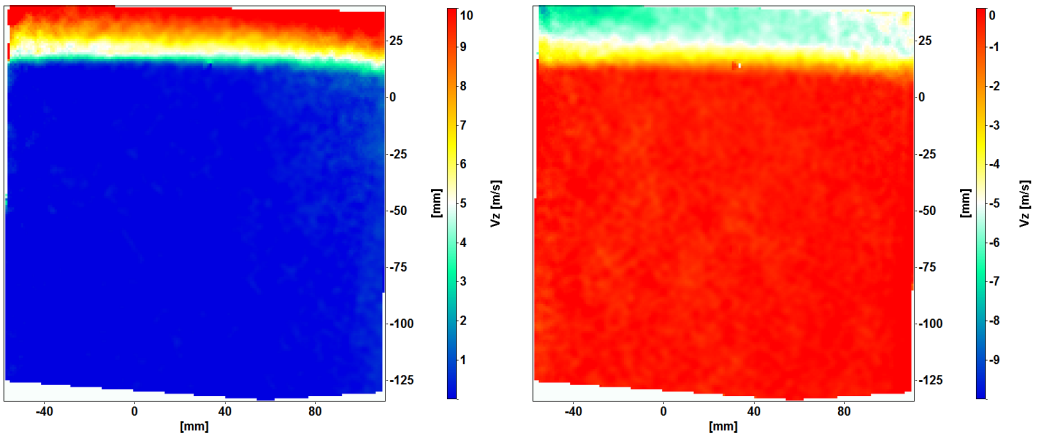

(a) V_z GPX-313 **(b)** V_z GPS-101

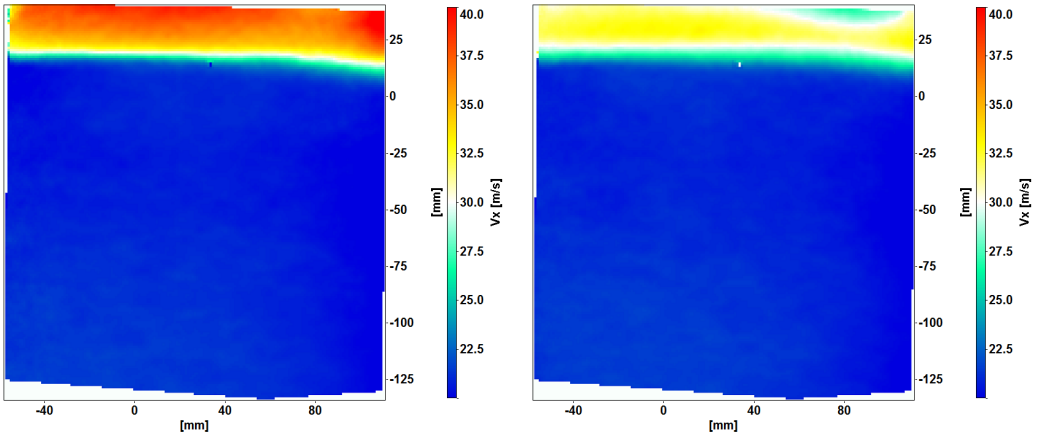

(c) V_x GPX-313 **(d)** V_x GPS-101

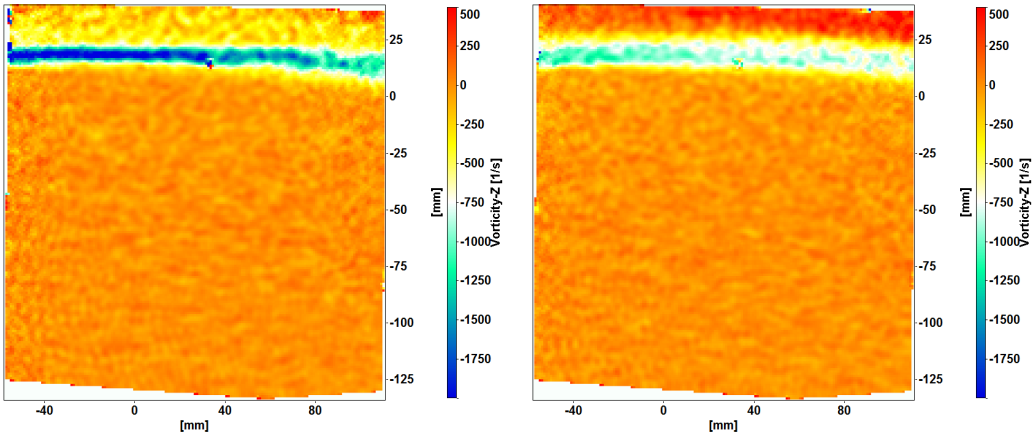

(e) ω_z GPX-313 **(f)** ω_z GPS-101

Figure D.3: Comparision between GPX-313 and GPS-101 Averaged

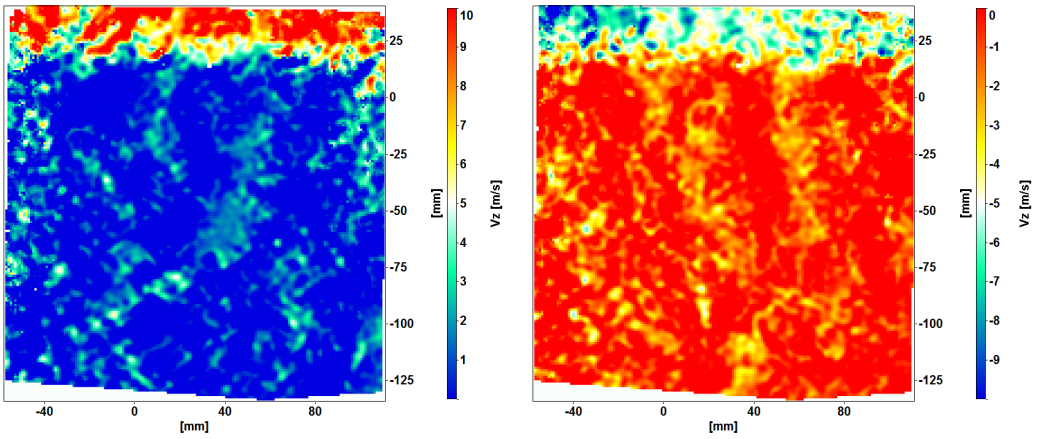

(a) V_z GPX-313 **(b)** V_z GPS-101

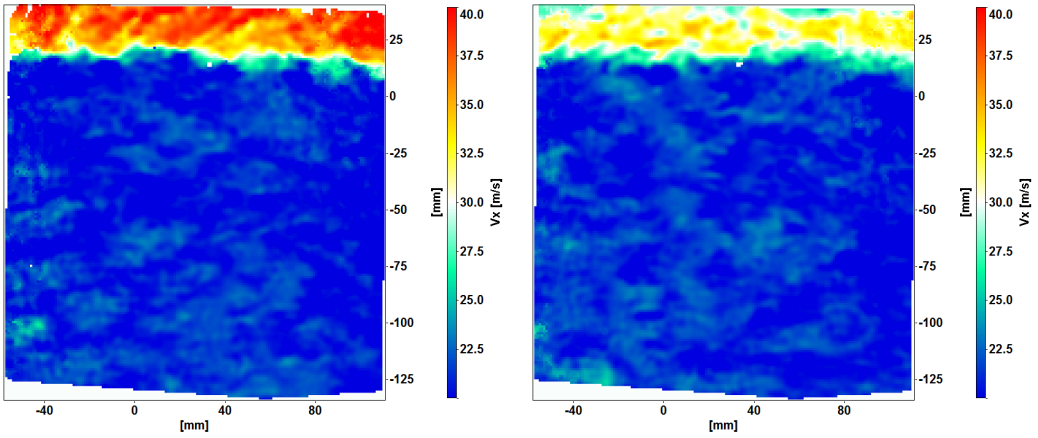

(c) V_x GPX-313 **(d)** V_x GPS-101

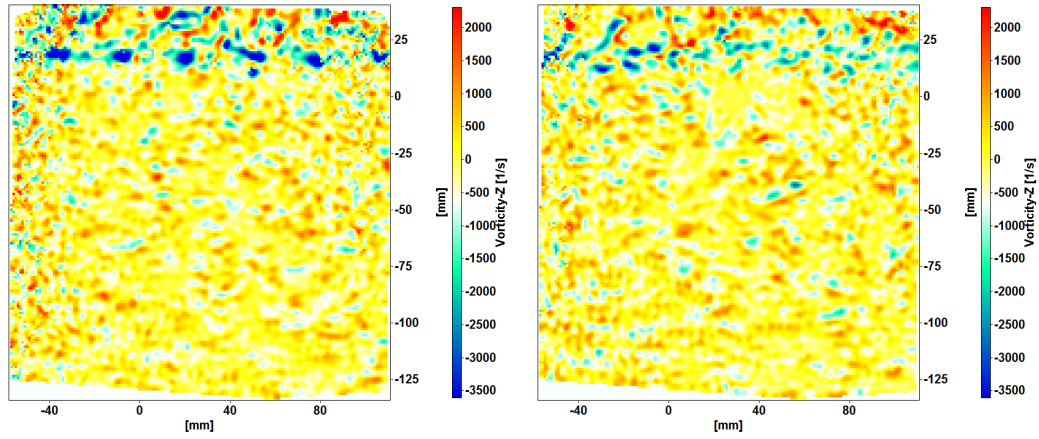

(e) ω_z GPX-313 **(f)** ω_z GPS-101

Figure D.4: Comparision between GPX-313 and GPS-101 Instantaneous

E

Static Testing Results

Static Test Results

Figure E.1 and E.2 show results from the latest performed static test session on the 26th of March 2015.

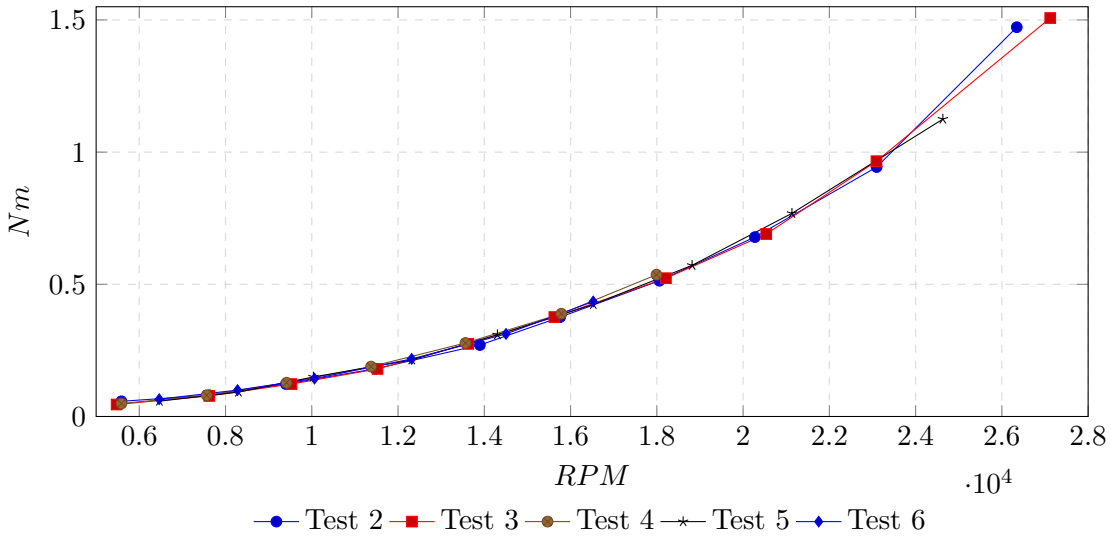

Figure E.1: Static Torque of GPX-313

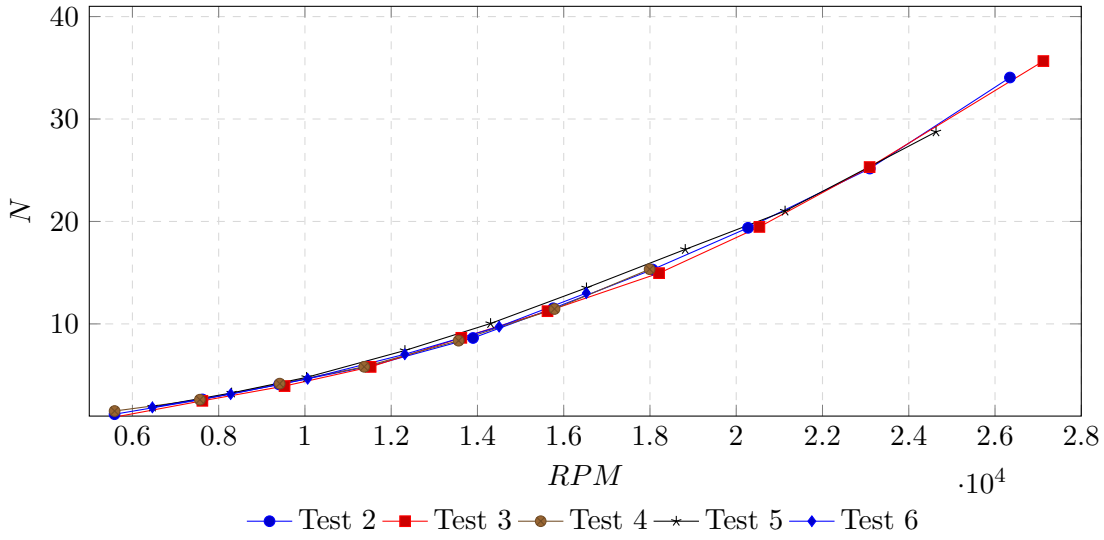

Figure E.2: Static Thrust of GPX-313

Static Force Change

Figure E.3 shows the thrust in a test rig during early testing, there is a high level of noise due to vibration but it illustrates the change in ambient flow field at static testing in terms of reduced thrust. This test is at 18200 RPM with $100m/s^2$ peak vibrations and is a section of the last high speed test was done in the static rig. Longer test was done but no tendency was seen of flow field stabilizing within a reasonable time frame.

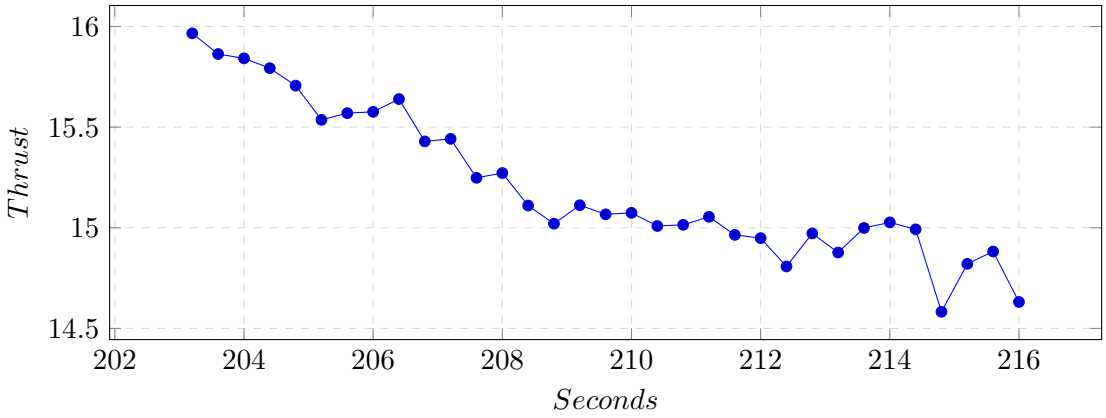

Figure E.3: Input Force during static testing at 18200 RPM during 13.2sec with peak vibrations of $100m/s^2$

Static Test Results Tabular

Tables E.1 to E.5 show results from the latest performed static test session on the 26th of March 2015.

Table E.1: Test 2 - Tabular Data

RPM	Nm	N
5,586	$5.75 \cdot 10^{-2}$	1.18
7,623	$8.03 \cdot 10^{-2}$	2.63
9,401	0.12	4.09
11,478	0.18	5.84
13,898	0.27	8.62
15,757	0.38	11.53
18,059	0.51	15.3
20,274	0.68	19.38
23,096	0.94	25.16
26,346	1.47	34.05

Table E.2: Test 3 - Tabular Data

RPM	Nm	N
5,476	$4.53 \cdot 10^{-2}$	0.81
7,622	$7.78 \cdot 10^{-2}$	2.49
9,527	0.12	3.93
11,524	0.18	5.8
13,626	0.27	8.64
15,624	0.38	11.24
18,211	0.52	14.95
20,537	0.69	19.47
23,092	0.97	25.31
27,121	1.51	35.66

Table E.3: Test 4 - Tabular Data

RPM	Nm	N
5,587	$4.92 \cdot 10^{-2}$	1.5
7,564	$8.03 \cdot 10^{-2}$	2.6
9,415	0.13	4.17
11,374	0.19	5.81
13,563	0.28	8.36
15,787	0.39	11.45
17,992	0.54	15.34

Table E.4: Test 5 - Tabular Data

RPM	Nm	N
6,467	$5.79 \cdot 10^{-2}$	1.89
8,300	$9.22 \cdot 10^{-2}$	3.26
10,038	0.15	4.78
12,318	0.21	7.4
14,304	0.31	10.04
16,528	0.42	13.52
18,818	0.57	17.27
21,133	0.77	21.02
24,632	1.12	28.75

Table E.5: Test 6 - Tabular Data

RPM	Nm	N
6,463	$6.55 \cdot 10^{-2}$	1.85
8,278	$9.99 \cdot 10^{-2}$	3.15
10,063	0.14	4.64
12,316	0.22	7.04
14,503	0.31	9.73
16,524	0.44	13.01